RESEARCH

UDOT Keeping Utah Moving

Utah Department of Transportation - Research Division
4501 South 2700 West - P.O. Box 148410 - SLC,UT 84114-8410

Report No. UT-25.23

DEVELOPING AND CHARACTERIZING SELF-HEALING CONCRETE FOR BRIDGE DECKS

Prepared For:

Utah Department of Transportation
Research & Innovation Division

Final Report
June 2025

DISCLAIMER

The authors alone are responsible for the preparation and accuracy of the information, data, analysis, discussions, recommendations, and conclusions presented herein. The contents do not necessarily reflect the views, opinions, endorsements, or policies of the Utah Department of Transportation or the U.S. Department of Transportation. The Utah Department of Transportation makes no representation or warranty of any kind, and assumes no liability therefore.

ACKNOWLEDGMENTS

The authors would like to thank the Utah Department of Transportation (UDOT) for funding this research. We also extend our gratitude to Graymont for supplying the quicklime aggregates and Sika for providing the ViscoCrete-2110-based super-plasticizer used in this study. Additionally, we express our thanks to the UDOT research project Technical Advisory Committee (TAC) members, including Jason Richins, Scott Strader, Jared Dastrup, Radhakrishnan Ukkiramapandian, James Corney, Thad Pinkerton, Brad Loveless, and David Stevens. We would also like to thank USU graduate student, Abdullah Al Sarfin, for his help with formatting the final report.

TECHNICAL REPORT ABSTRACT

1. Report No.	2. Government Accession No.	3. Recipient's Catalog No.
UT-25.23	N/A	N/A

4. Title and Subtitle	5. Report Date
Developing and Characterizing Self-Healing Concrete for Bridge Decks	June 2025
	6. Performing Organization Code: N/A
7. Author(s): Srishti Banerji, Mehrnoosh Nazari	8. Performing Organization Report No.: N/A
9. Performing Organization Name and Address: Utah State University, Department of Civil and Environmental Engineering, 4110 Old Main Hill, Logan, UT 84322-4110	10. Work Unit No.: 5H092 20H
	11. Contract or Grant No.: 24-8230
12. Sponsoring Agency Name and Address: Utah Department of Transportation, 4501 South 2700 West, P.O. Box 148410, Salt Lake City, UT 84114-8410	13. Type of Report & Period Covered: Final Report, August 2023 to June 2025
	14. Sponsoring Agency Code: PIC No. UT23.108

15. Supplementary Notes

Prepared in cooperation with the Utah Department of Transportation and the U.S. Department of Transportation, Federal Highway Administration

16. Abstract

This study investigates the self-healing potential of concrete with quicklime (CaO) aggregates, inspired by Roman concrete, to extend the service life of transportation infrastructure. Three concrete mixtures – control (0% quicklime), 2% quicklime (C-Q 2%), and 4% quicklime (C-Q 4%) – were tested for fresh properties, mechanical performance, durability, and crack-healing efficacy under cyclic water/air-drying and deicing salt solution/air-drying conditions. Microcracks with widths from 100 to 200 μm (0.004–0.008 inches) and 200 to 300 μm (0.008–0.012 inches), and macrocracks with widths from 300 to 550 μm (0.012–0.022 inches), were monitored over 180 days using optical microscopy, ultrasonic pulse velocity (UPV), water flow tests, and SEM-EDS. The addition of 4% quicklime reduced workability and setting time but improved compressive and tensile strength by up to 63% and 54%, respectively, due to enhanced C-S-H formation. Durability improvements included reduced chloride permeability, 23% higher electrical resistivity, increased abrasion resistance, and lower freeze-thaw mass loss. Microcracks exhibited more effective healing than macrocracks, with quicklime mixtures outperforming the control mixture, and comparable healing performance observed between the 2% and 4% dosages. Specimens with 4% quicklime achieved 100% surface closure for microcracks and up to 13.8% UPV gain, indicating substantial internal healing. Macrocrack healing ranged from 24% (water) to 69% (deicing salt), though salt exposure often led to superficial NaCl crystallization. Internal healing was more reliable, with water slightly favoring microcracks and deicing salt enhancing macrocrack healing via NaCl-facilitated $CaCO_3$ nucleation. SEM-EDS analysis confirmed a transition from C–S–H as the dominant healing product in control specimens to $CaCO_3$ in quicklime mixtures.

17. Key Words	18. Distribution Statement	23. Registrant's Seal
Quicklime, Calcium carbonate, Cracking, Roman concrete, Self-healing	Not restricted. Available through: UDOT Research & Innovation Div., 4501 South 2700 West, P.O. Box 148410, Salt Lake City, UT 84114-8410, www.udot.utah.gov/go/research	N/A

19. Security Classification (of this report)	20. Security Classification (of this page)	21. No. of Pages	22. Price
Unclassified	Unclassified	101	N/A

TABLE OF CONTENTS

LIST OF FIGURES

LIST OF TABLES

UNIT CONVERSION FACTORS

Units used in this report and not conforming to the UDOT standard unit of measurement (U.S. Customary system) are given below with their U.S. Customary equivalents:

SI* (MODERN METRIC) CONVERSION FACTORS

APPROXIMATE CONVERSIONS TO SI UNITS

Symbol	When You Know	Multiply By	To Find	Symbol
		LENGTH		
in	inches	25.4	millimeters	mm
ft	feet	0.305	meters	m
yd	yards	0.914	meters	m
mi	miles	1.61	kilometers	km
		AREA		
in^2	square inches	645.2	square millimeters	mm^2
ft^2	square feet	0.093	square meters	m^2
yd^2	square yard	0.836	square meters	m^2
ac	acres	0.405	hectares	ha
mi^2	square miles	2.59	square kilometers	km^2
		VOLUME		
fl oz	fluid ounces	29.57	milliliters	mL
gal	gallons	3.785	liters	L
ft^3	cubic feet	0.028	cubic meters	m^3
yd^3	cubic yards	0.765	cubic meters	m^3
	NOTE: volumes greater than 1000 L shall be shown in m^3			
		MASS		
oz	ounces	28.35	grams	g
lb	pounds	0.454	kilograms	kg
T	short tons (2000 lb)	0.907	megagrams (or "metric ton")	Mg (or "t")
		TEMPERATURE (exact degrees)		
°F	Fahrenheit	5 (F-32)/9 or (F-32)/1.8	Celsius	°C
		ILLUMINATION		
fc	foot-candles	10.76	lux	lx
fl	foot-Lamberts	3.426	candela/m^2	cd/m^2
		FORCE and PRESSURE or STRESS		
lbf	poundforce	4.45	newtons	N
lbf/in^2	poundforce per square inch	6.89	kilopascals	kPa

APPROXIMATE CONVERSIONS FROM SI UNITS

Symbol	When You Know	Multiply By	To Find	Symbol
		LENGTH		
mm	millimeters	0.039	inches	in
m	meters	3.28	feet	ft
m	meters	1.09	yards	yd
km	kilometers	0.621	miles	mi
		AREA		
mm^2	square millimeters	0.0016	square inches	in^2
m^2	square meters	10.764	square feet	ft^2
m^2	square meters	1.195	square yards	yd^2
ha	hectares	2.47	acres	ac
km^2	square kilometers	0.386	square miles	mi^2
		VOLUME		
mL	milliliters	0.034	fluid ounces	fl oz
L	liters	0.264	gallons	gal
m^3	cubic meters	35.314	cubic feet	ft^3
m^3	cubic meters	1.307	cubic yards	yd^3
		MASS		
g	grams	0.035	ounces	oz
kg	kilograms	2.202	pounds	lb
Mg (or "t")	megagrams (or "metric ton")	1.103	short tons (2000 lb)	T
		TEMPERATURE (exact degrees)		
°C	Celsius	1.8C+32	Fahrenheit	°F
		ILLUMINATION		
lx	lux	0.0929	foot-candles	fc
cd/m^2	candela/m^2	0.2919	foot-Lamberts	fl
		FORCE and PRESSURE or STRESS		
N	newtons	0.225	poundforce	lbf
kPa	kilopascals	0.145	poundforce per square inch	lbf/in^2

*SI is the symbol for the International System of Units. (Adapted from FHWA report template, Revised March 2003)

LIST OF ACRONYMS

AASHTO	American Association of State Highway and Transportation Officials
ASR	Alkali–Silica Reaction
ASTM	American Society for Testing and Materials
C-Q	Concrete with Quicklime
DOT	Department of Transportation
EDS	Energy-Dispersive X-Ray Spectroscopy
FHWA	Federal Highway Administration
FT	Freeze–Thaw
ITZ	Interfacial Transition Zone
SEM	Scanning Electron Microscopy
SSD	Saturated Surface Dry
TAC	Technical Advisory Committee
UPV	Ultrasonic Pulse Velocity
UDOT	Utah Department of Transportation

EXECUTIVE SUMMARY

This study explores the self-healing capabilities of concrete incorporating quicklime (CaO) aggregates, aiming to improve the durability of concrete bridge decks that are prone to cracking from shrinkage, temperature changes, and traffic-induced stresses. The approach of adding quicklime for self-healing is inspired by the longevity of ancient Roman concrete. In this project, three concrete mixtures with 0%, 2%, and 4% quicklime were evaluated for their fresh properties, mechanical strength, durability, and crack-healing performance.

The test results show the addition of quicklime significantly affected fresh concrete behavior, reducing both workability and setting time due to its high reactivity. While requiring superplasticizers for adjusting the workability, mixtures with quicklime showed elevated internal temperatures and accelerated setting with the 4% quicklime mixture exhibiting a setting time of 21 minutes as compared to 74 minutes for the control mixture. Quicklime incorporation improved compressive and tensile strengths, with the 4% quicklime batch showing up to 63% strength gain at 28 days and a 54.3% increase in splitting tensile strength. Durability improved with quicklime addition, as reflected by a 23% increase in electrical resistivity at 90 days (2% quicklime), lower abrasion-induced mass loss, and enhanced freeze–thaw resistance, with mass loss reduced from 8.8% in the control to 4% at 4% quicklime.

Crack-healing in the three mixtures was monitored under two environmental conditions representative of bridge deck exposure: cyclic water/air-drying and deicing salt solution (20% NaCl)/air-drying. For both the exposure conditions, all the specimens were induced with controlled microcracks (100–200 μm (0.004–0.008 inches) and 200–300 μm (0.008–0.012 inches)) and macrocracks (300–550 μm (0.012–0.022 inches)). Healing was assessed over a period of 180 days using optical microscopy images, ultrasonic pulse velocity (UPV), water flow reduction, and Scanning Electron Microscopy coupled with Energy-Dispersive X-Ray Spectroscopy (SEM-EDS). Under identical exposure conditions and quicklime content, microcracks consistently exhibited greater healing than macrocracks, with healing performance decreasing as crack width increased. At a given crack width and exposure condition, quicklime mixtures outperformed control mixtures, with comparable healing observed between 2% and 4% quicklime content. Across all

mixtures, better surface healing was observed with deicing salts than water, particularly in microcracks due to NaCl crystallization filling the crack mouth. However, for true internal healing measured by UPV, water/air-dry cycles slightly favored microcrack healing (13.8% vs. 12% UPV increase in 4% quicklime), while deicing salt provided slightly better depth-wise healing for macrocracks, likely due to the role of NaCl as a nucleation catalyst for $CaCO_3$ formation.

CHAPTER 1 - INTRODUCTION

This chapter outlines the durability issues in bridge deck structures and presents self-healing concrete as a potential solution, along with the problem statement, research objectives, and an overview of the scope, limitations, and methodology of this study.

1.1. Background

Bridge decks are critical components of transportation infrastructure that are directly exposed to environmental elements such as weather, temperature changes, and deicing chemicals, while also bearing heavy traffic loads. This combination makes them particularly vulnerable to deterioration mechanisms, including temperature fluctuations, chloride and sulfate attack, mechanical wear, alkali–silica reaction (ASR), and various forms of shrinkage as discussed herein [1, 2].

- Temperature fluctuations, particularly freeze–thaw cycles, are a major contributor to deterioration of bridge decks in cold regions. When water infiltrates concrete pores and freezes, it expands by approximately 9% in volume. This expansion generates internal stresses that can cause microcracking, surface scaling, or spalling over time. In these regions, where deicing salts are commonly applied, chloride ingress further exacerbates deterioration by initiating corrosion of steel reinforcement. Additionally, exposure to sulfate-rich environments introduces chemical degradation in concrete, as sulfate ions react with cement hydration products, causing expansive cracking and progressive strength loss.
- Mechanical wear due to heavy and repetitive traffic loading results in surface abrasion of bridge decks, gradually reducing concrete cover and exposing underlying layers to environmental attack. Additionally, abrasion can initiate microcracks, that accelerate the ingress of moisture and aggressive agents, thereby intensifying long-term deterioration.
- Alkali–silica reaction (ASR) is another chemical degradation mechanism that occurs when reactive silica in aggregates reacts with alkalis in the cement paste. This reaction forms an expansive gel that absorbs water and swells, producing internal stresses that lead to map-pattern cracking. ASR-related cracking

weakens the concrete matrix and can significantly reduce durability in moist environments.

- Shrinkage-related cracking is also a major issue in concrete bridge decks. The most significant forms include plastic, autogenous, thermal, and drying shrinkage [2, 3]. Plastic shrinkage occurs while the concrete is still fresh and is often driven by rapid moisture loss from the surface. Autogenous shrinkage results from internal volume changes during hydration, even without moisture loss. Thermal shrinkage occurs during cooling after the exothermic reaction of hydration, and drying shrinkage develops as hardened concrete loses internal moisture over time.

Ultimately, all these deterioration mechanisms lead to cracking and compromising the durability and structural reliability of bridge decks, underscoring the urgent need for advanced materials and strategies to mitigate damage and extend service life. In response, researchers have identified several strategies to mitigate cracking in concrete bridge decks, some of which are mentioned here. For instance, Krauss et al. [4] attributed cracking to thermal loading, concrete shrinkage, and structural restraint from supporting girders, suggesting that using concrete with a lower modulus of elasticity, enhanced creep, and reduced shrinkage can help. Additionally, modifying construction techniques to manage thermal strains and optimizing reinforcement placement can reduce cracking. Saadeghvaziri et al. [5] emphasized boundary restraints as the most critical factor, as they elevate tensile stresses in the deck. Reducing these restraints, such as by using roller-supported girders instead of fully fixed or pinned supports, can effectively minimize cracking. While these methods can reduce the number and size of cracks, they cannot eliminate cracking. As a result, post-cracking solutions, such as the use of crack sealants [6, 7] and structural overlays [8, 9] have also gained attention. However, most of these approaches to address cracking problems depend on external repairs and maintenance interventions, which are costly, disruptive, and provide only temporary solutions.

Determining the primary causes of cracking in bridge decks is inherently complex due to the multifaceted interactions among material properties, environmental conditions, construction practices, and service loads. Conventional maintenance approaches based on

crack detection and repair are reactive and often insufficient. These limitations have driven researchers to explore innovative strategies that allow concrete structures to repair themselves. In this context, self-healing concrete offers a proactive solution by enabling autonomous crack closure and helping restore deterioration without the need for external intervention. Self-healing concrete can help mitigate the impact of cracks, thereby extending the service life of bridge decks and reducing long-term maintenance costs.

Self-healing concrete refers to a class of cementitious materials capable of repairing cracks that form during service, thereby enhancing durability and extending service life without the need for external intervention. The concept is inspired by biological systems that can heal damage over time, and it aims to address the limitations of conventional repair techniques in maintaining long-term structural integrity. Self-healing mechanisms in concrete generally fall into two categories:

- Autogenous healing, which relies on the continued hydration of unreacted cement particles and precipitation of calcium carbonate.
- Autonomic healing, which involves the incorporation of healing agents such as encapsulated polymers, crystalline admixtures, quicklime aggregates, or bacteria. These agents are activated by the ingress of water or changes in environmental conditions.

These healing mechanisms seal cracks, limit permeability, and delay corrosion, reducing the maintenance and enhancing long-term performance. This makes it particularly attractive for critical infrastructure components such as bridge decks, which are exposed to aggressive environments and difficult to access for frequent repairs.

1.2. Problem Statement

Bridge decks recently constructed in Utah have exhibited early-age cracking, which poses significant long-term durability concerns. These cracks can accelerate the ingress of moisture, chlorides from deicing agents, and other aggressive substances, ultimately leading to the corrosion of embedded reinforcement. In addition to reinforcement corrosion, cracking can weaken the concrete matrix, exacerbate freeze–thaw damage, and compromise the overall structural integrity and serviceability of the deck. Aesthetically, such cracking is undesirable and often necessitates costly maintenance interventions, reducing the lifecycle performance of the structure. While ongoing investigations by the

Utah Department of Transportation (UDOT) seek to identify the root causes of premature deck cracking, the implementation of concrete capable of autonomously healing its cracks offers a complementary and proactive mitigation strategy.

The concept of self-healing concrete dates back to Roman times, where ancient structures have demonstrated remarkable longevity under aggressive environmental conditions. Recent studies suggest that the durability of Roman concrete is attributed in part to the inclusion of coarse quicklime (CaO) fragments in the mixture [10]. These lime inclusions serve as localized calcium reservoirs that, upon exposure to water through cracks, react to form calcium carbonate ($CaCO_3$), effectively filling and sealing the cracks. Adopting this approach for modern infrastructure could significantly enhance the durability of bridge decks, thereby extending service life and reducing maintenance costs.

To employ quicklime-based self-healing concrete in Utah bridge construction, a critical first step is the formulation of a viable mixture using regionally available materials. Beyond mixture design, it is essential to evaluate the crack-healing performance of the material under realistic service conditions. In Utah, bridge decks are regularly exposed to brine solutions (combinations of water and deicing salts) for snow and ice removal during winter months. These salt-laden materials are chemically aggressive and may impede or alter the healing processes within concrete. As such, the effects of deicing salt exposure on self-healing performance warrant thorough investigation. To address the aforementioned knowledge gaps, this proposed research will formulate a self-healing concrete mix using regional materials and investigate the effectiveness of the quicklime-based crack healing process under typical service conditions as well as corrosive conditions resulting from deicing salt-based solutions.

1.3. Research Objectives

The primary goal of this research is to develop a quicklime-based self-healing concrete mixture tailored to locally sourced materials and evaluating its crack-healing efficacy under conditions representative of Utah bridge decks. The specific objectives are:

- To develop cementitious mixture containing quicklime aggregates and evaluate its ability to autonomously heal cracks under realistic service conditions.

- To investigate the effects of varying quicklime aggregate dosages on the fresh and mechanical properties, durability, and self-healing performance of concrete.
- To evaluate crack-healing efficacy of quicklime concrete under both standard environmental exposure and deicing salt solution conditions by simulating healing conditions relevant to Utah bridge deck conditions.
- To assess the healing effectiveness across varying crack widths and identify thresholds beyond which healing becomes ineffective.

1.4. Scope and Methodology Overview

To address the research objectives of this study, three concrete mixtures were developed: one control mixture (0% quicklime) and two self-healing mixtures incorporating 2% and 4% quicklime aggregates (by volume of total aggregates). The mechanical properties were assessed through compressive strength and splitting tensile strength tests, while durability was evaluated by measuring drying shrinkage (length change), surface resistivity, abrasion resistance, and freeze–thaw performance.

The primary focus of this research was to assess the crack-healing capability of quicklime-enhanced concrete under simulated environmental exposures. To this end, specimens were pre-cracked with micro and macrocracks and subjected to two cyclic conditioning regimes for 180 days: (1) water and air drying to simulate temperature moisture fluctuations and (2) deicing salt solution and air drying to simulate aggressive environments. The healing performance was evaluated in three complementary phases: (1) Surface-level crack closure monitoring using optical microscopy and a crack width microscope, (2) Depth-wise recovery assessment using ultrasonic pulse velocity (UPV) and water flow tests, (3) Compositional analysis of the healing products via scanning electron microscopy (SEM) coupled with energy-dispersive X-ray spectroscopy (EDS).

1.5. Outline of Report

This report is organized into six chapters. Chapter 1 provides an introduction to this research, including a summary of common deterioration mechanisms in bridge decks, an overview of the concept and relevance of self-healing concrete, the problem statement, research objectives, and a brief outline of the scope and methodology. Chapter 2 presents

a literature review, covering a range of studies that utilize various self-healing agents, and their performance, and limitations. Special attention is given to research involving quicklime-based self-healing concrete, with an emphasis on identifying existing knowledge gaps that this study aims to address. Chapter 3 describes the experimental program in detail. It outlines the mixture designs, selection and proportioning of constituent materials, mixing procedures, and the testing methods employed to evaluate fresh properties, mechanical strength, durability, and self-healing behavior. Chapter 4 reports the results of the experimental investigations, focusing on the influence of quicklime incorporation on fresh and hardened properties, durability characteristics, and crack-healing performance. Results are analyzed to evaluate the self-healing potential of the developed mixtures under simulated service conditions. Chapter 5 concludes the report by summarizing the key findings. Chapter 6 discusses the practical implications of quicklime self-healing concrete for infrastructure applications, offering recommendations for future research.

CHAPTER 2 - LITERATURE REVIEW

This chapter reviews studies on various self-healing mechanisms in cementitious materials, highlighting their ability to seal cracks and improve the durability of concrete structures. These mechanisms are broadly categorized as autogenous and autonomous healing and are discussed in terms of their underlying processes, effectiveness, and limitations in practical applications. Special emphasis is placed on quicklime-based self-healing concrete, with detailed consideration of recent experimental findings and historical examples such as Roman concrete. Through this review, key gaps in the existing literature are identified, which directly inform the objectives and scope of the present research.

2.1. Self-Healing Mechanisms in Cementitious Materials

2.1.1. Autogenous Healing

Autogenous healing in concrete refers to the natural processes that repair minor cracks in concrete without external intervention. As illustrated in Figure 2.1 (a), this process is primarily driven by the formation of calcium carbonate ($CaCO_3$) or calcium hydroxide ($Ca(OH)_2$), which precipitate within cracks and act as sealants. In addition, the presence of particulate impurities along with water, as indicated in Figure 2.1 (b), can help clog the cracks. Further healing occurs through the continued hydration of unreacted cement or cementitious materials, as depicted in Figure 2.1 (c). Lastly, healing may be aided by the swelling and expansion of the hydrated cementitious matrix within the cracks as shown in Figure 2.1 (d). (Talaiekhozani et al. [11]).

Li et al. [12] emphasized that autogenous healing mechanisms in concrete, such as the continued hydration of unhydrated cement particles and the precipitation of calcium carbonate ($CaCO_3$) can effectively seal cracks up to 0.2 mm (0.008 inches) wide by partially filling the crack openings. While these natural processes are inherently limited by crack width and environmental conditions [13], their effectiveness can be significantly enhanced through strategic modifications to the concrete matrix. In particular, incorporating fiber reinforcement and mineral additives has shown promise in improving the extent and reliability of autogenous healing. The following sections discuss the roles of

these enhancements in promoting more efficient autogenous healing in cementitious materials.

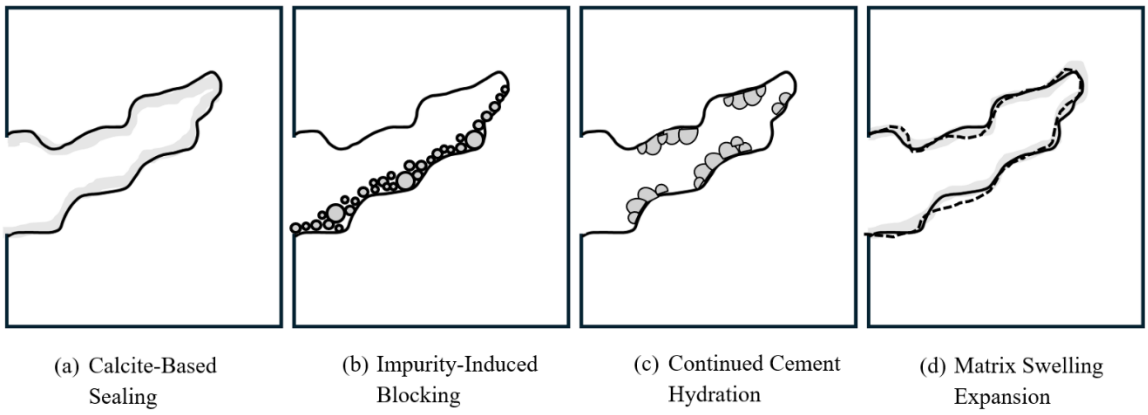

Figure 2.1. Mechanisms for autogenous self-healing in cementitious materials [11].

2.1.1.1. Mineral Additives

Mineral additives such as fly ash, blast furnace slag, high-reactivity metakaolin, granular bentonite, and fine calcium carbonate powder enhance the autogenous self-healing capacity of concrete by promoting secondary hydration through chemical reactions with water. These materials react with unhydrated cement particles or calcium hydroxide in the matrix to form additional binding phases, which can expand and precipitate within cracks, thereby improving crack healing and reducing permeability. For instance, Lee et al. [14] reported a healing index of up to 90% in cracks up to 0.3 mm using mineral-based admixtures embedded in urethane capsules and enhanced mortars. Alternative binders such as fly ash and blast furnace slag have also shown strong potential in hydration-driven healing mechanisms, particularly when used as partial cement replacements [15, 16]. Jiang et al. [17] found that expansive agents and swelling minerals accelerate healing under high pH and elevated temperature, while Suleiman et al. [18] identified calcium carbonate as the dominant healing product in mineral-based healing exposed to wet or cyclic environmental conditions. These findings underscore the capability of mineral additives to support efficient crack sealing and, in some cases, contribute to strength recovery.

Despite these promising outcomes, the effectiveness of mineral-induced healing remains highly sensitive to exposure conditions, particularly moisture availability and temperature, as these factors govern the activation and continuation of the healing

reactions. Studies have also highlighted concerns about the instability of the bond between newly formed healing products and the original concrete matrix, especially calcium carbonate, which may compromise the long-term durability of the repair [19]. In addition, early and uncontrolled consumption of reactive additives such as sodium carbonate may reduce the healing potential over time. Therefore, while mineral additives offer a promising and cost-effective method to enhance autogenous healing, their success depends on careful material selection, dosage control, and exposure to favorable environmental conditions.

2.1.1.2. Fiber-Reinforcement

Fiber-reinforced concrete (FRC) enhances autogenous healing by incorporating fibers that control crack widths and promote the natural self-healing processes of cementitious materials. Unlike autonomous healing that relies on added healing agents, this approach leverages the intrinsic behavior of fibers such as steel, synthetic polymers, or recycled materials to bridge cracks and limit their growth. By keeping cracks sufficiently narrow, fibers create favorable conditions for autogenous mechanisms such as continued hydration of unreacted cement particles and calcium carbonate precipitation to occur.

In particular, Engineered Cementitious Composites (ECC) have demonstrated notable autogenous self-healing capabilities under moisture-rich conditions. Yang et al. [20] reported that ECC specimens subjected to wet-dry cycles, involving both air and oven drying, recovered 76% to 100% of their initial resonant frequency and nearly regained their original tensile strain capacity. In a separate study, Yang et al. [21] demonstrated that early-age ECC cracks (induced at a strain of 0.3%) responded favorably to water exposure, leading to significant restoration of mechanical performance. Zhu et al. [22] further assessed healing behavior of ECC using both non-destructive and destructive techniques, noting that healing products primarily consisted of calcium carbonate and calcium hydroxide.

Fibers not only bridge cracks but also facilitate in-situ formation and retention of healing products. Neves et al. [23] investigated the use of Electric Arc Furnace Slag (EAFS), Fly Ash (FA), and Recycled Tyre Steel Fibers (RTSF) as healing agents. After inducing cracks through tensile splitting tests and submerging the specimens in water, they observed improved ductility, energy absorption, and permeability recovery, despite a minor reduction in strength. Similarly, Nishiwaki et al. [24] demonstrated that synthetic

fibers, particularly polyvinyl alcohol (PVA), enhanced healing by encouraging the precipitation of sealing compounds, thereby reducing water permeability. However, the effectiveness of fiber-based healing mechanism is influenced by multiple factors including fiber type, dosage, distribution, mixture compatibility, and long-term durability. Some fibers may degrade or lose effectiveness over time, and their performance can vary across different environmental or loading conditions. Additionally, the economic costs, energy consumption, and environmental footprint associated with fiber production pose sustainability challenges.

2.1.2. Autonomous Healing

Autonomous healing involves the deliberate incorporation of engineered agents into concrete that actively trigger healing reactions when cracks develop, or environmental conditions change. Unlike autogenous healing, these materials such as bacteria, polymers, or crystalline admixtures are designed to initiate repair processes autonomously, enhancing the ability of concrete to self-repair beyond its natural capacity. The main categories of autonomous healing agents include:

2.1.2.1. Chemical Healing

Chemical healing primarily refers to an artificial method that involves injecting chemical compounds directly into cracks to facilitate repair. The typical chemical compounds are epoxy, methyl methacrylate, or superabsorbent polymers (SAPs). In self-healing concrete, this concept is implemented by embedding encapsulated chemical agents in fresh concrete [11]. Building on this approach, White et al. [25] pioneered the use of microcapsules containing healing agents that are designed to break upon crack formation, releasing their contents to fill the cracks and limit further ingress, as illustrated in Figure 2.2.

Encapsulated healing agents have demonstrated effective crack sealing and partial mechanical strength recovery [11]. Microcapsules and hollow pipettes containing chemical healing agents have shown the potential to restore up to 26% of the original strength after damage [26], while SAPs have been effective in reducing water flow through cracks by 98%, indicating a strong sealing effect [27]. However, the effectiveness of this mechanism is highly dependent on capsule integrity, distribution uniformity, and compatibility with

environmental conditions [28]. As demonstrated by Hilloulin et al. [29] and Snoeck et al. [30], encapsulating materials must survive the harsh conditions of concrete mixing and release healing agents only upon crack formation. Nevertheless, polymer degradation in the alkaline environment of concrete remains a critical limitation. Moreover, incomplete or inconsistent healing, resulting from non-uniform dispersion or premature rupture of the capsules, raises concerns about the long-term durability and reliability of chemical self-healing mechanism. Therefore, although chemical healing offers promising localized repair mechanisms, its practical application requires careful material selection and system design to ensure controlled activation and sustained performance under field conditions.

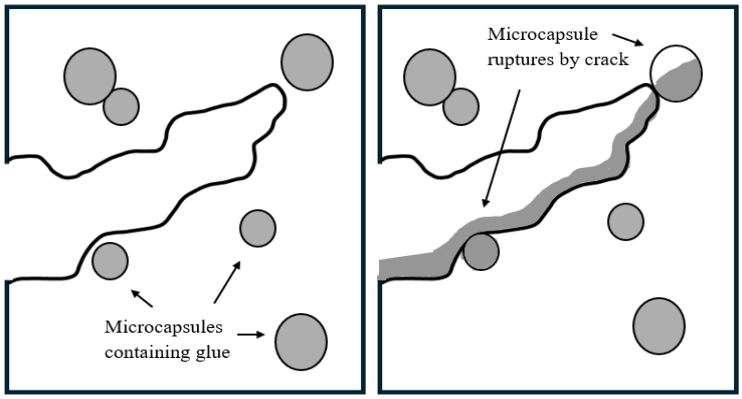

(a) The crack extends deeper into concrete.

(b) The crack breaks the microcapsules, releasing adhesive that flows in and seals the opening.

Figure 2.2. Crack-healing mechanisms using encapsulated glue.

2.1.2.2. Biological Healing

Biologically inspired strategies for designing self-healing concrete have prominently leveraged the use of microorganisms, particularly bacteria. These bacteria are selected for their unique ability to convert nutrients into calcium carbonate ($CaCO_3$), which fills and seals cracks in the concrete (Figure 2.3).

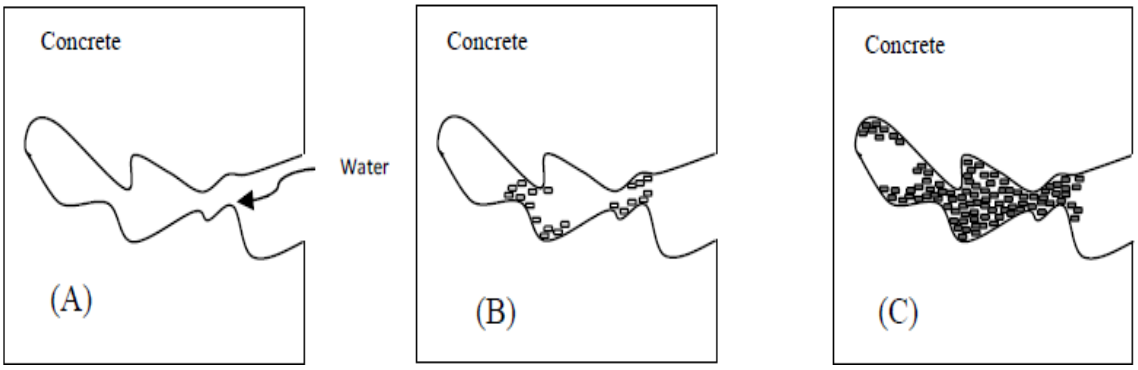

Figure 2.3. Schematic scenario of crack healing by microorganisms (a) crack is propagating into concrete, (b) microorganisms can be activated into crack, (c) microorganisms grow and precipitate calcium carbonate around their wall cells and can fill crack (Taken from Talaiekhozani et al. [11]).

The reviewed studies demonstrated that biological self-healing using bacteria offers a promising approach for crack sealing and durability enhancement in concrete. Bacteria such as Bacillus pasteurii, Bacillus subtilis, and Bacillus cohnii have shown the ability to precipitate calcium carbonate within cracks, effectively reducing water and chloride ingress while modestly recovering mechanical strength [31, 32, 33, 34, 35]. In particular, healing of cracks up to 0.59 mm has been reported, along with improved resistance to freeze-thaw cycles and frost salt scaling [33, 35]. Studies employing encapsulated bacterial spores have also shown effective healing under water immersion conditions, reinforcing the potential for durability enhancement in harsh environments [36]. However, the long-term viability of bacteria in the alkaline concrete matrix remains a critical limitation, as survival and activity may decline over time, thereby affecting healing performance [37]. Additionally, the high cost associated with bacterial incorporation, including encapsulation methods, nutrient supply, and quality control, poses a barrier to large-scale implementation [38]. While biologically driven healing offers an environmentally sustainable solution, its practical application requires optimization of bacterial selection, improvements in microbial durability, and economic feasibility.

2.1.2.3. Crystalline Admixtures Healing

Crystalline admixtures have emerged as a promising agent for enhancing the self-healing performance of concrete by reacting with cementitious components to form insoluble crystalline deposits, sealing cracks and reducing permeability [39]. The

formation of these crystals has been shown to partially restore mechanical properties, particularly when healing occurs in water-rich environments. For instance, Ferrara et al. [16] demonstrated substantial crack closure (70–80%) and property recovery, confirmed through UPV and SEM/EDS analysis under water immersion conditions. Roig-Flores et al. [40, 41] also confirmed the effectiveness of crystalline admixtures in early-age concrete with cracks up to 0.4 mm, showing optimal healing at a 4% admixture dosage under continuous water immersion. Similarly, Sisomphon et al. [42] found that wet/dry cycles or water immersion induced superior healing compared to indoor air exposure, reinforcing the importance of environmental conditions. However, the efficiency of crystalline admixtures is strongly dependent on the availability of water, as their healing mechanism relies on continuous moisture to activate crystal growth. This dependency limits their effectiveness in dry environments. Furthermore, their healing capacity is crack width-dependent; larger cracks may remain only partially sealed, compromising long-term durability. These findings are supported by the study conducted by Palin et al. [43], which reported diminished performance in the absence of a continuous water supply and in the presence of larger cracks.

While various self-healing mechanisms, including bacterial, crystalline, fiber-reinforced, and mineral-based agents, have demonstrated potential in mitigating concrete cracking, each presents specific limitations. Issues such as limited effectiveness for larger cracks, dependency on water availability, high costs, or material degradation over time pose significant barriers to their practical application in critical infrastructure such as bridge decks. These challenges have prompted researchers to explore alternative solutions. Inspired by the exceptional longevity of Roman concrete, quicklime-based agents have gained attention as a promising solution to the limitations of existing self-healing methods. The ability of Roman structures to endure millennia has renewed interest among researchers seeking to enhance the resilience of modern transportation infrastructure, which will be further discussed in the following sections.

2.1.2.4. Quicklime-Based Healing

A notable study was conducted by Seymour et al. [10] who uncovered the self-healing mechanism in ancient Roman concrete. Roman concrete is made by mixing quicklime (CaO) directly with water, volcanic ash, and aggregates (Figure 2.4), producing

chemically active calcium sources and demonstrating exceptional durability over millennia despite exposure to harsh environmental conditions. Jackson et al. [44, 45] provided insights into the durability of Roman concrete through comprehensive investigations of core samples from the Markets of Trajan wall and analog laboratory-recreated specimens. Their findings revealed that Trajanic concrete resists microcracking due to a calcium aluminum silicate hydrate (C-A-S-H) binder, particularly platey strätlingite, that strengthens the interfacial transition zones (ITZ) and reduces the tendency for microcracking within the cementitious matrix. Seymour et al. [10] further explained how pozzolanic material, such as unhydrated volcanic ash or aggregates of volcanic origin dissolve and react with calcium-rich fluids originating from the lime clasts to form C-A-S-H (Equation (2.1)). C-A-S-H reinforces the interfacial zones between volcanic aggregates, ash, and the binding matrix by filling the pores and creating a strong chemical bond.

$$xCa(OH)_2+yAl_2O_3+zSiO_2+(n-x)H_2O \rightarrow \text{(C-A-S-H gel)} \quad (2.1)$$

Additionally, Seymour et al. [10] used the term "hot mixing" to describe the exothermic reaction between quicklime (CaO) and water, which generates substantial heat that can reach high temperatures, creating a rapid hydration environment. In this condition, large particles of quicklime do not fully dissolve or react completely but instead remain as lime clasts encapsulated within the concrete matrix. The outer layer of these lime clasts reacts with available water, silica and alumina, forming a hydration rim which keeps the lime clasts intact. When water seeps through concrete cracks, calcium re-crystallizes as $CaCO_3$ inside the cracks after leaching from the lime clasts and carbonating in the presence of CO_2. (Equation (2.2)).

$$CaO + H_2O \rightarrow Ca(OH)2;\ Ca(OH)_2 + CO_2 \rightarrow CaCO_3 + H_2O \quad (2.2)$$

This dual mechanism, comprising both pozzolanic C-A-S-H formation and crack sealing via $CaCO_3$ precipitation, has been proposed as the source of the exceptional longevity of Roman concrete. Although the durability of Roman concrete has been explored, limited research has focused on tracking the progression of its crack-healing

mechanisms over time, especially under conditions relevant to bridge deck applications. For instance, Seymour et al. [10] investigated crack-healing progression in laboratory-prepared Roman concrete specimens incorporating quicklime, but their study was restricted to a single crack width of 0.5 mm and exposure condition of flowing water for 30 days. However, existing studies fall short in addressing the environmental and mechanical challenges of modern bridge decks, especially in Utah where freeze–thaw cycles, deicing salts, and early-age shrinkage are common. For practical implementation, key factors like workability and compatibility with current placement methods must be evaluated, in light of the exothermic nature of quicklime and its impact on setting, placement, strength development, and long-term performance. Additionally, the mixture must be tailored to the local materials and exposure conditions of Utah. The present study addresses these gaps by developing and assessing a quicklime-based self-healing concrete suitable for durable and constructible bridge deck applications in Utah.

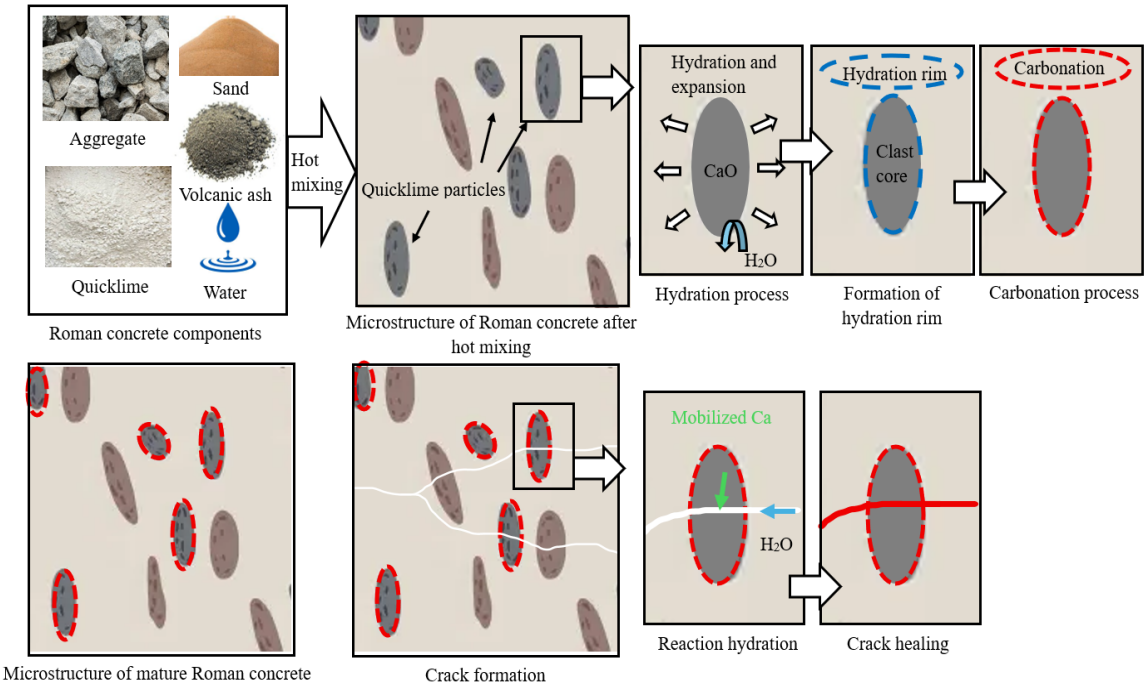

Figure 2.4. Schematic of self-healing mechanism for Roman concrete.

2.2. Bridge Deck Performance Challenges

Cracking in bridge decks poses a critical challenge by compromising structural integrity, accelerating deterioration, and increasing maintenance demands. Cracks in bridge decks are typically categorized based on their orientation into five major types:

longitudinal, transverse, diagonal, map, and random cracks (**Figure 2.5**) Among these, transverse cracks are the most common, which run roughly perpendicular to the longitudinal axis of the bridge and usually appear after casting. Transverse cracks can also be reflective cracks from partial-depth precast deck panels. These cracks often exceed the 0.18 mm (0.007 inches) limit recommended by the ACI Committee 224 [46] and are particularly concerning due to their location directly above transverse reinforcement. Longitudinal cracks, running parallel to the length of the deck, may arise from shrinkage, thermal gradients, or overloading. Diagonal cracks, typically associated with shear or differential settlement, occur at oblique angles. Map cracking, also called crazing, forms a network of fine, interconnected cracks usually caused by surface shrinkage, while random cracks lack a distinct pattern and result from multiple interacting stressors or material deficiencies.

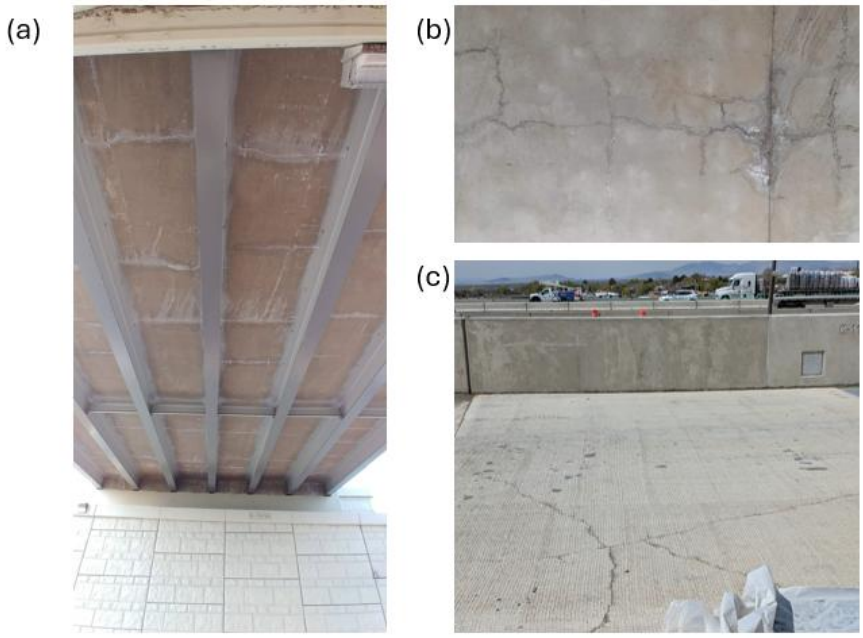

Figure 2.5. (a) Transverse crack, (b) map cracks, and (c) random cracks (Image courtesy: UDOT Structures).

All cracks serve as pathways for moisture, chlorides, and other aggressive agents to penetrate the concrete and reach the steel reinforcement, leading to corrosion, expansion, and further cracking or spalling. This not only weakens the structural capacity of the deck

over time but also reduces its durability and service life. In cold climates, freeze-thaw cycles exacerbate the damage by widening cracks and contributing to surface delamination or pothole formation. Additionally, cracked decks are more difficult and costly to repair, often requiring repeated maintenance interventions or full-depth replacements, which strain infrastructure budgets. Koch et al. [47] quantified the corrosion-related losses of $8.3 billion on highway bridges in 2002, with an even greater economic impact due to traffic delays and lost productivity, roughly 10 times that amount. Beyond structural concerns, cracks diminish the effectiveness of protective overlays or coatings and raise safety and serviceability issues, such as water leakage and uneven driving surfaces. Consequently, addressing crack formation and propagation is essential for ensuring the long-term performance and sustainability of bridge deck systems.

Despite past research on self-healing mechanisms, including quicklime-based systems inspired by Roman concrete, their application in field-like conditions for bridge decks remains underexplored. Most existing studies have been limited to controlled environments, narrow crack widths, and short-term evaluations. Furthermore, literature reviews indicate that the effectiveness of any healing agent depends on critical factors such as its quantity, the range of crack sizes it can address, and the exposure conditions it encounters, which need further research.

2.3. Methods for Self-Healing Evaluation

To assess the performance of self-healing mechanisms, particularly the quicklime-based system examined in this study, it is essential to employ reliable monitoring methods. As self-healing concrete research advances, a wide array of experimental techniques have been developed to assess healing performance from multiple perspectives. These methods include both destructive and non-destructive approaches, ranging from microstructural analyses to mechanical property recovery. For instance, Gagné et al. [48] utilized air-flow measurements and Variable Pressure Scanning Electron Microscopy (VPSEM) to monitor changes in permeability and to visually identify healing products. Ferrara et al. [16] combined Ultrasonic Pulse Velocity (UPV), Optical Microscopy, and SEM to track mechanical recovery and microstructural evolution. Similarly, Cappellesso et al. [33] employed stereomicroscopic crack width measurement, water permeability testing, mercury intrusion porosimetry (MIP), and EDS/SEM analysis to provide a comprehensive

evaluation of healing under freeze-thaw conditions. To capture nanoscale effects, Yoo et al. [49] applied Energy Dispersive X-Ray Spectroscopy (EDS) and Atomic Force Microscopy (AFM) to examine fiber corrosion and healing compound formation. Other researchers, such as Suleiman et al. [18], employed optical microscopy, X-ray computed tomography, SEM, MIP, and EDS to characterize internal crack sealing and pore structure modifications. Water permeability tests and visual crack monitoring have also been widely used in past studies [24, 27, 14, 40, 41, 23, 17], offering practical insights into the rate and extent of crack closure. Furthermore, Zhu et al. [22] combined UPV with direct tensile testing to non-destructively evaluate the mechanical recovery of healed specimens.

Based on previous studies, the evaluation methods selected for this research incorporate multiple complementary techniques to comprehensively assess the healing process. The healing performance was examined through surface-level monitoring using optical microscopy and crack width measurements to observe visible crack closure. This was followed by depth-wise assessment employing ultrasonic pulse velocity (UPV) and water flow tests to evaluate healing through the depth of concrete and permeability recovery. Finally, compositional analysis of the healing products was conducted using scanning electron microscopy (SEM) combined with energy-dispersive X-ray spectroscopy (EDS) to characterize the chemical nature of the material filling the cracks.

2.4. Summary and Research Gap

Various self-healing mechanisms including bacterial, crystalline, fiber-reinforced, and mineral-based agents have shown promise in reducing concrete cracking. However, each approach has notable limitations such as reduced effectiveness on larger cracks, reliance on water availability, high costs, or material degradation over longer time periods. These challenges have led researchers to seek alternative solutions. Inspired by the enduring performance of Roman concrete, quicklime-based self-healing concrete has emerged as a promising alternative. Currently, there is limited research on the crack-healing progression of Roman concrete over time, particularly under conditions relevant to bridge decks. Given that bridge decks face a wider range of crack sizes and harsher environmental exposures, studies focusing on a single crack width or limited conditions are insufficient to fully assess the practical potential of quicklime aggregates. Bridge decks are routinely exposed to cyclic moisture, freeze–thaw action, deicing salts, and early-age

shrinkage, all of which pose challenges to conventional materials. These service conditions, common in regions like Utah, necessitate an evaluation of healing performance across a range of crack widths (micro- and macrocracks) and exposure conditions representative of real-world environments. This study addresses these gaps by investigating the effects of different quicklime dosages, crack sizes, and exposure regimes on healing performance.

CHAPTER 3 - RESEARCH METHODOLOGY

This chapter discusses the development of quicklime-based concrete, detailing the mixture designs, the selection and proportions of constituent materials, the mixing procedure, and the experimental methods used to evaluate its fresh properties, mechanical performance, durability, and crack-healing capability.

3.1. Experimental Program

3.1.1. Materials

The ingredients for the concrete mixtures are locally sourced from Utah. Portland cement Type I/II, with a specific gravity of 3.1 and an average particle size of 17 μm, is procured from Intermountain Concrete Specialties and serves as the primary binder for the concrete. To enrich the cementitious matrix, a percentage of the Portland cement is replaced by volume with Class F fly ash, which has a specific gravity of 2.3, as shown in Table 3.1. Crushed granitic aggregate with a size range of 4.75 to 19 mm and a specific gravity of 2.68 is used as the coarse aggregate. The fine aggregate consists of non-reactive siliceous river sand with a fineness modulus of 2.6, an absorption ratio of 0.3%, and a specific gravity of 2.65. Both coarse and fine aggregates are sourced from Rocky Mountain Landscape Products and meet the ASTM C33 standard [50]. Additionally, quicklime aggregates (shown in Figure 3.1) with an average particle size of 2 mm, a specific gravity of 3.31, and a calcium oxide (CaO) content of 95.5%, as part of the chemical composition summarized in Table 3.2, are used as a partial replacement for the aggregates and are acquired from Graymont. The specific grading details of these aggregates are provided in Figure 3.2. Furthermore, a Sika ViscoCrete-2110 superplasticizer is used to adjust workability as required.

Table 3.1. Physical properties of materials used in concrete composition

Component	Fine Aggregate	Coarse Aggregate	Portland Cement	Fly Ash	Quicklime
Specific Gravity	2.65	2.68	3.10	2.30	3.31

Figure 3.1. Quicklime aggregates.

Table 3.2. Chemical and physical properties of quicklime aggregate (Taken from Graymont specification data sheet)

Component/Property	Quicklime
Total Calcium Oxide (CaO) (%)	95.5
Magnesium Oxide (MgO) (%)	1.3
Silica (SiO_2) (%)	1.7
Ferric Oxide (Fe_2O_3) (%)	0.2
Alumina (Al_2O_3) (%)	0.5
Manganese Oxide (MnO) (ppm)	<50
Total Sulfur (S) (%)	0.02
Loss on ignition (%)	1.3
Calcium Carbonate ($CaCO_3$) (%)	1.8
Temperature rise in 30 seconds (°C)	38
Temperature rise in 3 min (°C)	52
Total temperature (°C)	53
Total active slaking time (min)	4.1

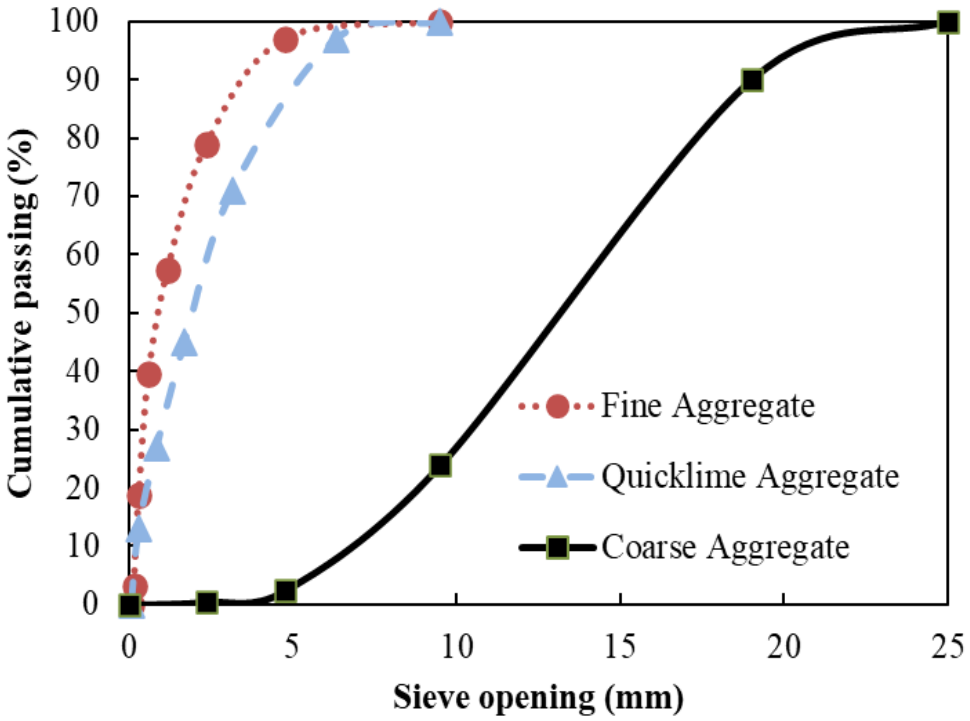

Figure 3.2. Particle size distributions of coarse, fine, and quicklime aggregates.

3.1.2. Mixture Design

In this study, a total of three concrete mixtures were developed. The control mixture contained no quicklime (C-Q 0%), while the other two mixtures incorporated quicklime at 2% (C-Q 2%) and 4% (C-Q 4%) by total mixture volume. The corresponding quicklime volume was then accommodated by replacing an equivalent volume of fine and coarse aggregates. The fine-to-coarse aggregate ratio was maintained constant at 0.7 across all mixtures. All the batches had a constant water-to-binder ratio of 0.44. Additionally, fly ash replaced 20% of the Portland cement volume in all mixtures. The proportions for the control mixture were determined in consultation with the Utah Department of Transportation (UDOT) to replicate typical mixture designs used for concrete bridge decks. For the mixtures incorporating quicklime (C-Q 2% and C-Q 4%), the same parameters as the UDOT control mixture were maintained, including water-to-binder ratio, cementitious material content, and fine-to-coarse aggregate ratio, and the quicklime percentages were adopted based on the range explored in the study by Seymour et al. [10]. The proportions of all three concrete mixtures are shown in Table 3.3.

Table 3.3. Mix proportion of all concrete mixtures in this study

Mixture ID	C-Q 0%	C-Q 2%	C-Q 4%
Cement (lb/yd^3)	669	669	669
Fly ash (lb/yd^3)	167	167	167
Water (lb/yd^3)	371	371	371
Coarse aggregate (lb/yd^3)	1,567	1,518	1,454
Fine aggregate (lb/yd^3)	1,122	1,082	1,057
Quicklime aggregate (lb/yd^3)	–	111	224
Super-plasticizer (lb/yd^3)	–	4.7	9.4

3.1.3. Mixing Procedure

For the mixture preparation, fine and coarse aggregates were first homogenized for 30 seconds. Thereafter, half of the Portland cement and fly ash mixture along with half of the water and superplasticizer were mixed for 3 minutes, followed by a 1-minute resting. The rest of the cementitious materials together with the remaining water and super-plasticizer were added and mixed for 3 minutes. For the two mixtures incorporating quicklime (C-Q 2% and C-Q 4%), after 2 minutes of resting, quicklime was added and mixed for 60-90 seconds. Finally, concrete samples were cast into molds by rodding 25 times in three layers for compaction. After 24 hours, specimens were removed from the molds and air-cured at a temperature of 23±2℃ in a moisture-controlled room until the day of testing.

3.2. Experimental Methods

The fresh properties, mechanical performance, and durability of the developed concrete mixtures were evaluated using a series of standardized tests, while crack-healing was investigated through tailored methods owing to the absence of standardized testing procedures.

3.2.1. Fresh Concrete Properties

3.2.1.1. Slump

Slump measurements for each batch were conducted in accordance with ASTM C143 [51]. Fresh concrete was placed into a slump cone in three layers, with each layer compacted by rodding it 25 times. The cone was then lifted vertically and placed next to

the slumped concrete. The slump was measured as the vertical distance from the top of the cone to the peak of the concrete.

3.2.1.2. Setting Time

The setting time of the fresh concrete mixture was measured according to ASTM C191 [52]. The test began by mixing the dry material and starting a timer as soon as water was added. The concrete was sieved to isolate the paste for the test and poured into a Vicat mold, then leveled. A standardized needle was brought into contact with the surface and set to a zero-reference point. Upon release, the needle penetrated the paste. This step was repeated every 15 minutes until the penetration depth did not exceed 25 mm, indicating the initial setting time, measured from the time of water addition.

3.2.1.3. Post-Casting Temperature

To characterize the thermal effects associated with the highly exothermic hydration of quicklime during hot mixing, which is a process integral to the Roman concrete technology as discussed in Chapter 2, the internal temperature development of each mixture was systematically monitored. Post-casting temperatures were recorded for all mixtures using a thermocouple placed at the center of the mold. The molds were stored at room temperature, and monitoring continued until each batch of concrete reached its peak temperature followed by cooling or stabilizing.

3.2.2. Mechanical Properties

3.2.2.1. Compressive Strength

For all the batches, the compressive strength of 100 × 200 mm cylindrical specimens was measured at 28 and 90 days using a 1300 kN universal testing machine, in accordance with ASTM C39 [53], with at least three replicate samples per test. Figure 3.3 shows the compression test setup. Prior to testing, the cross-sectional dimensions of each cylinder were measured to calculate the corresponding area. During testing, the maximum load sustained by each specimen at failure was recorded, and using these measurements, the corresponding compressive strength was calculated using Equation (3.1).

$$f_c' = \frac{P}{A} \tag{3.1}$$

In this equation, "P" denotes the maximum load applied (N), "A" refers to the cross-sectional area of the cylindrical samples (mm²), and "$f'c$" represents the compressive strength (MPa).

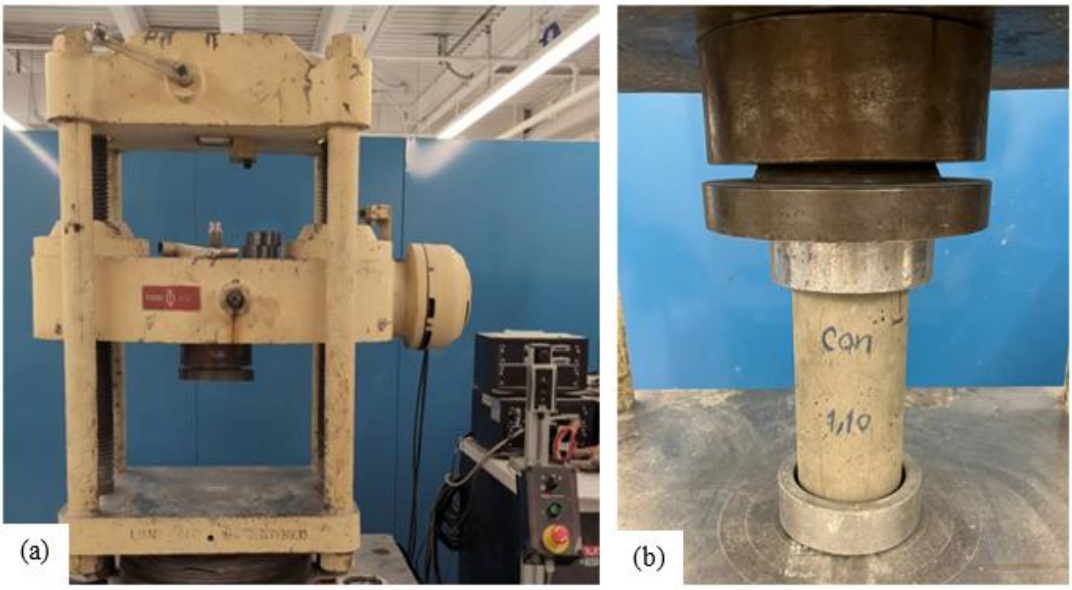

Figure 3.3. (a) Universal testing machine and (b) compression test set up on 100 × 200 mm cylinders.

3.2.2.2. Splitting tensile strength

Cylindrical samples measuring 100 × 200 mm were tested for splitting tensile strength at 28 and 90 days in accordance with ASTM C496 [54]. The splitting tensile strength of the cylindrical samples was determined using a universal testing machine, which facilitated an indirect tension test. The setup used to apply the diametral compressive load, inducing indirect tensile stress to the cylinders, is shown in Figure 3.4. For each age, the reported tensile strength was based on the average value of at least three samples. The peak load, diameter, and length of the cylindrical specimens were recorded to calculate the splitting tensile strength using Equation (3.2).

$$f_t' = \frac{2.P}{L.d.\pi} \tag{3.2}$$

In this equation, "P" represents the peak load (N), "L" denotes the length of the concrete cylinder (mm), "d" indicates the diameter of the cylinder (mm), and "$f't$" signifies the splitting tensile strength (MPa).

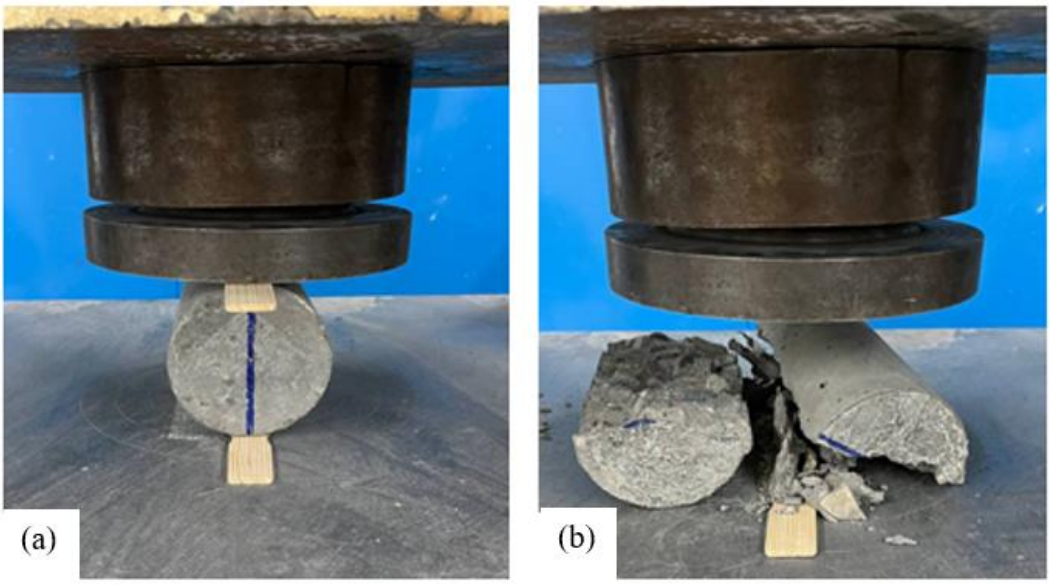

Figure 3.4. (a) Indirect split tension test set up on 100 × 200 mm cylinders and (b) cylindrical specimen post-failure.

3.2.3. Durability Properties

3.2.3.1. Drying Shrinkage

In accordance with ASTM C157 [55], prism specimens with a square cross-section of 75 mm and a length of 285 mm were tested to evaluate drying shrinkage. After demolding, the specimens were immersed in lime-saturated water maintained at 73 °F (23 °C) for a minimum of 30 minutes. Each specimen was removed individually from the water storage, wiped with a damp cloth, and promptly measured for initial length using a comparator. Following this, the specimens were cured in lime-saturated water for 28 days. After the curing period, the specimens were transferred to a controlled drying environment, and comparator readings for each specimen were taken after 7, 14, 28, and 56 days of air curing to assess length changes (Figure 3.5), which were then calculated using Equation (3.3).

$$\text{Length change } (\Delta L_x) = 100 \times \frac{\text{CRD} - \text{initial CRD}}{G} \quad (3.3)$$

"CRD" is defined as difference between the comparator reading of the specimen and the reference bar at any age (mm), and "G" is the gage length (250 mm).

Figure 3.5. (a) Reference bar and (b) drying shrinkage setup on prism specimen.

3.2.3.2. Surface Resistivity

Surface electrical resistivity of cylinders with 100 mm in diameter and 200 mm in length was measured in accordance with AASHTO T 358 [56], as shown in Figure 3.6. Measurements were conducted at 28, 90, and 120 days of curing. The specimens were maintained in a fully saturated condition from the time of demolding until testing. Prior to testing, they were removed from water storage, and their surfaces were wiped to achieve a saturated surface-dry (SSD) condition. During the test, electrical voltage was applied for 60 seconds, and resistance was measured at four circumferential locations of 0°, 90°, 180°, and 270°. The measurement process was conducted twice to calculate the average of the two readings. All measurements were performed at a controlled laboratory temperature of 23 °C. The correlation between chloride penetrability classification and resistivity readings is provided in Table 3.4.

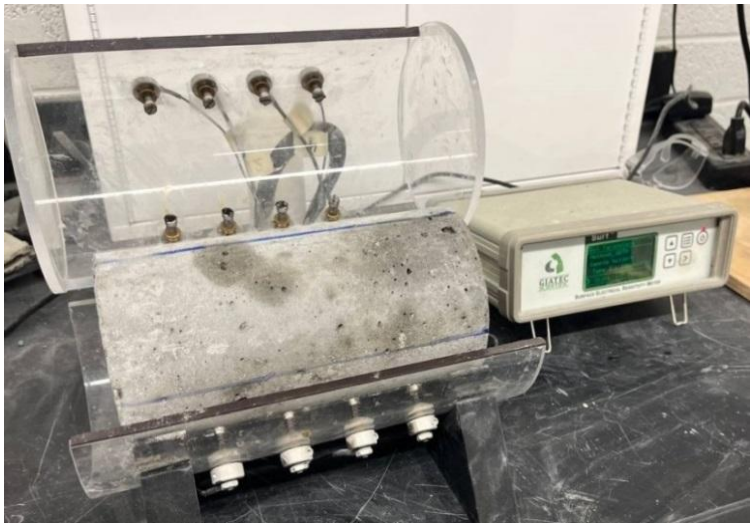

Figure 3.6. The surface electrical resistivity test setup.

Table 3.4. The relationship between chloride penetrability classification and surface electrical resistivity at 23°C

Penetration	Resistivity (kΩ.cm)
High	<12
Moderate	12-21
Low	21-37
Very Low	37-254
Negligible	>254

3.2.3.3. Abrasion Resistance

Cylindrical specimens measuring 100 mm in diameter and 200 mm in height were cast and tested for abrasion resistance at 28 and 90 days of curing, following the procedure outlined in ASTM C1747 [57]. Three specimens were placed in the steel drum of a Los Angeles abrasion testing machine and subjected to a total of 500 revolutions. After every 100 revolutions, the drum was discharged, and the mass of the remaining specimens was recorded. Abrasion resistance was determined by measuring the mass loss of the specimens using Equation (3.4).

$$ML(\%) = 100 \times \frac{M2-M1}{M1} \quad (3.4)$$

In this equation, “ML” denotes the mass loss percentage, while “M2” and “M1” are the final and initial masses of the specimens (g), respectively.

3.2.3.4. Freeze-Thaw Resistance

Concrete samples cured for 28 days were tested to evaluate freeze-thaw (FT) resistance. A freeze-thaw chamber meeting ASTM C666 [58] specifications was used to expose 100 × 200 mm cylindrical specimens to cyclic freezing and thawing. Each cycle involved cooling from +4 °C to –18 °C, followed by warming back to +4 °C, with a total cycle duration of 3 hours. After every 30 cycles, the samples were removed, weighed to determine mass loss, and tested for changes in dynamic modulus of elasticity according to ASTM C215 [59] using resonant frequency test (Figure 3.7).

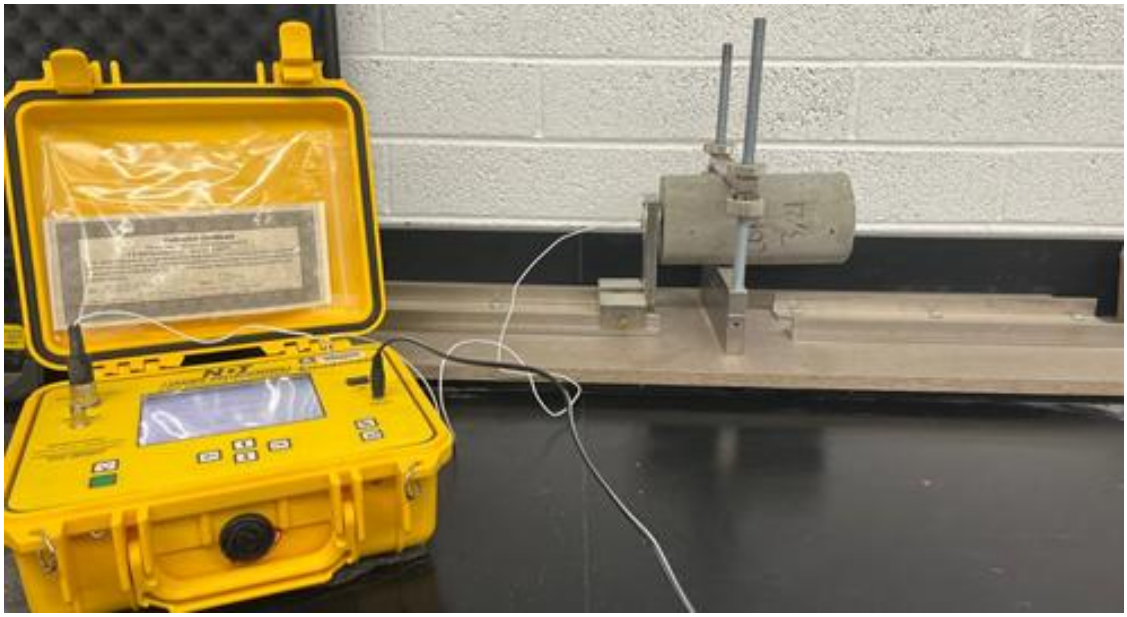

Figure 3.7. Frequency measurement using resonant frequency test.

The reported mass loss and dynamic modulus of elasticity values represent the average of at least four specimens. Testing continued until either 300 freeze-thaw cycles were completed or until the specimens reached a 15% mass loss. Mass loss was calculated using the following equation:

$$ML(\%) = 100 \times \frac{M2-M1}{M1} \quad (3.5)$$

where “ML” denotes the mass loss percentage, while “M2” and “M1” are the final and initial masses of the specimens (g), respectively. The dynamic modulus of elasticity (E) was calculated using the following equation:

$$Dynamic\ E = CMn^2 \quad (3.6)$$

where “M” is mass of specimen (kg), “n” is resonant frequency (Hz), “C” is a constant equal to 1.6067× (L^3×T/d^4) (m^{-1}), wherein “T” is a correction factor that depends on the ratio of the radius of gyration to length, and “L” and “d” are length and diameter of specimen (m), respectively.

3.2.4. Crack Healing Capability

The effectiveness of crack healing in the concrete test specimens was evaluated after 28 days of curing. Microcracks with widths ranging from 100 to 200 μm (0.004–0.008 inches) and 200 to 300 μm (0.008 to 0.012 inches), and macrocracks with widths ranging from 300 to 550 μm (0.012 to 0.022 inches), were created in specimens from all three batches. To induce these cracks, cylindrical concrete specimens (100 × 200 mm/ 4 × 8 inches) were first cut into disks measuring 50 mm (2 inches) in height and 100 mm (4 inches) in diameter. A 5 mm (0.2 inches) notch was introduced on each disk to create a controlled splitting plane, as shown in Figure 3.8 (a). The specimens were then subjected to indirect tensile loading, causing them to split into two halves (Figure 3.8 (b-c)). Subsequently, flexible silicone sheets were placed between the split sections, covering 15 mm at each end (Figure 3.8 (d)). To maintain a controlled crack width along the remaining contact area, a stainless-steel band with a clamp was utilized to hold the portions together (Figure 3.8 (e)). Two exposure scenarios were employed to replicate the exposure conditions on bridge decks: (i) cyclic exposure to water and air-drying, and (ii) cyclic exposure to deicing salt solution and air drying. The deicing salt solution was 20% in concentration and was prepared by dissolving 200 grams of deicing salt in 1000 grams of water. This deicing salt was sourced from Logan UDOT Shed and comprised 98.8% sodium chloride (NaCl) by weight with remaining contents as 0.4% sulfate (SO_4), 0.09% calcium (Ca), and 0.19% magnesium (Mg). In both scenarios, each cycle consisted of 3.5-days wetting period, followed by a 3.5-days air exposure period, repeated continuously over a 180-day healing period. The six specimen groups, categorized by crack width, quicklime content, and exposure condition, are summarized in Table 3.5.

Table 3.5. Specimen groups by quicklime content, crack width, and exposure condition

Group ID	Quicklime Content (%)	Crack Width (μm)	Crack Width (inches)	Exposure Condition
W-MICRO1-Q (0-4%)	0,2,4	100-200	0.004–0.008	Water/air cycles
W-MICRO2-Q (0-4%)	0,2,4	200-300	0.008–0.012	Water/air cycles
W-MACRO-Q (0-4%)	0,2,4	300-550	0.012–0.022	Water/air cycles
DS-MICRO1-Q (0-4%)	0,2,4	100-200	0.004–0.008	Deicing salt solution/air cycles
DS-MICRO2-Q (0-4%)	0,2,4	200-300	0.008–0.012	Deicing salt solution/air cycles
DS-MACRO-Q (0-4%)	0,2,4	300-550	0.012–0.022	Deicing salt solution/air cycles

Crack closure was monitored using a crack width microscope and optical microscopy for surface-level observations. However, surface observations alone do not capture the extent of healing within the bulk of the material. To assess the degree of crack healing throughout the depth of the specimens, water flow tests and Ultrasonic Pulse Velocity (UPV) measurements were conducted. In addition, Scanning Electron Microscopy (SEM) and Energy Dispersive X-Ray Spectroscopy (EDS) were employed to analyze and characterize the composition of the crack-fill materials. These complementary methods collectively offer a thorough evaluation of both surface and internal crack healing, detailed in the following sections.

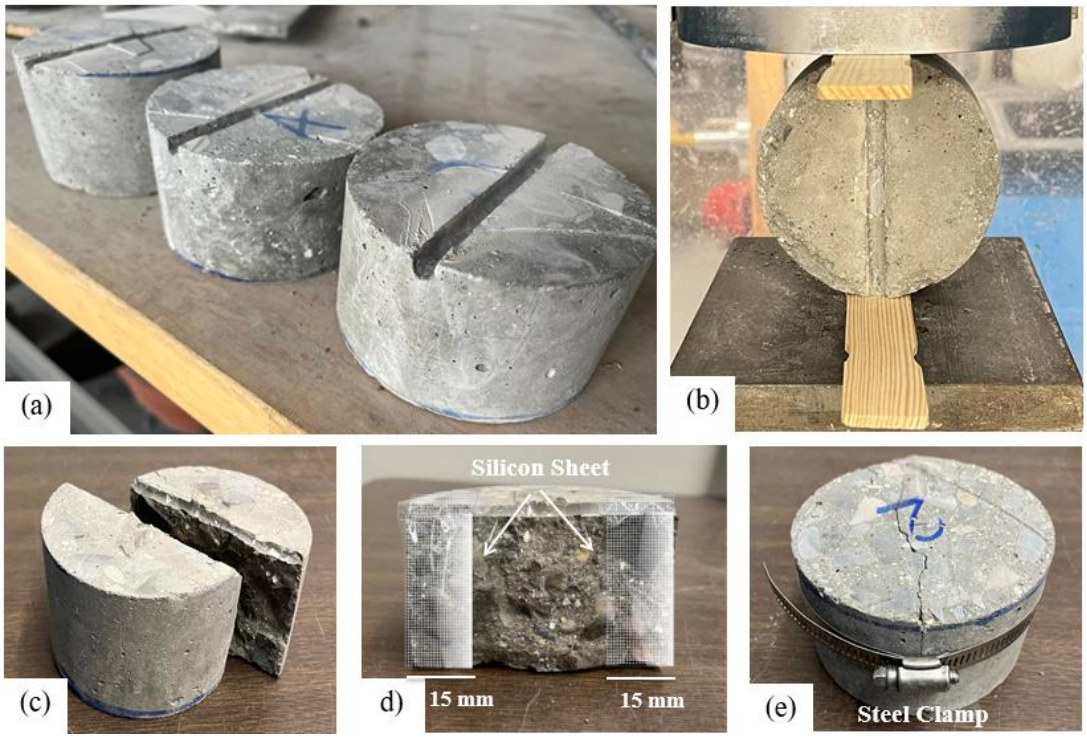

Figure 3.8. Preparation of cracked specimens: (a) 5 mm notch for splitting plane, (b) Split specimen setup, (c) Specimen split into two halves, (d) Silicone sheet is located between sections, (e) Sections are bound together with a steel band.

3.2.4.1. Surface-Level Crack Healing Monitoring

To trace the self-healing performance of both micro- and macrocracks on the surface of the concrete specimens, optical microscopy and a crack width microscope were utilized. While the crack width microscope was used for preliminary, qualitative observations to monitor general closure trends, only the images captured via optical microscopy at specified intervals of day 0 (initial reading) and at 60, 120, 160, and 180 days were analyzed using ImageJ software to quantitatively measure crack widths. Even though cracks were created in a controlled manner for all specimens, variations in crack width along the length of the induced crack were observed. To address this, three locations along each crack were selected for measurement, and their average was used to represent the crack width at a given time, as illustrated in Figure 3.9. This method helped to ensure consistent measurements for tracking crack closure over time.

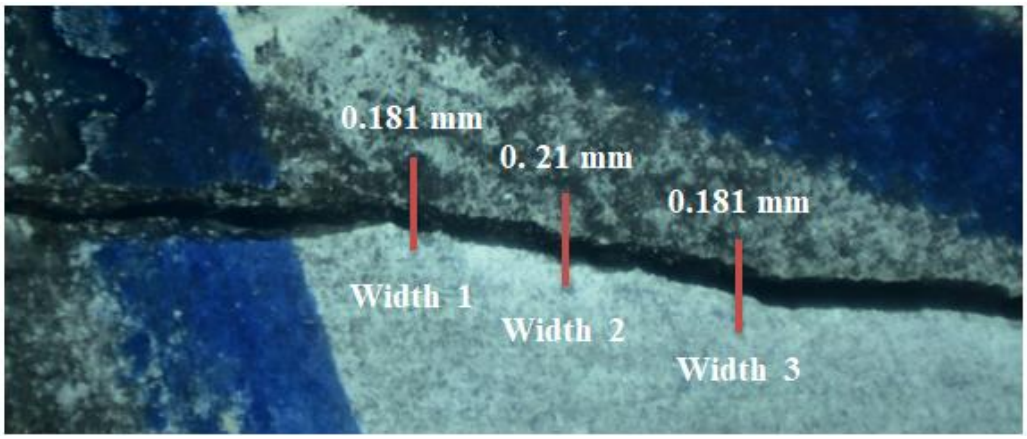

Figure 3.9. Crack widths at three locations along the crack for calculating average crack width.

The extent of surface healing is quantified in terms of crack closure percentage and is calculated according to Equation (3.7), using the average of the three crack width measurements taken over a period of time. In this equation, "$w_{initial}$" is the average of the crack widths measured on day 0, and "w_t" denotes the average of crack widths at time "t", where "t" is the specific healing time at which the magnitude of crack closure is calculated.

$$Crack\ closure\ (\%) = [1 - \frac{w_t}{w_{initial}}] \times 100 \quad (3.7)$$

3.2.4.2. Depth-Wise Crack Healing Monitoring

The Ultrasonic Pulse Velocity (UPV) test was employed to track the healing progress throughout the depth of cracks. The UPV test is a non-destructive technique for evaluating concrete quality and was conducted using the Humboldt HC-6390 UPV Tester in this study. The test measured the travel time of an ultrasonic pulse between a pair of transducers placed on the opposite flat circular surfaces of 100 mm (4 in.) diameter × 50 mm (2 in.) thick concrete disks (the same specimens used for surface crack monitoring). The transducers were placed 50 mm apart, corresponding to the depth of the disks, which is the effective path length of the pulse (Figure 3.10).

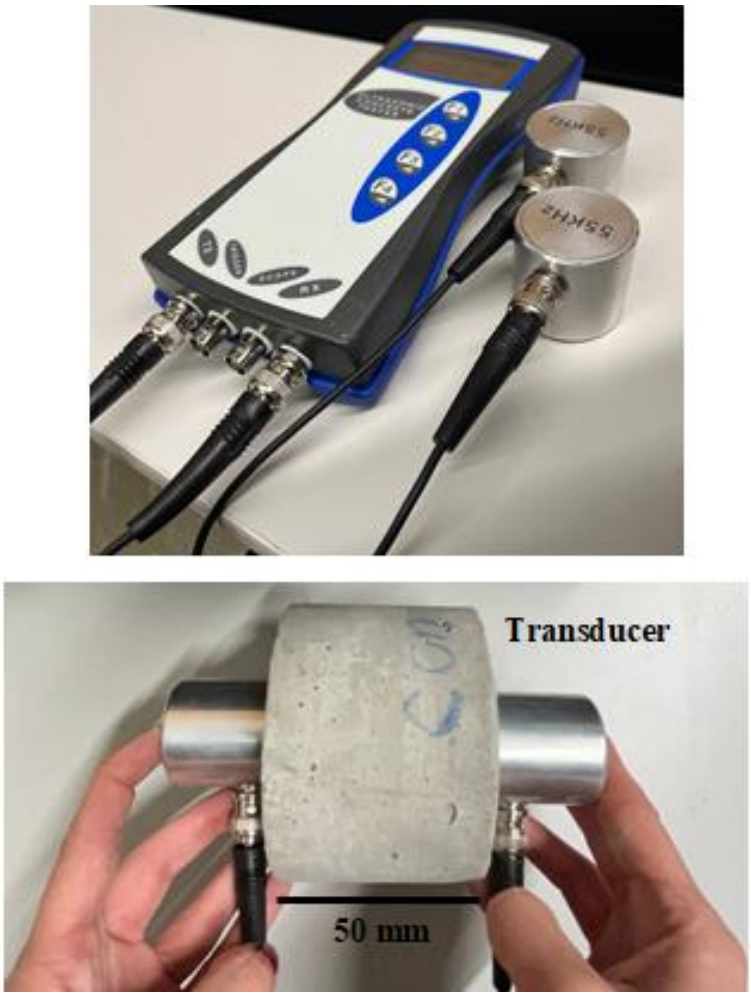

Figure 3.10. Ultrasonic pulse velocity (UPV) apparatus.

UPV measurements were taken at 0, 60, 120, 160, and 180 days on the same specimens during the healing process. The pulse velocity was calculated by dividing the travel distance (50×10^{-6} km) by the recorded travel time. The results are presented as the percentage increase in UPV, calculated using Equation (3.8). In this equation, "$V_{initial}$" is the pulse velocity (km/s) measured on day 0, and "V_t" is the pulse velocity at time "t," representing a specific healing duration at which the UPV increase is evaluated.

$$Relative\ improvement\ in\ UPV\ (\%) = [1 - \frac{V_t}{V_{initial}}] \times 100 \quad (3.8)$$

To contextualize the UPV results, Table 3.6 presents the correlation between pulse velocity, modulus of elasticity (MOE), and concrete quality. The MOE values were calculated according to the ASTM C597 standard [60] using Equation (3.9). Where "E" is

the modulus of elasticity (GPa), "ρ" is the density (kg/m³), "V" is the ultrasonic pulse velocity (km/s), and "μ" is the Poisson's ratio.

$$E = \rho V^2 \frac{(1+\mu)(1-2\mu)}{(1-\mu)} \quad (3.9)$$

The density of the quicklime-based concrete was measured to be 2451 kg/m³ (4,128 lb/yd³). Using the Emodumeter data, the dynamic modulus of elasticity (E) and shear modulus (G) were found to be 45 GPa and 18.4 GPa, respectively, resulting in Poisson's ratio of 0.22 (μ=2GE−1). Based on this table, higher pulse velocities correlate with higher MOE values, both of which indicate a denser concrete matrix with fewer pores and cracks, and in turn, improved internal crack healing.

Table 3.6. Relationship between pulse velocity and quality of concrete

Pulse Velocity (km/S)	Modulus of Elasticity (GPa)	Quality of Concrete
Above 4.5	Above 43	Excellent
3.5 to 4.5	26 to 43	Good
3.0 to 3.5	19 to 26	Medium
Below 3.0	Below 19	Doubtful

To evaluate the self-healing performance through the depth of the cracks, water flow testing using the falling head permeability method [61, 62] was also conducted as an additional test on selected disk specimens. This test was performed on 100 × 50 mm concrete disks that had exhibited complete surface crack closure, previously used for optical microscopy and UPV measurements. The fully closed surface-crack specimens were placed inside a PVC ring and secured with PVC pipe cement glue. The PVC ring was then attached to a graduated cylinder and sealed with a clear waterproof sealant to ensure no leakage. The entire assembly was positioned on a meshed basket to allow water passage (Figure 3.11). Before testing, water was poured into the graduated cylinder to fill the specimen cell to a specific height. The time required for water to flow from the initial head (h_1) to the final head (h_2) was recorded in seconds. In this study, water flow was recorded over a 24-hour period. The water flow test was used to evaluate the effectiveness of crack sealing solely on specimens with visually confirmed full-surface crack closure because it was a sacrificial test and monitoring of unhealed specimens is still ongoing for long-term

studies. Using Equation (3.1), permeability coefficients are calculated at the end of the healing process, indicating effective crack healing.

$$K = \frac{a \times L}{A \times t} \ln\left(\frac{h_1}{h_2}\right) \quad (3.10)$$

In this equation, “K” represents permeability coefficient (mm/s), ”a” is the cross-sectional area of the pipe (mm^2), “A” is the cross-sectional area of the specimen (mm^2), ”L” is length (mm), ”t” is time (s), and h_1, h_2 are initial and final water heads (mm) respectively.

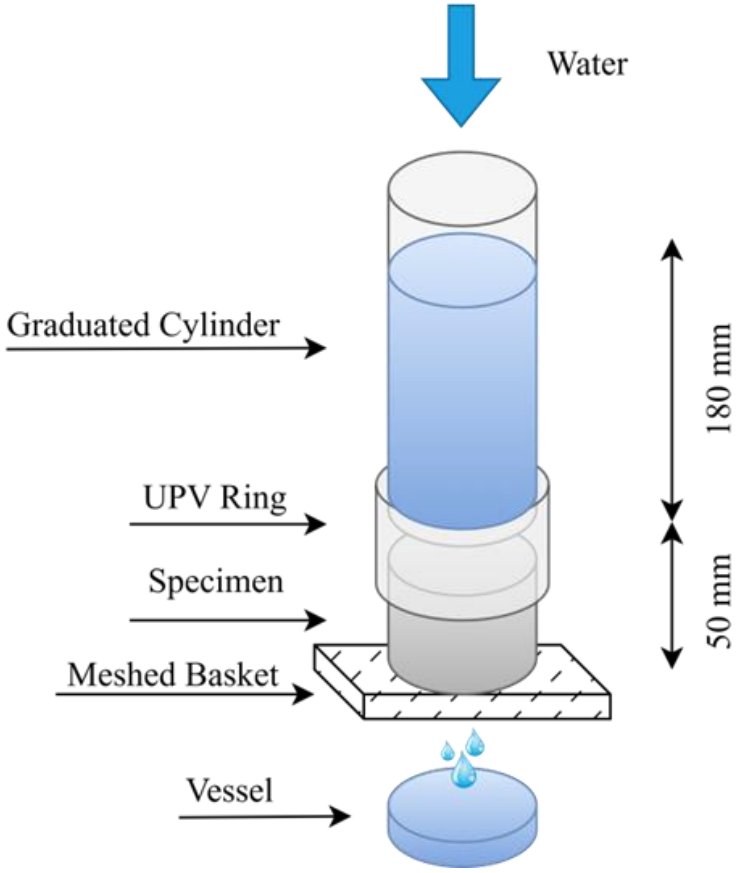

Figure 3.11. Water-flow test setup

3.2.4.3. SEM-EDS Analysis of Crack-Filling Products

To investigate the composition of the materials filling the cracks in the concrete specimens, scanning electron microscopy (SEM) combined with energy dispersive spectroscopy (EDS) was employed. SEM-EDS analysis was conducted on healing products extracted from two sets of specimens containing 0%, 2%, and 4% quicklime, selected to

represent varying crack widths, exposure environments, and healing mechanisms. The first set, which included specimens with microcracks ranging 100-200 μm, was exposed to cyclic water and air-drying. The second set, containing specimens with macrocracks (300–550 μm), underwent cyclic exposure to a 20% deicing salt solution and air-drying. These specimens were selected to represent a range of crack widths, healing environments, and quicklime contents, allowing for a comparative evaluation of the influence of each variable on the composition of healing products. After 180 days of healing, powder samples were extracted from the surfaces of the reopened cracks and mounted on double-sided carbon tape for SEM-EDS analysis Figure 3.12(a). These samples were gold-coated to enhance conductivity before being examined in a high-vacuum chamber. The analysis was conducted using a Quanta FEG 650 scanning electron microscope (SEM) at an accelerating voltage of 10 kV. Elemental mapping was performed across the entire sample area to visualize the spatial distribution of key elements. Additionally, point-and-ID analysis was conducted at approximately 20 locations per sample to obtain localized quantitative data. To minimize charging artifacts, the measurements were acquired using a concentric backscatter (CBS) detector EDS system.

In addition to crack-fill analysis, solid samples from various regions of the matrix in concrete specimens, as shown in Figure 3.12 (b), containing 2% and 4% quicklime were examined using SEM to detect quicklime-induced expansion and hydration rim formation around the quicklime aggregates. These solid samples were gold-coated and analyzed in a high-vacuum chamber at an accelerating voltage of 10 kV, using an Everhart-Thornley detector (ETD) to capture secondary electrons for imaging.

(a)

(b)

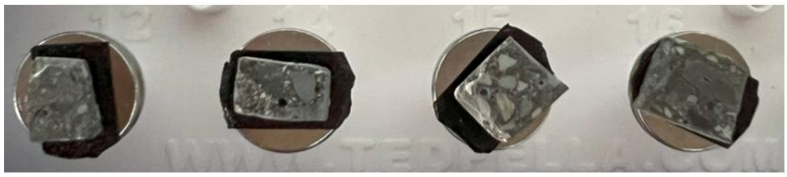

Figure 3.12. (a) Powder samples for SEM-EDS analysis of healing products; (b) Solid samples to observe quicklime-induced cracking and hydration rims.

3.2.4.4. Strength Recovery of Healed Specimens

To quantify the compressive strength recovery of healed specimens, microcracks with widths ranging from 100 to 200 μm (0.1 to 0.2 mm) and 200 to 300 μm (0.2 to 0.3 mm) were induced on 28-day cylindrical specimens (100 × 200 mm) with 2% and 4% quicklime content, as shown in Figure 3.13(a). The initial crack widths were maintained using silicone sheets.

One set of these pre-cracked specimens was exposed to cyclic water/air-dry conditions, while the other set was subjected to 20% deicing salt solution/air-dry cycles for 180 days. After the healing period, the compressive strength of the specimens was measured using a 1300 kN universal testing machine (Figure 3.13(b)). The reported compressive strength values represent the average of at least two specimens for each condition. Using Equation (3.11), the strength recovery percentage is calculated for each set of specimens, where “Residual f'c” denotes the compressive strength of the healed specimen (MPa), and “f'c” is the 28-day compressive strength of the uncracked specimen (MPa).

$$Strength\ Recovery\ (\%) = \frac{Residual\ f_c'}{f_c'} \times 100 \tag{3.11}$$

This evaluation facilitates a quantitative assessment of the mechanical performance recovery attributable to quicklime-based healing mechanism under controlled environmental conditioning representative of in-service exposure for bridge decks.

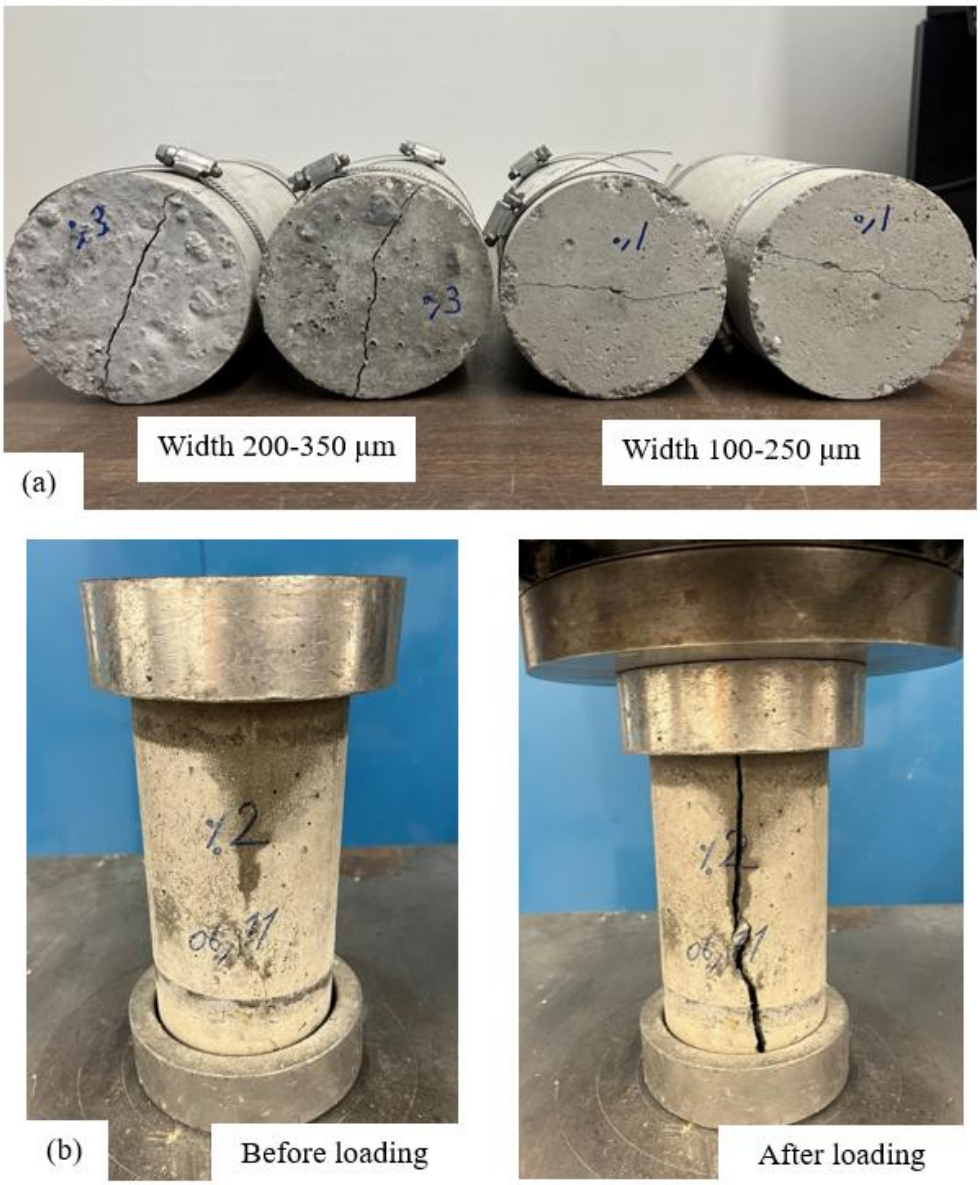

Figure 3.13. (a) Pre-cracked cylindrical specimens with controlled crack widths, and (b) compressive strength measurement of healed specimens using a universal testing machine.

CHAPTER 4 - RESULTS AND DISCUSSION

This chapter presents the results of experimental investigations on quicklime-based concrete, focusing on its fresh properties, mechanical performance, durability, and crack-healing capability. The outcomes are analyzed to understand the effects of quicklime incorporation on concrete properties and to assess the potential of the developed mixtures for self-healing performance.

4.1. Fresh Concrete Properties

The addition of quicklime to the concrete mixtures significantly reduced their workability, resulting in stiffer and less manageable fresh concrete. This reduction is primarily attributed to water consumption of quicklime aggregates during hot mixing due to their partial hydration and the heat generated by this exothermic reaction [10, 63]. Additionally, quicklime has a high water absorption rate of 32% [64], which further increases the water demand and contributes to the reduction in workability. To compensate for the loss in workability, superplasticizer was added at dosages of 0.7% and 1.4% by volume of cement for the C–Q 2% and C–Q 4% mixtures, respectively. The modified mixture designs incorporating superplasticizer showed improved slump values of 200 mm (8 in.) for both C-Q 2% and C-Q 4%, compared to 100 mm (4 in.) for the control mixture (C-Q 0%), as shown in Figure 4.1.

Quicklime addition also led to a substantial rise in temperature due to its exothermic reaction with water, noted as hot mixing in the literature. As shown in Figure 4.2, C-Q 0% remained at ambient temperature (~23°C or 73°F) after 237 minutes (4 hours), while C-Q 2% and C-Q 4% reached higher peak temperatures of 33°C (91.5 °F) and 46°C (115°F) within 36 minutes (0.6 hour) and 27 minutes (0.45 hour), respectively. The observed increase in temperature correlates with the amount of quicklime added, as higher dosages lead to more intense hydration. This reflects the intensity of the exothermic reaction, wherein calcium oxide (CaO) reacts with water (H_2O) to form calcium hydroxide ($Ca(OH)_2$), releasing a significant amount of heat. This behavior is concerning from a mass concrete perspective, as partial insulation from formwork can trap heat. Even comparatively thin sections may reach internal temperatures above 160°F. This reaction accelerates early cement hydration, particularly of tricalcium silicate (C_3S). Similar

findings were observed by Commandré et al. [65], with the temperature of lime-based mortar reaching 60°C (140°F). The higher temperatures encountered during quicklime mixing led to the formation of hydration gradients around the lime clasts, which can create a reaction rim that prevents them from dissolving further within the concrete matrix.

Figure 4.1. Slump test for (a) C-Q 0%, (b) C-Q 2% and (c) C-Q 4% after the addition of superplasticizer.

The initial setting time for C-Q 0%, C-Q 2%, and C-Q 4% was measured as 74, 40, and 21 minutes, respectively. The initial setting times decreased with increasing quicklime content, and this is attributed to the heat generated during quicklime hydration and the corresponding reduction in free water, both of which expedite setting time. These findings are consistent with previous research on lime-modified cementitious systems [66, 67, 68].

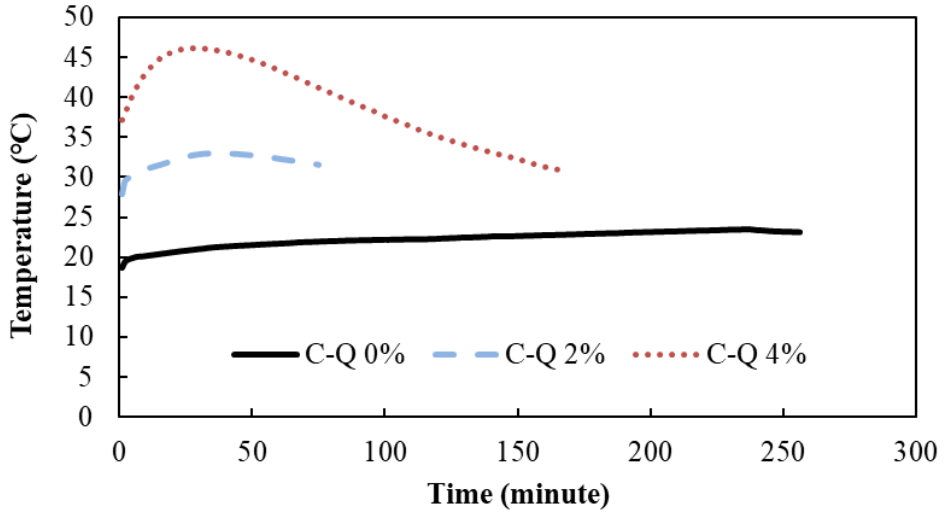

Figure 4.2. Progression of post-casting temperatures in concrete batches.

4.2. Mechanical Properties

4.2.1. Compressive Strength

The compressive strength tests were performed at the ages of 28 and 90 days for all concrete specimens and the results are presented in Figure 4.3. At 28 days, the compressive strengths of C-Q 0%, C-Q 2%, and C-Q 4% were 33 MPa (4,786 psi), 43 MPa (6,235 psi), and 53 MPa (7,687 psi), respectively. At 90 days, strength increased for all mixtures, with C-Q 0% reaching 37 MPa (5,366 psi), C-Q 2% reaching 48 MPa (6,962 psi), and C-Q 4% reaching 58 MPa (8,412 psi). These results indicate that compressive strength improved with increasing quicklime content. The greatest improvement was observed for the specimens with 4% quicklime, which showed a 63% and 59% increase in compressive strength at 28 and 90 days, respectively, compared to the control mixture.

This enhancement in compressive strength can be attributed to several factors. First, the reaction between quicklime and the cementitious environment leads to the formation of additional calcium silicate hydrate (C-S-H) gel, through reactions between the available silica (SiO_2) and alumina (Al_2O_3) in the presence of quicklime, thereby contributing to further strength development [10, 44, 69, 70]. Additionally, the filler effect of quicklime particles improves the packing density and contributes to a denser interfacial transition zone between the concrete matrix and the aggregates, further increasing the compressive strength of concrete. This observation aligns with the findings of Acharya et al. [63], who reported that replacing up to 7% of cement with hydraulic lime enhances the compressive strength of concrete. Furthermore, the high water absorption capacity of quicklime (32%), coupled with its exothermic reaction, reduces the amount of free water in the mixture, limiting evaporation during curing and potentially lowering porosity. This leads to denser microstructure, contributing further to the observed increase in compressive strength.

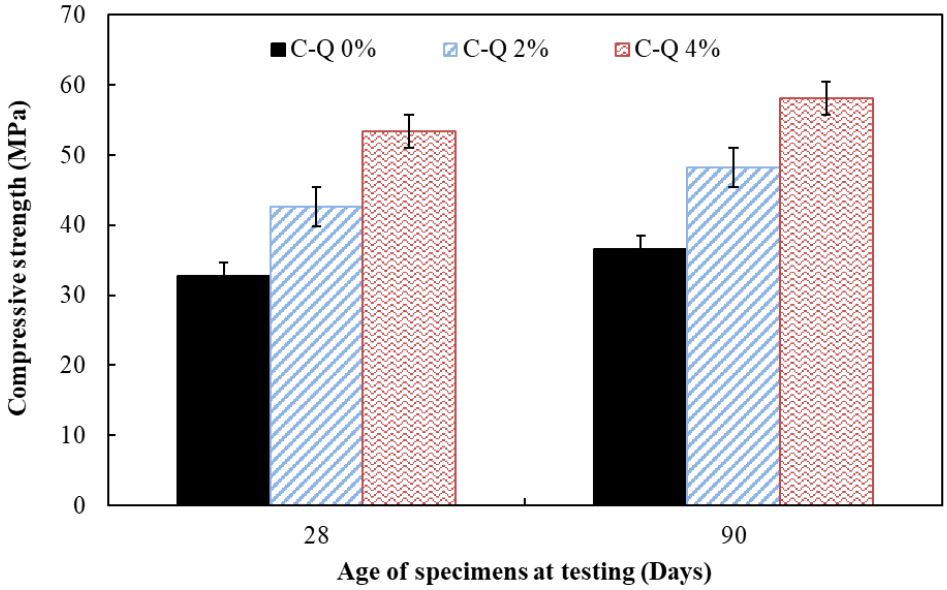

Figure 4.3. Compressive strength of all concrete mixtures at 28 and 90 days.

4.2.2. Splitting Tensile Strength

The splitting tensile strength results at 28 and 90 days for all concrete mixtures are presented in Figure 4.4. At 28 days, the control mixture (C-Q 0%) exhibited a splitting tensile strength of 3.3 MPa. This value increased by 35.3% to 4.5 MPa and by 54.3% to 5.15 MPa with the replacement of 2% and 4% quicklime aggregates, respectively. At 90 days, the strength further increased to 5.4 MPa for specimens with 2% quicklime (a 36.3% increase) and to 6 MPa for those with 4% quicklime (a 52.3% increase).

The ratio of splitting tensile strength to compressive strength ranged from 9.6% to 10.5% at 28 days and from 10.3% to 11.2% at 90 days. These values fall within, or slightly exceed, the typical range of 8% to 10% reported for normal to medium-strength concrete [71]. Overall, the trend in splitting tensile strength mirrored that of compressive strength, showing a consistent strength increase with higher quicklime content. This enhancement in tensile strength can be attributed to the formation of additional calcium silicate hydrate (C–S–H) gel, which fills the pores and contributes to a denser interfacial transition zone between the aggregate and the cement matrix facilitated by the presence of quicklime.

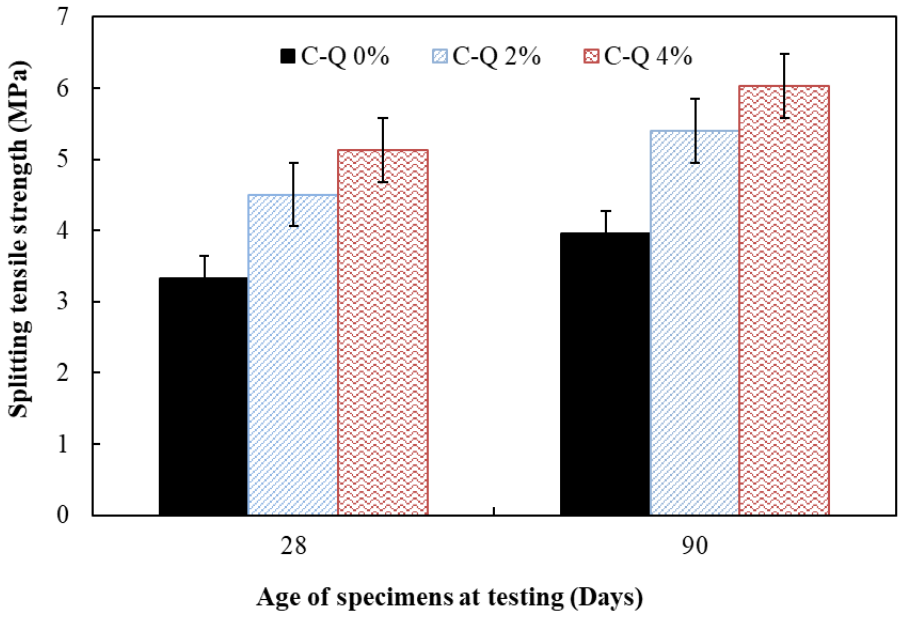

Figure 4.4. Splitting tensile strength of all concrete mixtures at 28 and 90 days.

4.3. Durability Properties

4.3.1. Drying Shrinkage

The effect of quicklime content on drying shrinkage was assessed over a 56-day air exposure period. Figure 4.5 presents the average length change (%) for C-Q 0%, C-Q 2%, and C-Q 4% specimens measured at 7, 14, 28, and 56 days. The results indicate that the concrete mixture with 4% quicklime content exhibited a greater degree of drying shrinkage compared to the C-Q 0% and C-Q 2% specimens. Shrinkage increased with quicklime content; at 56 days, C-Q 0% measured 0.031%, compared with 0.130% for C-Q 2% and 0.200% for C-Q 4%. Thus, the control mixture's shrinkage magnitude is about 76% and 85% lower than the 2% and 4% mixtures, respectively. In practical terms, C-Q 2% experienced about 4.2 times the shrinkage of the control mixture, and C-Q 4% experienced 6.5 times the shrinkage of the control. UDOT specifies a maximum allowable deck shrinkage of 0.035%; the control meets this requirement, whereas the quicklime mixtures exceed it.

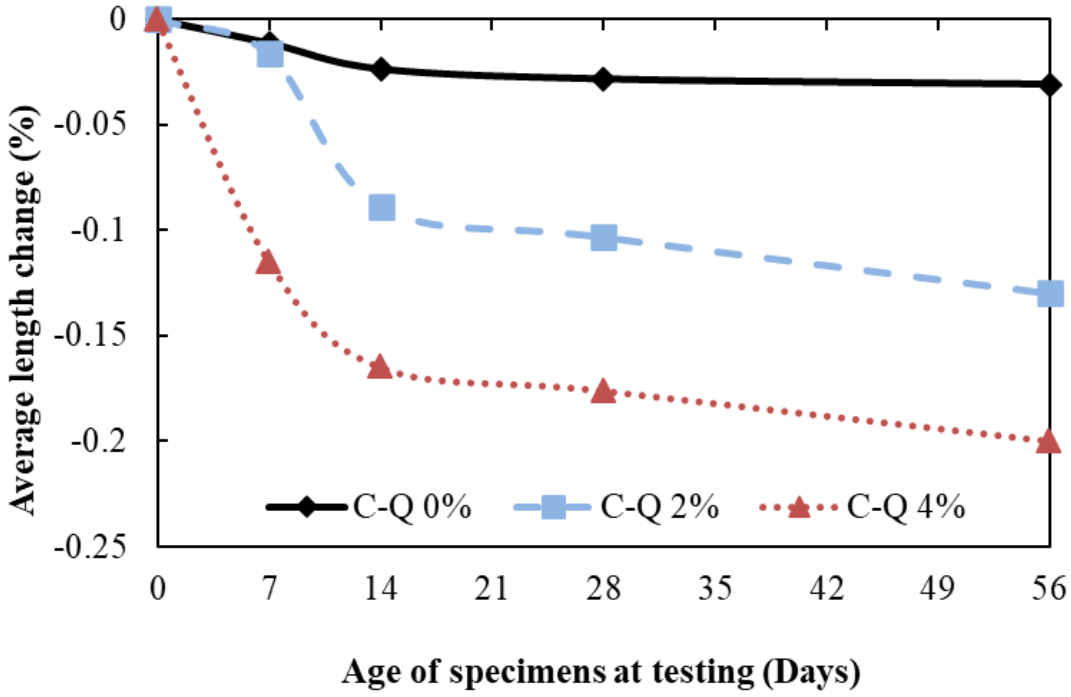

Figure 4.5. Average Length Change (%) of specimens.

This trend is consistent with findings of Pozo-Antonio [72], who reported that mortars composed purely of lime experienced higher shrinkage than those containing both lime and cement. The increased shrinkage can be attributed to the tendency of quicklime aggregates to raise the water demand of the concrete mixture, due to the heat released during their hydration and their inherently high-water absorption capacity. Furthermore, quicklime actively participates in hydration reactions, leading to the formation of calcium silicate hydrate (C–S–H) gel, resulting in volumetric contractions during setting and drying, thereby increasing shrinkage.

4.3.2. Surface Resistivity

Surface electrical resistivity, which reflects the resistance of concrete for chloride ion penetration, was measured at 28, 90, and 120 days to evaluate the durability of the quicklime-modified mixtures. Figure 4.6 presents the average resistivity values for C-Q 0%, C-Q 2%, and C-Q 4% specimens. At 28 days, the measured resistivity values were 18.5 kΩ·cm for C-Q 0%, 20.8 kΩ·cm for C-Q 2%, and 19 kΩ·cm for C-Q 4%, corresponding to “moderate” chloride penetration potential category according to

AASHTO T 358 classification. These results suggest that all concrete mixtures, regardless of quicklime content, demonstrate effective resistance to chloride ingress.

Furthermore, surface electrical resistivity consistently increased with age. At 90 and 120 days, resistivity values reached 25.3 and 32 kΩ•cm for C-Q 0%, 31.1 and 37 kΩ•cm for C-Q 2%, and 30.9 and 34.6 kΩ•cm for C-Q 4%, respectively. These values reflect a shift toward "low" chloride ion penetrability, suggesting a progressive refinement of the pore structure over time, contributing to decreased permeability and enhanced chloride ingress protection.

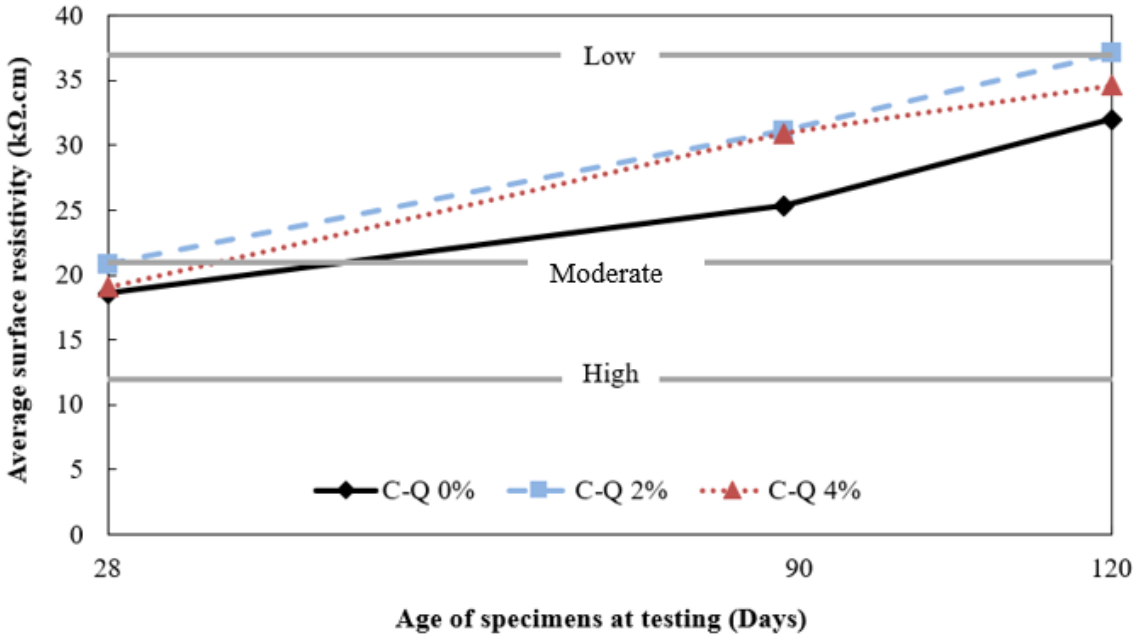

Figure 4.6. Average surface resistivity of quicklime-based self-healing concrete at 28, 90 and 120 days.

Additionally, the incorporation of quicklime aggregates improved surface resistivity at all curing ages. Specifically, a 2% quicklime replacement led to increases of approximately 12.4% at 28 days, 23% at 90 days, and 16% at 120 days, and a 4% replacement resulted in increases of 2.8%, 22%, and 8.2%, respectively, compared to the control mix (C-Q 0%). This enhancement is primarily attributed to the formation of additional calcium silicate hydrate (C–S–H) gel and the pore-filling effect of quicklime aggregates, which reduce porosity and hinder chloride ion ingress by refining and densifying the concrete microstructure.

4.3.3. Abrasion Resistance

The abrasion resistance of the concrete mixtures was evaluated by measuring the mass loss of specimens subjected to up to 500 revolutions in a Los Angeles abrasion machine. Figure 4.7 shows the condition of specimens from C–Q 0%, C–Q 2%, and C–Q 4% batches before and after 500 revolutions. It can be seen that abrasion begins with the fracturing of corners and edges and gradually rounds the specimens into more spherical shapes.

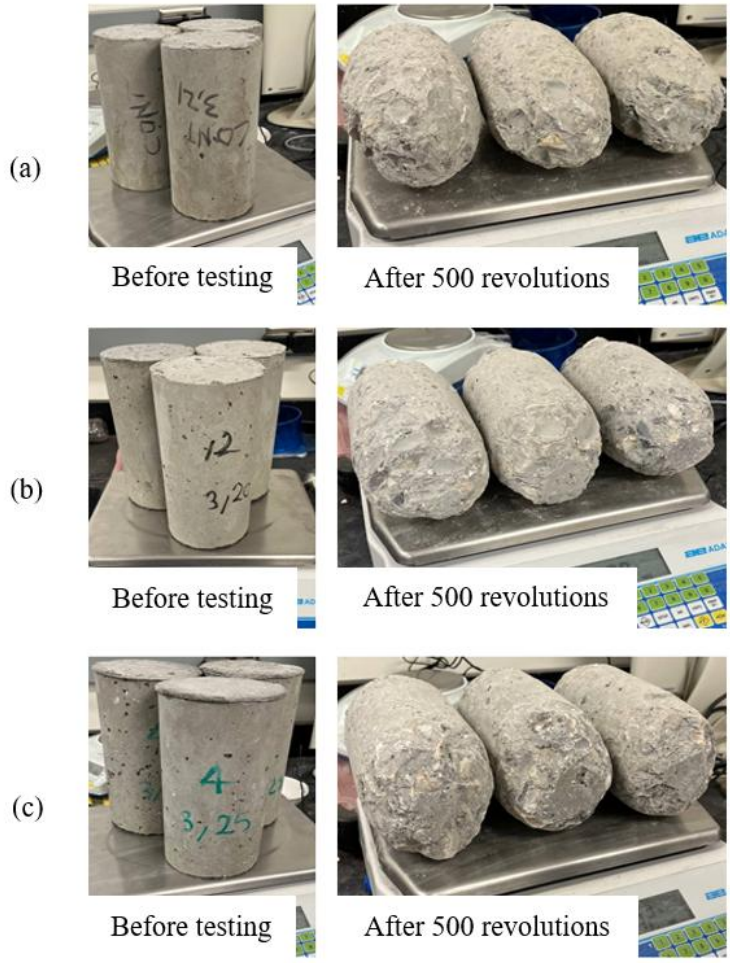

Figure 4.7. Condition of (a) C-Q 0%, (b) C-Q 2%, and (c) C-Q 4% specimens before and after 500 revolutions.

Figure 4.8 presents the calculated mass loss percentages at every 100-revolution interval for C-Q 0%, C-Q 2%, and C-Q 4% specimens. As expected, mass loss increases with the number of revolutions across all mixtures. After 500 revolutions, 28-day concrete with 100% natural aggregate (C-Q 0%) shows a mass loss of 28.7%, whereas specimens

containing 2% and 4% quicklime exhibit reduced mass losses of 20.7% and 14.6%, respectively. For the 90-day specimens, the corresponding mass losses are 21.5% (C-Q 0%), 15.2% (C-Q 2%), and 12.0% (C-Q 4%). These results demonstrate that abrasion resistance improves with increasing quicklime content and curing age. Compared to the control mixture, C-Q 4% specimens achieved reductions in mass loss of 14.1% and 9.5% at 28 and 90 days, respectively. Moreover, 90-day specimens exhibit lower mass losses than 28-day specimens, indicating enhanced abrasion resistance over time, due to increased strength and reduced porosity as curing progresses.

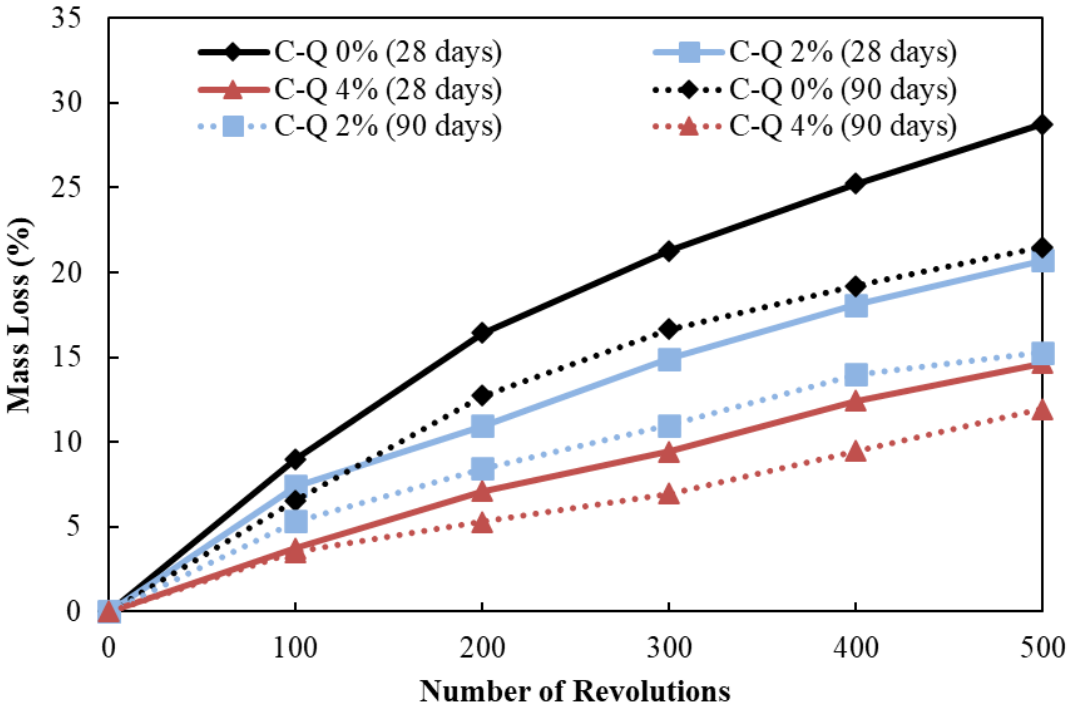

Figure 4.8. Mass loss percentages of all concrete mixtures after 500 revolutions in the Los Angeles abrasion machine at 28 and 90 days.

4.3.4. Freeze-Thaw Resistance

To evaluate the effects of freeze-thaw (FT) cycles on durability of the concrete specimens, mass loss and relative dynamic modulus of elasticity were measured at 30-cycle intervals up to 300 cycles. Figure 4.9 presents the progressive mass loss percentages of all specimens over 300 freeze-thaw cycles. The control C-Q 0% specimens experienced the highest mass loss at 8.8%, followed by C-Q 2% at 5.6%, and C-Q 4% at 4%. Among the

tested specimens, those without quicklime (C-Q 0%) exhibited the greatest degradation, as evidenced by their visibly deteriorated surface condition shown in Figure 4.10. In contrast, specimens containing 2% and 4% quicklime showed significantly lower mass loss after 300 cycles and retained more structural integrity. The reduced mass loss observed in specimens with 2% and 4% quicklime suggests improved resistance to freeze-thaw (FT) damage. This enhancement is likely due to the formation of additional calcium silicate hydrate (C-S-H) gel, which refines the pore structure and strengthens the matrix. Dong et al. [73], using poromechanical theory, explained that FT damage occurs when hydraulic pressure from freezing pore water exceeds the strength of concrete, regardless of the presence of entrained air. In quicklime-incorporated specimens, the denser and stronger matrix resist this pressure, thereby reducing the damage caused by freeze-thaw cycles.

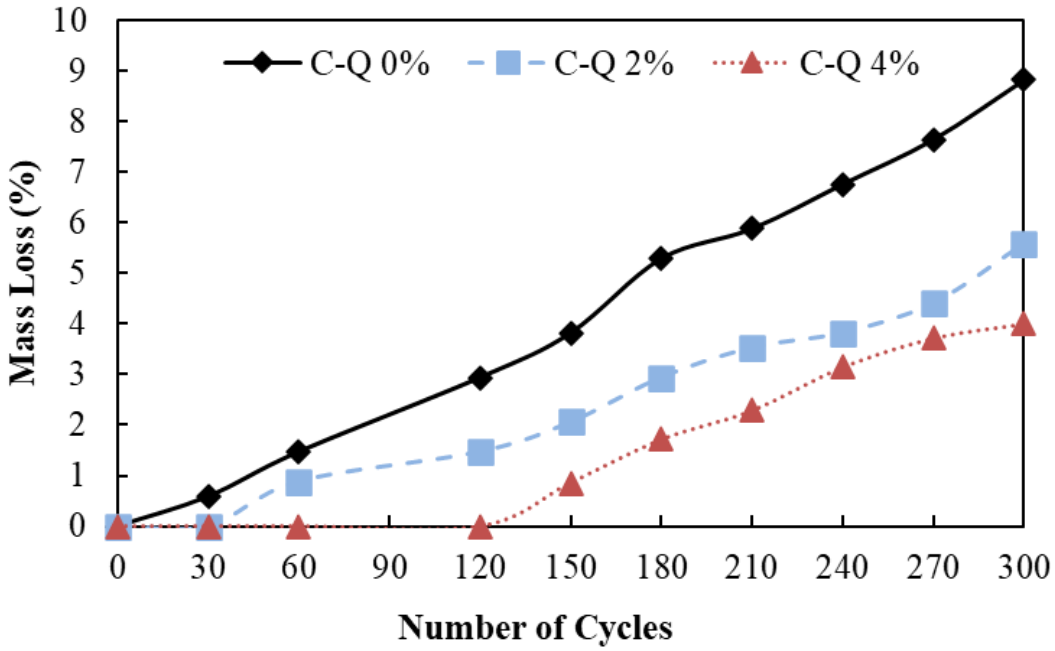

Figure 4.9. Mass loss of all mixtures over 300 freeze-thaw cycles.

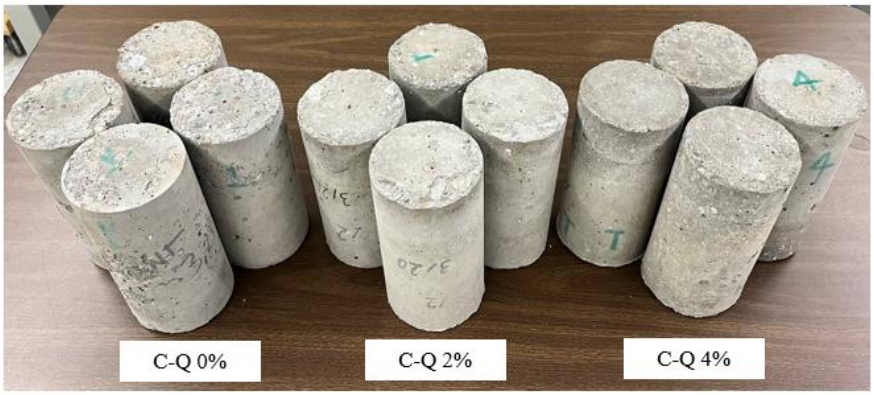

Figure 4.10. The surface conditions of all concrete mixtures after undergoing 300 freeze-thaw cycles.

Figure 4.11 presents the evolution of the relative dynamic modulus of elasticity throughout the freeze-thaw cycles, reflecting internal damage. After 300 cycles, specimens with 4% quicklime showed the smallest reduction in elastic modulus (23.8%), followed by the C-Q 2% mixture (35.3%), while the C-Q 0% mixture experienced the largest decrease (48%). This decline in dynamic modulus is consistent with microcrack formation caused by cyclic freeze-thaw stresses, as reported by Ebrahimi et al. [74] and Zhou et al. [75]. The superior retention of modulus in the quicklime mixtures suggests reduced internal damage and improved long-term durability.

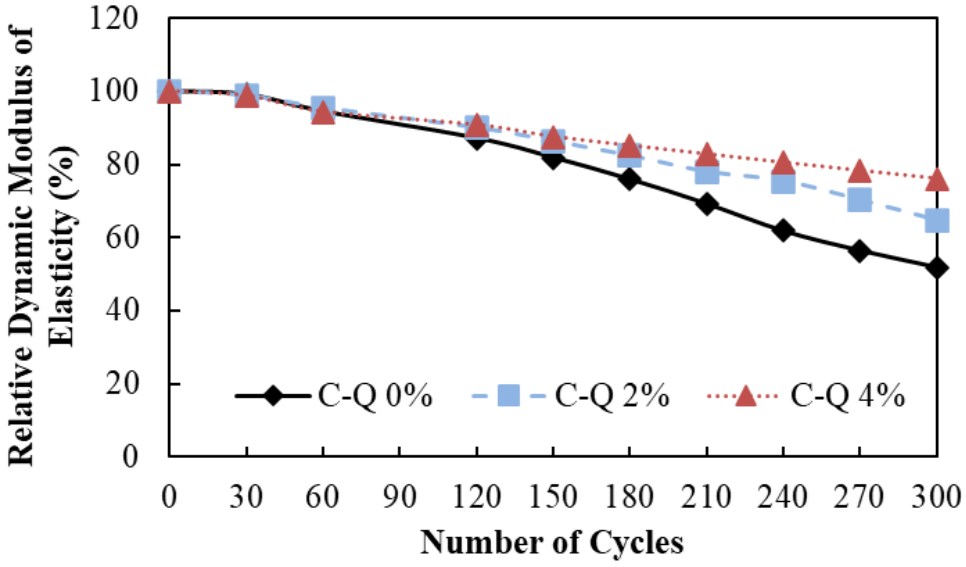

Figure 4.11. Relative dynamic modulus of elasticity (%) of all mixtures after 300 freeze-thaw cycles.

4.4. Crack Healing Capability

4.4.1. Surface-Level Crack Healing

To evaluate surface-level healing performance, changes in surface-crack width were monitored in both micro and macrocracked specimens containing 0%, 2%, and 4% quicklime after 180-days period. Among the microcracked specimens (W-MICRO1-Q series) with initial widths ranging from 100 to 200 μm and exposed to cyclic water/air-drying, specimens with 4% quicklime (W-MICRO1-Q 4%) reached 100% surface crack closure, while W-MICRO1-Q 2% and W-MICRO1-Q 0% achieved 93% and 34% closure, respectively as summarized in Table 4.1. These values were derived from crack width measurements obtained through optical microscopy and quantified using ImageJ.

Table 4.1. Crack closure (%) of all batches after 180 days of monitoring

Group ID	Crack Closure (%)	Healing Type	Group ID.	Crack Closure (%)	Healing Type
W-MICRO1-Q 0%	34	Partial	DS-MICRO1-Q 0%	87	Partial
W-MICRO1-Q 2%	93	Partial	DS-MICRO1-Q 2%	100	Fully
W-MICRO1-Q 4%	100	Fully	DS-MICRO1-Q 4%	100	Fully
W-MICRO2-Q 0%	17	Partial	DS-MICRO2-Q 0%	40	Partial
W-MICRO2-Q 2%	47	Partial	DS-MICRO2-Q 2%	73	Partial
W-MICRO2-Q 4%	56	Partial	DS-MICRO2-Q 4%	81	Partial
W-MACRO-Q 0%	7	Partial	DS-MACRO-Q 0%	33	Partial
W-MACRO-Q 2%	20	Partial	DS-MACRO-Q 2%	69	Partial
W-MACRO-Q 4%	24	Partial	DS-MACRO-Q 4%	66	Partial

Specifically, average crack widths were reduced from 154 μm to 104 μm in W-MICRO1-Q 0%, from 158 μm to 11 μm in W-MICRO1-Q 2%, and from 171 μm to 0 μm in W-MICRO1-Q 4%, as shown in Figure 4.12. Additionally, the surface-crack widths for W-MICRO2-Q (0-4%), which included specimens with wider initial crack widths (200–

300 µm), are presented in Figure 4.13. The average crack width in specimens with 0% quicklime (W-MICRO2-Q 0%) was reduced by 17%, while enhanced reductions of 47% and 56% were observed in C-Q 2% and C-Q 4%, respectively. Figure 4.14 presents optical microscopy images of macrocracked specimens (W-MACRO-Q) with initial crack widths of 300–550 µm after cyclic water/air-drying for 180 days. The average crack width in W-MACRO-Q 0% decreased by 7%, from 500 µm to 465 µm. In contrast, quicklime mixtures exhibited greater reductions with W-MACRO-Q 2% showing a 20% reduction, from 472 µm to 377 µm, while W-MACRO-Q 4% had the greatest reduction at 24%, from 509 µm to 386 µm.

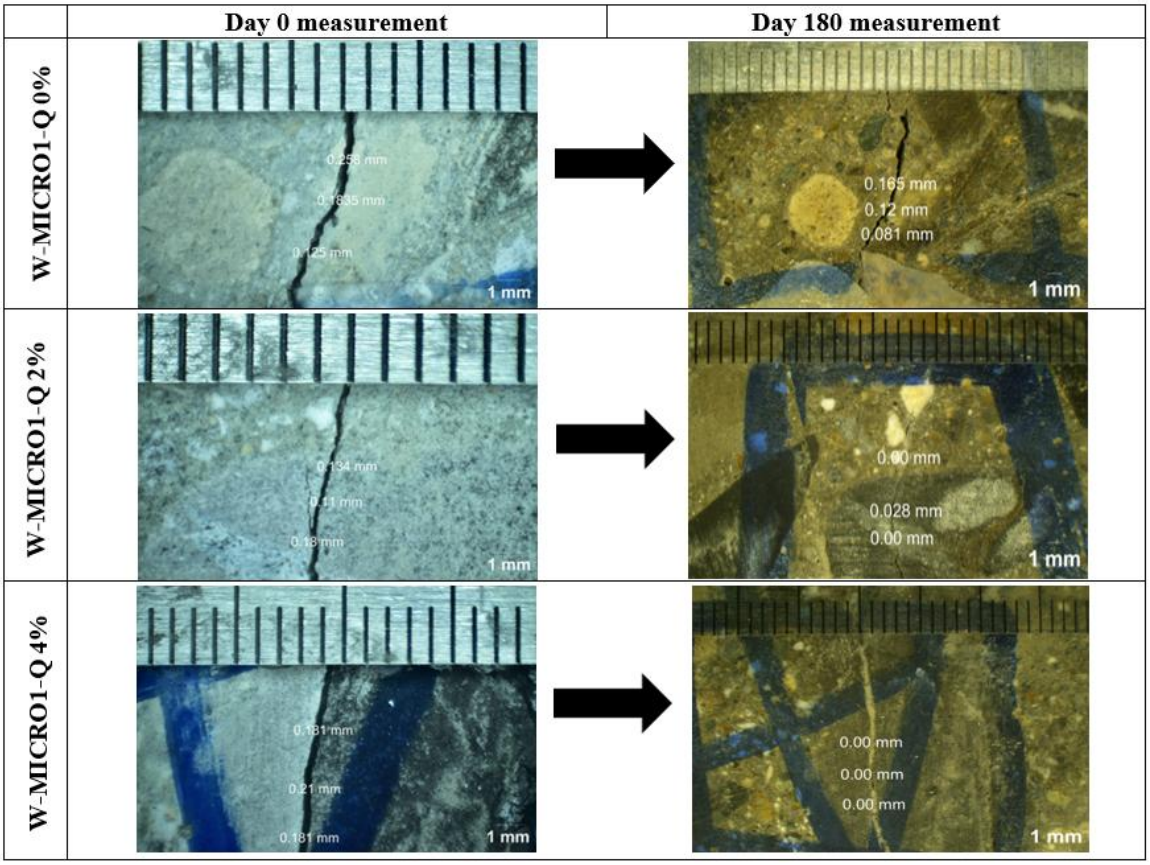

Figure 4.12. Crack width changes in W-MICRO1-Q (0–4%) specimens with initial crack widths of 100–200 µm after 180 days of cyclic water/air-dry exposure.

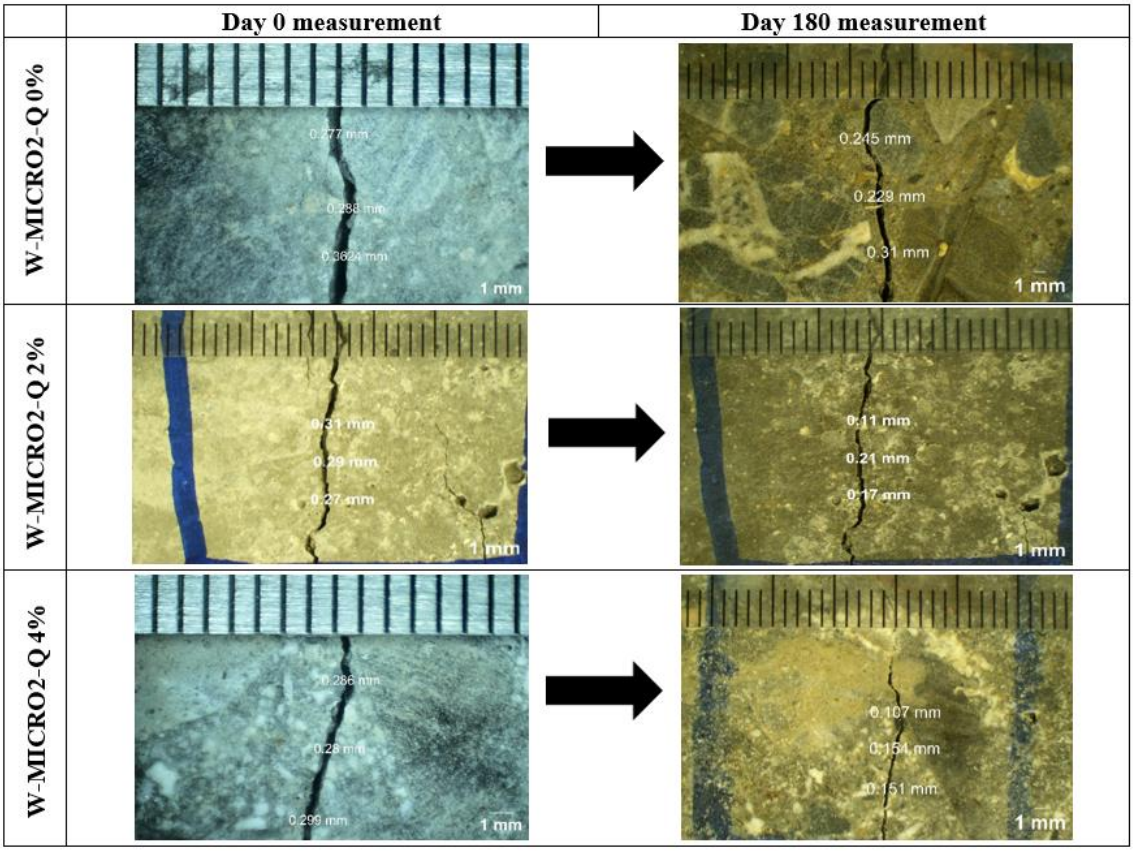

Figure 4.13. Crack width changes in W-MICRO2-Q (0–4%) specimens with initial crack widths of 200–300 µm after 180 days of cyclic water/air-dry exposure.

The results from both micro and macrocracked specimens indicate that higher quicklime content significantly enhances surface-level crack healing. This improvement is primarily attributed to the presence of calcium oxide (CaO) in quicklime, which reacts with atmospheric carbon dioxide (CO_2) and water (H_2O) to form calcium carbonate ($CaCO_3$). The precipitation of $CaCO_3$ within the cracks effectively contributes to their closure. Accordingly, specimens with 2% and 4% quicklime exhibited greater healing performance due to increased CaO availability and subsequent $CaCO_3$ formation. In addition to quicklime content, the initial crack width was found to have a substantial influence on healing effectiveness. Specimens with microcracks showed greater reductions in crack width compared to those with macrocracks. For instance, microcracked specimens with width ranging from 100 to 200 µm and containing 0%, 2%, and 4% quicklime achieved 17%, 46%, and 44% higher crack width reductions, respectively, than those with crack width of 200 to 300 µm. Compared to macrocracked specimens with the same quicklime

contents, these microcracked specimens showed 27%, 73%, and 76% higher crack width reduction, respectively. Microcracks require less healing product to achieve full closure, making them more responsive to the limited supply of healing agents available from quicklime or hydration products. Further, in microcracks, the crack faces are closer, increasing the likelihood that precipitated products (C–S–H or $CaCO_3$) can bridge and bond across the crack, restoring integrity more effectively.

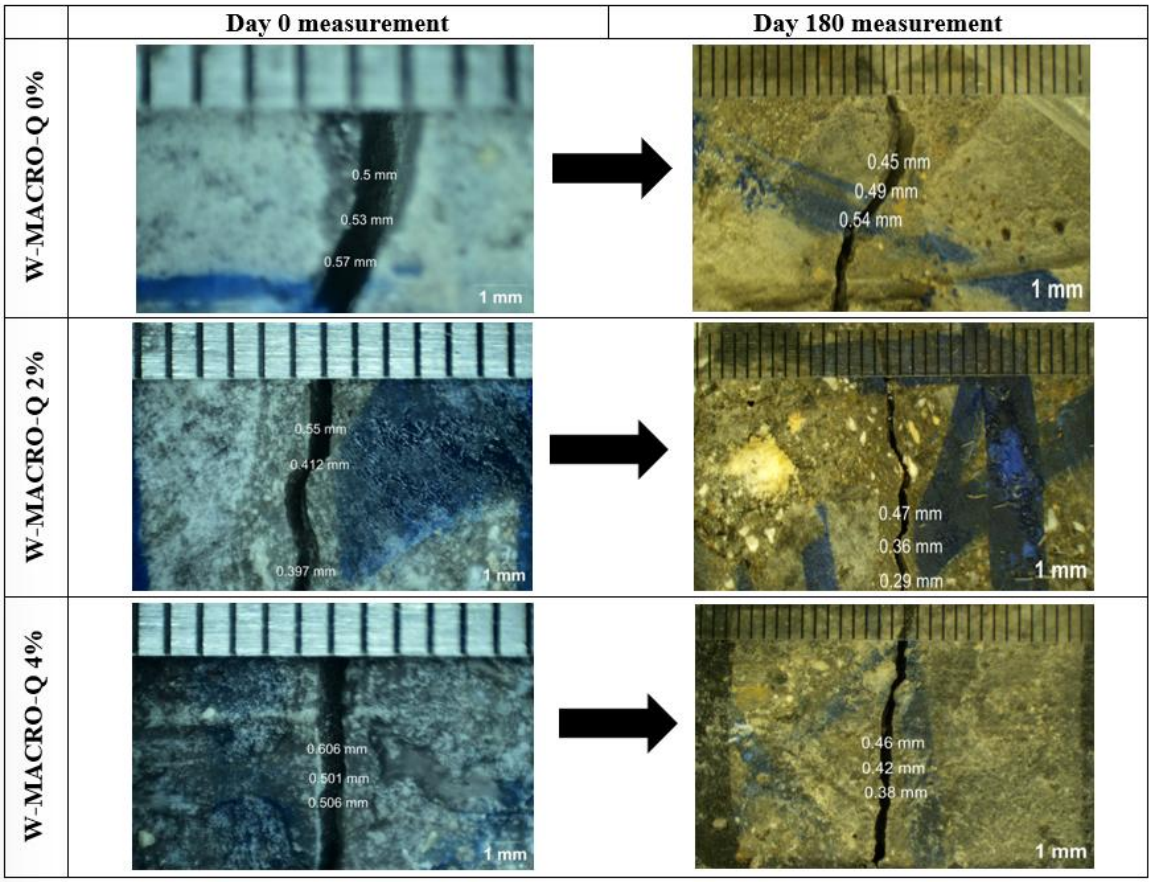

Figure 4.14. Crack width changes in W-MACRO-Q (0–4%) specimens with initial crack widths of 300–550 µm after 180 days of cyclic water/air-dry exposure.

In addition to water/air-drying exposure, surface-crack healing was also evaluated in specimens subjected to cyclic deicing salt solution and air-drying conditions. Figure 4.15 presents the measured crack widths in microcracked specimens in the DS-MICRO1-Q group (initial crack widths: 100–200 µm) containing 0%, 2%, and 4% quicklime after 180 days of exposure. The average crack width in DS-MICRO1-Q 0% decreased from 155 µm to 20 µm, corresponding to an 87% surface-crack closure. In contrast, specimens with 2% and 4% quicklime achieved full crack closure, with widths reducing from 138 µm and

147 µm to 0 µm, respectively. Crack width changes in DS-MICRO2-Q microcracked specimens with initial widths ranging from 200 to 300 µm after 180 days of exposure to the deicing salt/air-drying cycle, are shown in Figure 4.16. Specimens with 0%, 2%, and 4% quicklime exhibited 40%, 73%, and 81% surface-crack closure, respectively, as summarized in Table 4.1. These results confirm that higher quicklime content enhances healing in microcracks, even under chemically aggressive conditions, although healing efficiency decreases with increasing initial crack width.

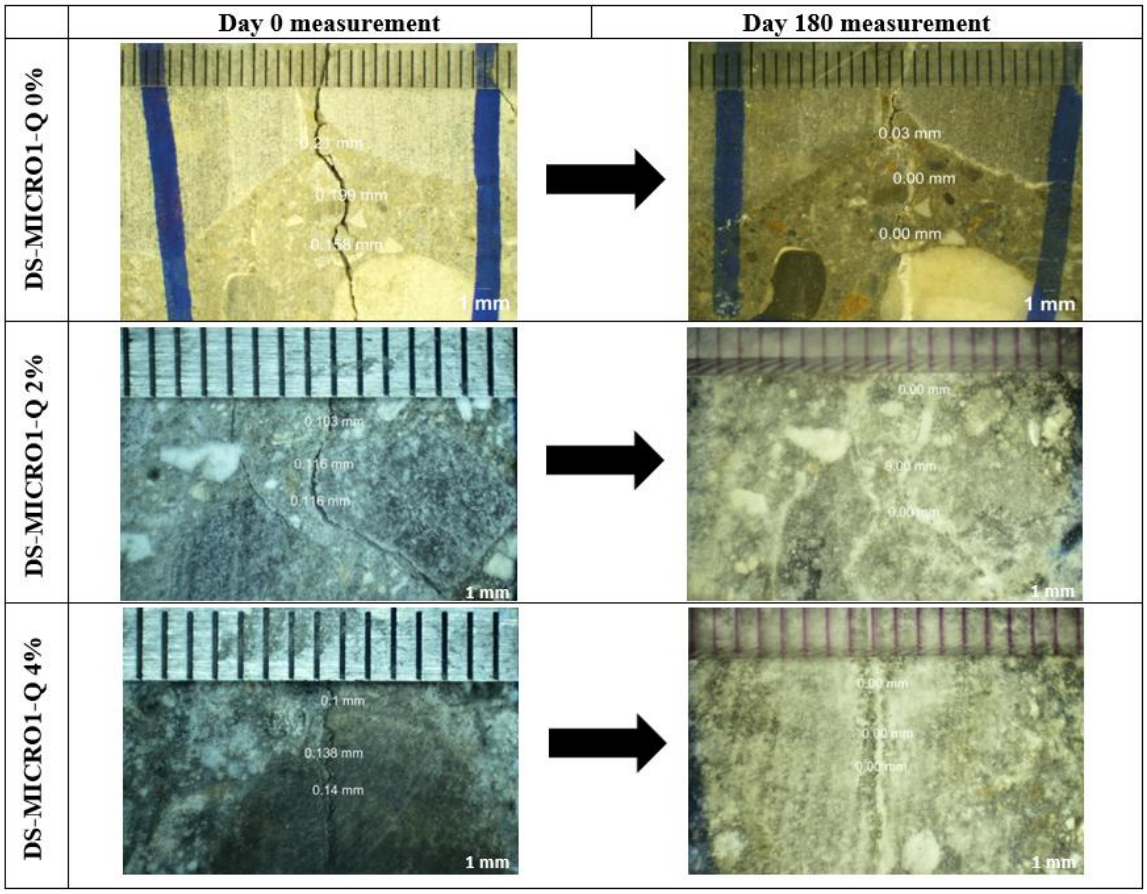

Figure 4.15. Crack width changes in DS-MICRO1-Q (0–4%) specimens with initial crack widths of 100–200 µm after 180 days of cyclic deicing salt solution/air-dry exposure.

For macrocracked specimens under the same exposure conditions (DS-MACRO-Q), Figure 4.17 shows a similar trend. DS-MACRO-Q 0% exhibited a 33% reduction in crack width, decreasing from 517 µm to 348 µm. In contrast, specimens with 2% and 4% quicklime showed significantly greater healing, with crack widths decreasing from 457 µm

to 143 µm (69% closure) and from 485 µm to 166 µm (66% closure), respectively. These results are consistent with the trends observed under water/air-dry exposure and further confirm that increasing quicklime content leads to greater surface-crack closure, while larger initial cracks – especially macrocracks – result in lower healing efficiency.

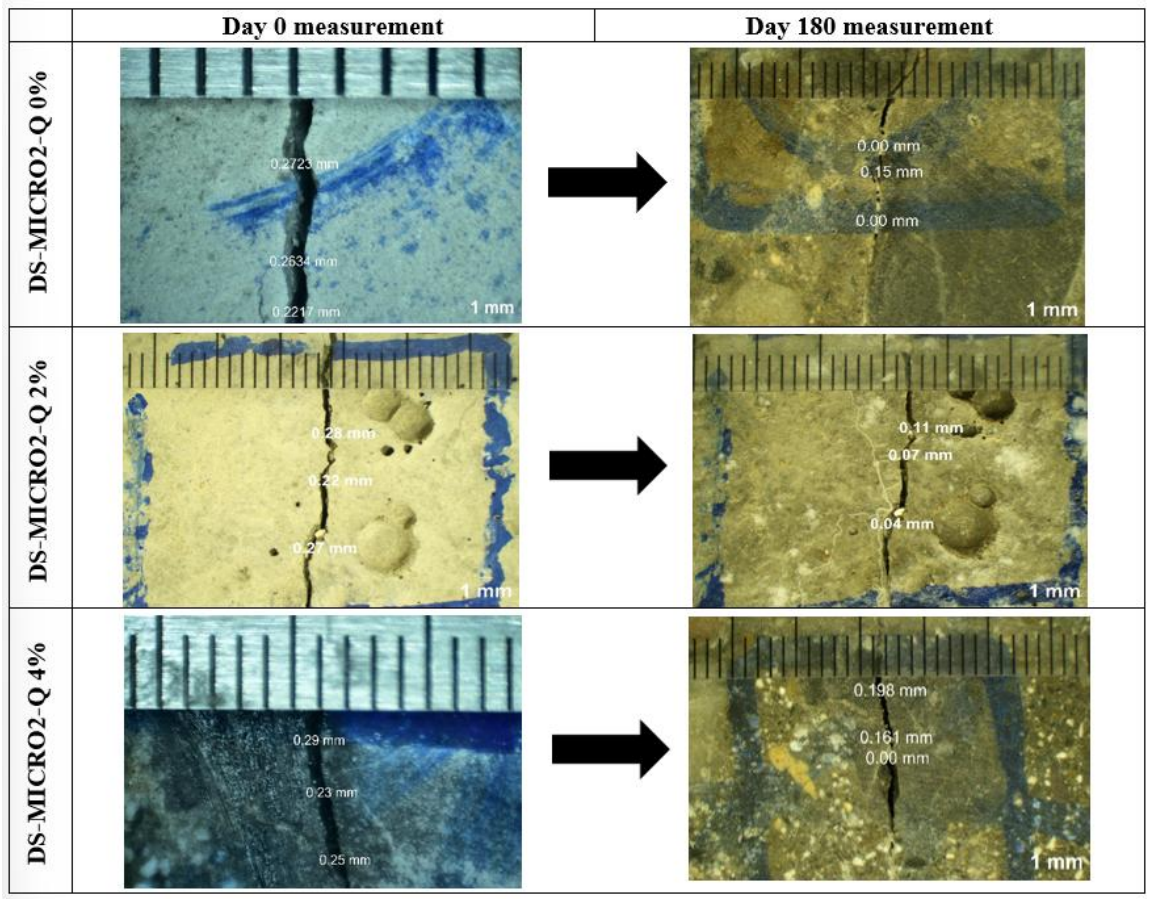

Figure 4.16. Crack width changes in DS-MICRO2-Q (0–4%) specimens with initial crack widths of 200–300 µm after 180 days of cyclic deicing salt solution/air-dry exposure.

To assess the healing progression over time, the percentage of surface-crack closure was calculated at days 0, 60, 120, 160, and 180 for all mixtures. These results are presented in Figure 4.18, where part (a) illustrates the healing progression of micro and macrocracked specimens exposed to cyclic water/air-drying, and part (b) shows the corresponding results for specimens subjected to cyclic deicing salt solution and air-drying. A steady increase in healing percentage is observed across all mixtures under both the exposure conditions, highlighting the positive influence of extended healing period. Notably, preliminary crack width measurements using a crack width microscope showed that the first significant signs

of healing appeared close to day 60, identifying it as the onset of visible surface-level crack closure.

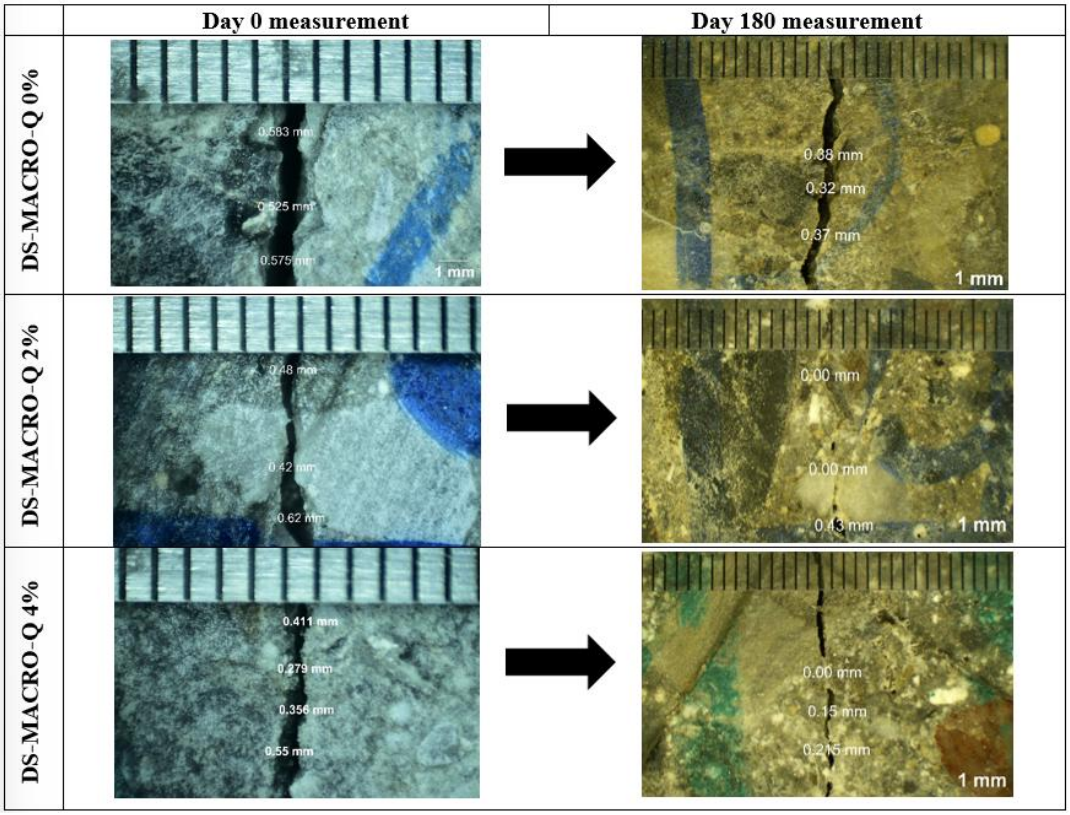

Figure 4.17. Crack width changes in DS-MACRO-Q (0–4%) specimens with initial crack widths of 300–550 µm after 180 days of cyclic deicing salt solution/air-dry exposure.

For specimens exposed to cyclic water/air-drying (Figure 4.18(a)), W-MICRO1-Q mixtures achieved 58–79% of their total surface healing within the first 60 days, with W-MICRO1-Q 0% showing the lowest and W-MICRO1-Q 4% the highest early-stage healing. Similarly, W-MICRO2-Q specimens reached 47–75% of their final closure by day 60. In contrast, W-MACRO-Q specimens exhibited considerably slower healing rates, with only 7–20% of their total healing in the same period. Most healing in W-MACRO-Q occurred between days 60 and 120, contributing 54–84% of the total crack closure, suggesting that larger initial cracks tend to heal more gradually over time. Larger cracks heal more gradually because they have a greater void volume that requires more time for healing agents (like Ca^{2+} ions and carbonate) to be transported, precipitated, and accumulated. Figure 4.18(b) illustrates the healing progression trends for specimens

subjected to cyclic exposure to deicing salt solution and air drying. Microcracked specimens from DS-MICRO1-Q and DS-MICRO2-Q series achieved 78–95% and 60–68% of their final healing, respectively, by day 60. In comparison, macrocracked specimens (DS-MACRO-Q) reached 66–72% of their total healing within the same period. These findings indicate that the rate of early-stage healing is influenced by both crack size and exposure conditions, with smaller cracks and aggressive chemical environments promoting more rapid healing. Overall, across all specimens, surface-crack closure improved with increasing quicklime content and decreasing initial crack width. This effect was particularly evident in microcracked specimens with higher quicklime content, which achieved up to 100% healing, whereas macrocracked specimens exhibited a maximum of 69% closure. Additionally, for the same crack width and quicklime content, specimens exposed to deicing solution and air-drying demonstrated greater surface-crack closure than those subjected to water/air-drying. However, this surface-crack closure alone may not fully represent the extent of internal healing. Therefore, evaluating crack closure through the entire depth of the specimen is essential to fully assess the effect of exposure conditions on the overall healing progression.

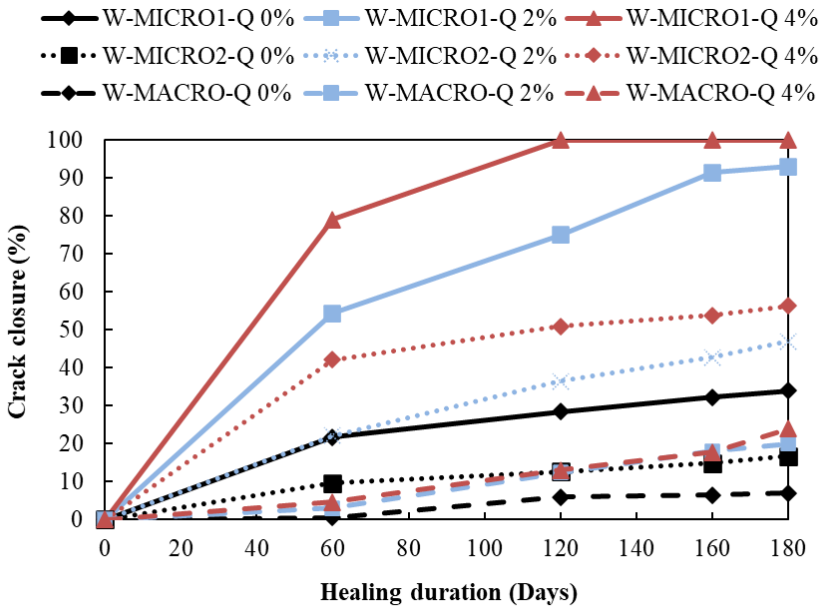

(a) Specimens exposed to water/air-drying cycles

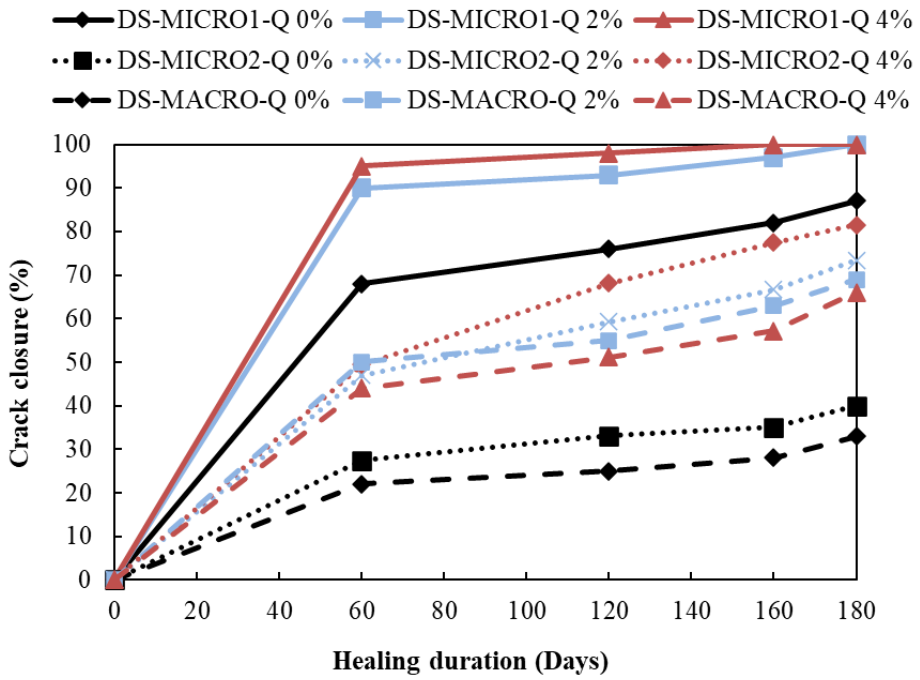

(b) Specimens exposed to deicing salt solution/air-drying cycles

Figure 4.18. Healing percentage trends over 180 days for both micro and macrocracked specimens exposed to (a) water/air-dry and (b) deicing salt solution/air-dry cycles.

4.4.2. Internal Depth-Wise Crack Healing

The extent of crack healing throughout the depth of concrete specimens was evaluated using ultrasonic pulse velocity (UPV) measurements and a falling head water flow test. Figure 4.19 presents the relative improvement in UPV (%) recorded on day 0 (before healing) and after 60, 120, 160, and 180 days of healing for all specimens. Higher UPV values typically indicate denser concrete, reflecting a higher modulus of elasticity, improved mechanical integrity, and fewer internal voids or cracks [76]. As shown in Figure 4.19 (a), W-MICRO1-Q 0% specimens exhibited a 7% increase in pulse velocity, rising from 3.2 km/s to 3.4 km/s after 180 days of exposure. Specimens containing 2% and 4% quicklime showed greater increases of 13.5% (from 3.2 km/s to 3.6 km/s) and 13.8% (from 3.4 km/s to 3.9 km/s), respectively. Similarly, for W-MICRO2-Q 0% specimens, the UPV increased by 5.3% (from 3.2 km/s to 3.37 km/s), while those with 2% and 4% quicklime showed higher increases of 8% and 12%, respectively. In W-MACRO-Q specimens, the velocity increase was more modest, with increase in control specimen (0% quicklime) by

5% (from 2.8 km/s to 2.9 km/s), and specimens containing 2% and 4% quicklime showing marginal improvement of approximately 6%.

Figure 4.19 (b) displays the relative UPV increment (%) for micro and macrocracked specimens exposed to 180 days of cyclic deicing salt solution and air-drying. Among the DS-MICRO1-Q specimens, those with 0% quicklime exhibited a 5.5% increase in UPV, while specimens with 2% and 4% quicklime showed 12% increases. In DS-MICRO2-Q specimens, the 0% quicklime mixture showed a 5% increase, while the 2% and 4% mixtures increased by approximately 10% and 11%, respectively. The DS-MACRO-Q 0% specimens experienced a 5.5% increase (from 2.89 km/s to 3.05 km/s), while specimens with 2% and 4% quicklime exhibited increases of 7% (from 2.99 km/s to 3.25 km/s) and 8% (from 2.98 km/s to 3.22 km/s), respectively.

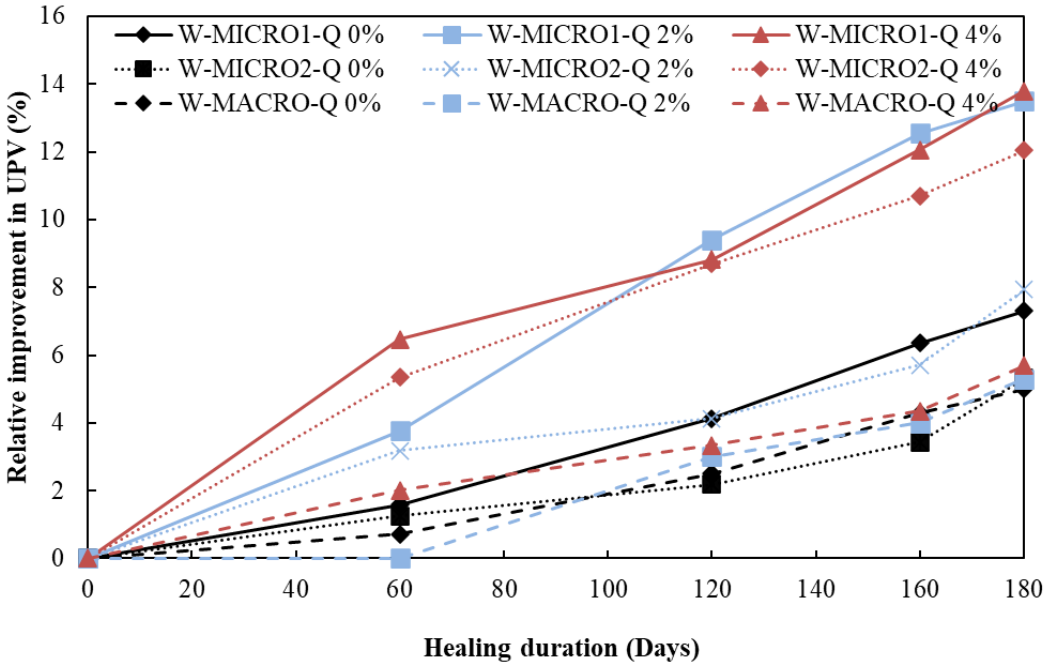

(a) Specimens exposed to water/air-drying cycles

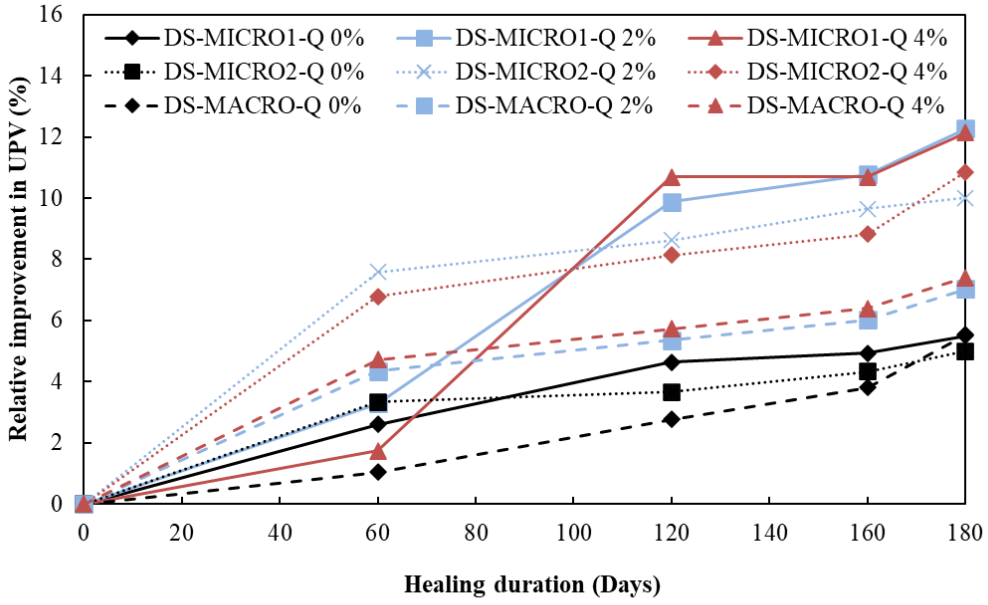

(b) Specimens exposed to deicing salt solution/air-drying cycles

Figure 4.19. Ultrasonic pulse velocity measurements over 180 days for both micro and macrocracked specimens exposed to (a) water/air-dry and (b) deicing salt solution/air-dry cycles.

These UPV results confirm that the incorporation of quicklime significantly enhances the healing progression throughout the depth of concrete specimens, with the highest UPV increase (13.8%) observed in W-MICRO1-Q 4% specimen. Specimens without quicklime exhibited comparatively lower healing efficiency, with a maximum UPV increase of 7%, recorded in W-MICRO1-Q 0%. For a given quicklime content and exposure condition, specimens with microcracks healed more effectively than those with macrocracks in terms of depth-wise healing. Furthermore, water/air-drying exposure promoted slightly better healing than deicing salt/air-drying through the depth of microcracked specimens (13.8% in W-MICRO1-Q 4% vs. 12% in DS-MICRO1-Q 4%). This is possibly because the consistent presence of moisture supports prolonged hydration of unreacted cement particles and facilitates Ca^{2+} and CO_3^{2-} ion mobility, promoting uniform $CaCO_3$ and C–S–H formation along the crack depth. The small crack width allows efficient moisture retention and healing agent transport. However, in macrocracked specimens, the opposite trend was observed, with the deicing salt solution slightly outperforming water exposure, as DS-MACRO-Q specimens exhibited a 0.5–1% higher

increase in UPV compared to their water-exposed counterparts. This is due to NaCl acting as a nucleation catalyst that accelerates $CaCO_3$ precipitation at deeper crack locations, with larger crack volumes allowing easier salt ingress and more effective ion exchange and carbonation reactions.

To further verify healing through the full depth of the concrete specimens with 100% surface-crack closure, a falling head water flow test was conducted on W-MICRO-Q 4%, DS-MICRO-Q 2%, and DS-MICRO-Q 4% specimens. Results indicated that during the 24-hour test period, no water passed through the specimens, and a permeability coefficient of 0 mm/s was recorded for all. These findings support the surface-level crack measurement and the UPV results for the specimens with complete crack closure, confirming substantial sealing of internal cracks. While healing is expected to progress further over time, extending the measurement duration beyond 24 hours may result in slight water passage and a permeability coefficient greater than 0 mm/s, which could be explored in future studies.

4.4.3. Characterization of Healing Products

The compositional properties of the crack-filling materials were characterized through SEM-EDS for concrete specimens containing 0%, 2%, and 4% quicklime. Both EDS elemental mapping and point-and-ID analyses were conducted under varying exposure conditions to investigate the healing products and matrix microstructure. Figure 4.20 (a-c) presents elemental maps obtained by EDS for microcracked specimens W-MICRO1-Q with initial crack widths of 100–200 μm exposed to water/air-dry cycles, while Figure 4.21 (a-c) shows elemental maps for macrocracked DS-MACRO-Q specimens subjected to cyclic deicing salt solution and air-dry conditions. EDS mapping was used to provide an overview of elemental distribution across the healing regions, with color-coded images reflecting the relative concentrations of key elements based on color intensity. These color-coded maps provide a qualitative assessment of elemental concentration gradients, highlighting the spatial distribution of key elements such as calcium (Ca), silicon (Si), and aluminum (Al), which are commonly associated with healing products.

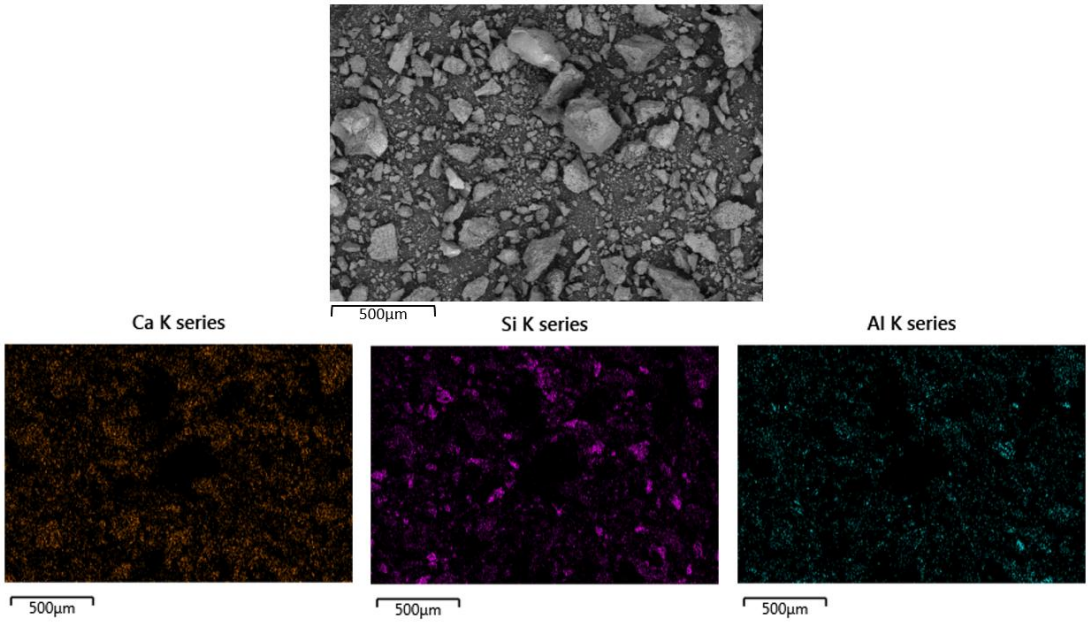
500µm
Ca K series
Si K series
Al K series
500µm
500µm
500µm

(a)

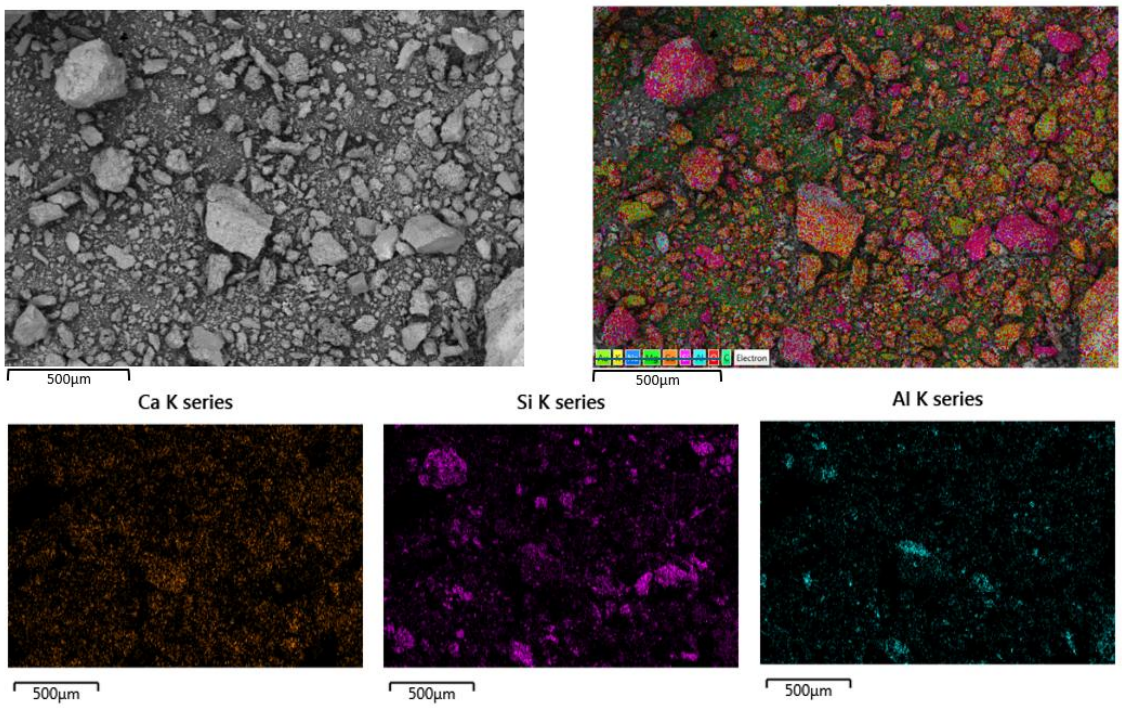
500µm
500µm
Ca K series
Si K series
Al K series
500µm
500µm
500µm

(b)

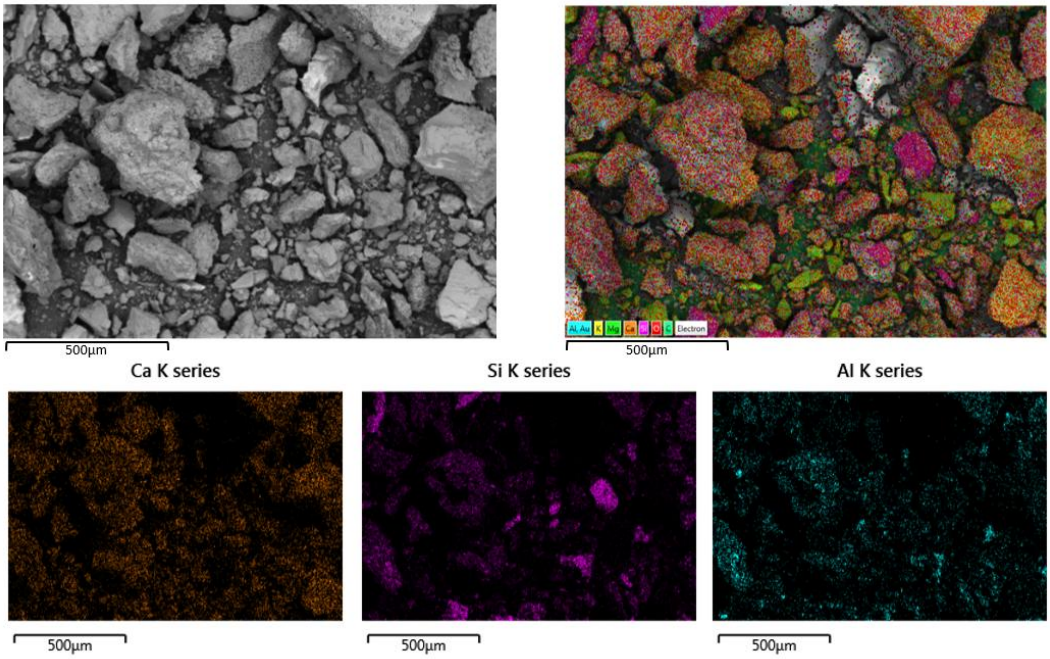

(c)

Figure 4.20. Elemental distribution mapping of healing materials: (a) W-MICRO1-Q 0%, (b) W-MICRO1-Q 2%, (c) W-MICRO1-Q 4%.

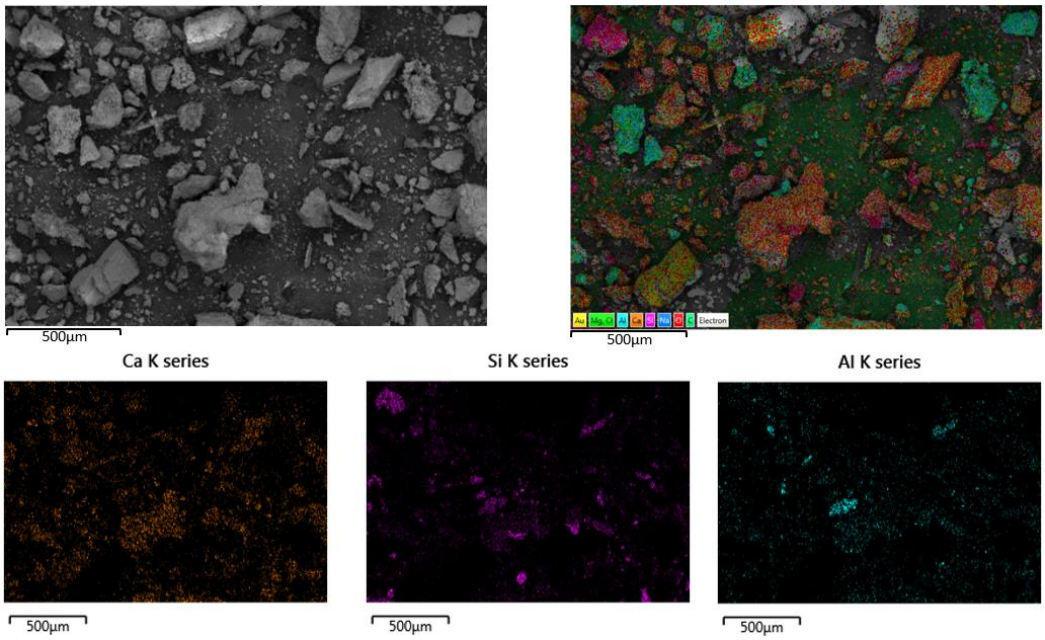

(a)

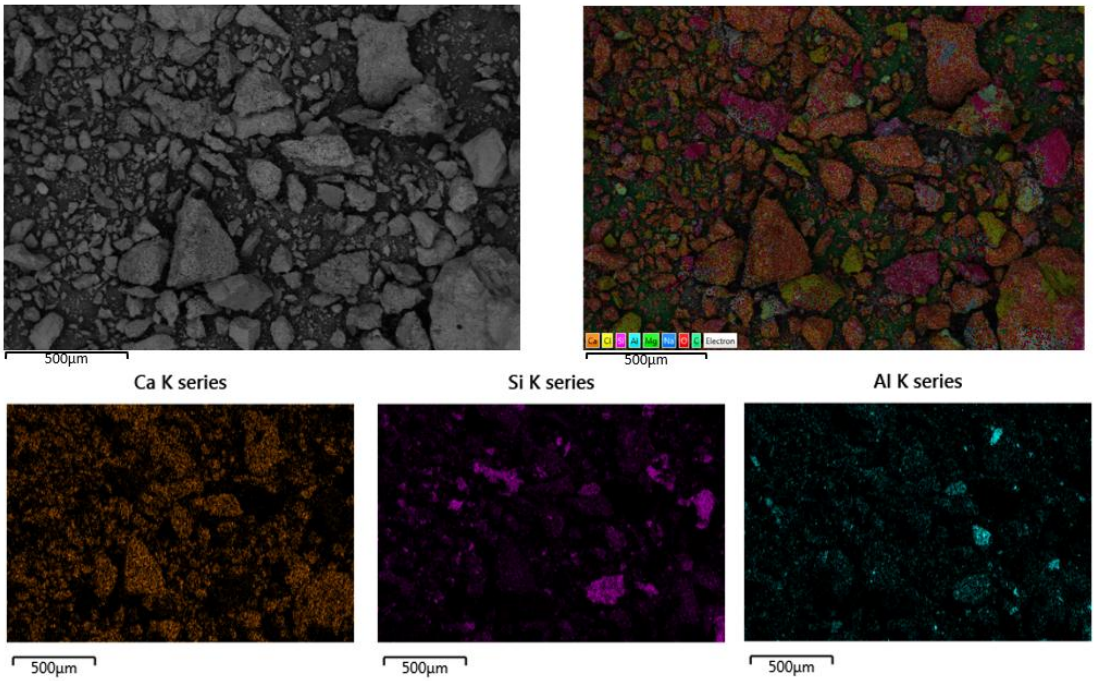

(b)

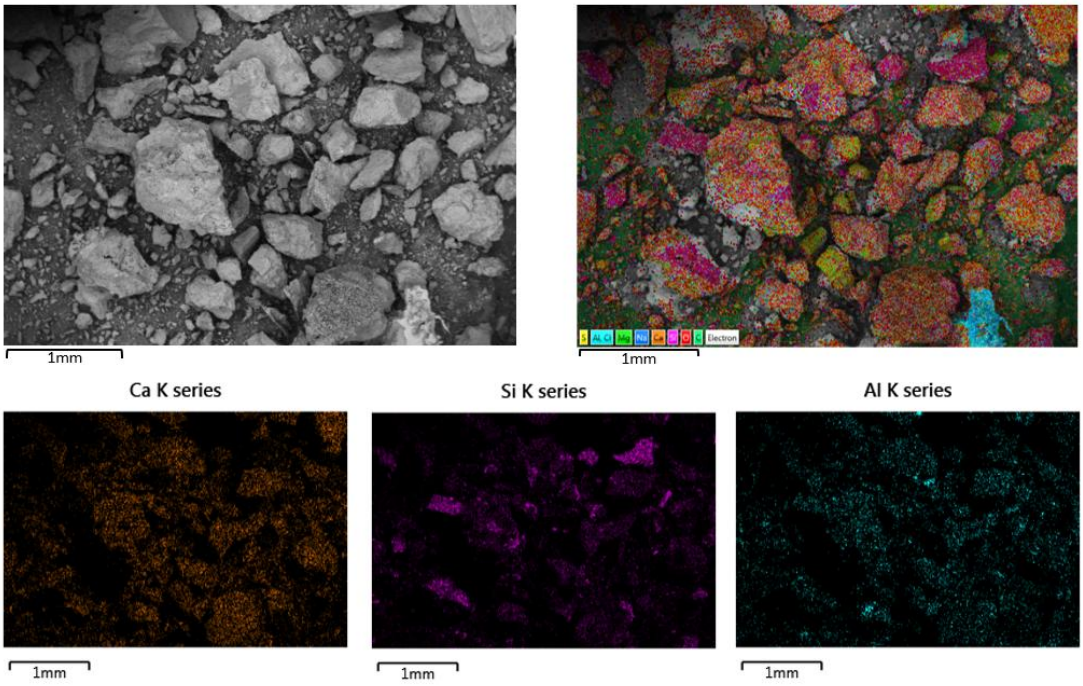

(c)

Figure 4.21. Elemental distribution mapping of healing materials: (a) DS-MACRO-Q 0%, (b) DS-MACRO-Q 2%, (c) DS-MACRO-Q 4%.

In addition to elemental mapping, point-and-ID analysis was performed at approximately 20 locations per specimen to obtain quantitative atomic percentage data. This step was particularly important because the specimens were mounted on carbon tape, which interfered with the accurate measurement of carbon content in the atomic percentage results. Table 4.2 presents the average atomic percentages of each element. Based on these values, the healing products primarily consist of calcium carbonate ($CaCO_3$) and calcium silicate hydrate (C–S–H). However, it is difficult to determine which of these materials is the dominant healing product in each mixture. As reported in the literature, Ca/Si ratios serve as reliable indicators for identifying the predominant compound in each mixture [77].

A Ca-to-Si ratio between 1.5 and 2 indicates the formation of calcium silicate hydrate (C–S–H), while a ratio higher than 2 suggests that calcium carbonate ($CaCO_3$) is the primary healing product [78]. Accordingly, microcracked specimens with 0% quicklime exhibit a Ca-to-Si ratio of 1.5, indicating that C–S–H is the dominant healing product, with some $CaCO_3$ also present. In specimens with 2% quicklime, Ca/Si ratio is 1.7 and both C–S–H and $CaCO_3$ were identified as the primary healing products. In contrast, $CaCO_3$ was found to be the dominant healing product in microcracked specimens with 4% quicklime, which exhibited a Ca-to-Si ratio of 2.6. It has been reported that $CaCO_3$ tends to form at the crack mouth, whereas C–S–H can form both at the surface and within the depth of cracks [79]. This helps explain why specimens with 2% and 4% quicklime, which had a higher content of $CaCO_3$, exhibited greater surface crack closure compared to those without quicklime. Moreover, the Al/Si ratio was used to compare the chemical composition of the matrix and the healing products. Previous studies have reported that the Al/Si ratio required to form healing materials typically falls within the range of 0.1 to 0.3 [80, 81], which is consistent with the results obtained in the present study.

Similar trends in Ca-to-Si ratios were observed for macrocracked specimens exposed to deicing salt. However, NaCl-related phenomena were also evident. In specimens without quicklime (0%), the Na-to-Cl ratio at most measured points was approximately 1.1, which closely aligns with the stoichiometric composition of NaCl (1:1). This suggests the crystallization of pure NaCl within the crack voids, serving as a passive filling material. However, specimens containing 2% and 4% quicklime exhibited Na-to-Cl ratios of 1.4 and 0.8, respectively, indicating deviations from the expected stoichiometry.

These variations suggest that in the presence of quicklime, NaCl does not crystallize independently but instead serves as a nucleation catalyst, promoting $CaCO_3$ formation and enhancing crack healing. A similar observation was reported by Takita et al. [82], who found that adding NaCl to a $CaCO_3$ system formed from $CaCl_2$ and Na_2CO_3 solutions promoted the transformation of vaterite to calcite and favored crystal growth over nucleation, resulting in larger and more complex calcite structures. These findings suggest that NaCl increases $CaCO_3$ solubility and drives calcite deposition. This mechanism aligns with its catalytic role in the 2% and 4% quicklime specimens, where it supports $CaCO_3$ formation as the primary healing product.

Table 4.2. Average atomic percentages of elements of healing materials based on point-and-ID EDS analysis

Group ID	O	C	Ca	Si	Al	Mg	S	Na	Cl	Ca/Si	Na/Cl	Al/Si
W-MICRO1-Q 0%	61.5	17.2	10.8	7	1.6	1.3	0.6	-	-	1.5	-	0.2
W-MICRO1-Q 2%	60.4	20	11	6.3	1.2	1.1	0.7	-	-	1.7	-	0.3
W-MICRO1-Q 4%	60.2	19.2	12.7	5	1.2	1.9	0.8	-	-	2.6	-	0.2
DS-MACRO-Q 0%	46.5	22.1	9.6	6.7	0.8	0.6	0.9	10.1	9.1	1.4	1.1	0.2
DS-MACRO-Q 2%	59.4	21.4	9	5	1	3	0.5	1.2	0.9	1.8	1.4	0.2
DS-MACRO-Q 4%	54.4	17.1	12.7	5	1.4	1.5	0.7	4.4	4.9	2.5	0.8	0.1

To summarize, microcracks consistently exhibited superior healing compared to macrocracks, with healing effectiveness declining as crack width increased. Under the same conditions, quicklime mixtures outperformed the control, with similar healing observed for 2% and 4% quicklime. Deicing salt exposure led to significantly greater surface crack closure across all mixtures, largely due to NaCl crystallization at the surface. However, internal healing showed only marginal differences: water slightly favored

microcrack healing (13.8% vs. 12% UPV increase), while deicing salt slightly improved macrocrack healing (0.5–1% higher UPV). Water exposure promoted slightly better internal healing in microcracks due to sustained moisture supporting C–S–H and $CaCO_3$ formation, whereas macrocracks benefited more from deicing salt, as NaCl acted as a nucleation catalyst for $CaCO_3$ precipitation. SEM-EDS results confirmed a shift from C–S–H in control specimens to $CaCO_3$ as the dominant healing product in quicklime mixtures.

Figure 4.22 presents the SEM results capturing the behavior of quicklime aggregates in the concrete environment. The full image (a) and magnified view (b) reveal a distinct bright rim surrounding the quicklime particles, consistent with the formation of a hydration rim composed primarily of calcium-rich products. This high-contrast region is typical in SEM backscattered imaging due to the higher atomic weight of calcium. Radial nanoscale cracks are also visible around the hydrated quicklime particles. These cracks are likely the result of localized expansion during the hydration of CaO to $Ca(OH)_2$; however, thermal effects may also contribute. The hydration of quicklime is highly exothermic, and the elevated internal temperatures measured during curing could induce localized thermal gradients. Subsequent cooling may generate contraction stresses, further promoting microcrack development around the particles. Although these cracks are on the nanoscale and unlikely to immediately compromise mechanical integrity, their long-term influence on durability and transport properties warrants further study.

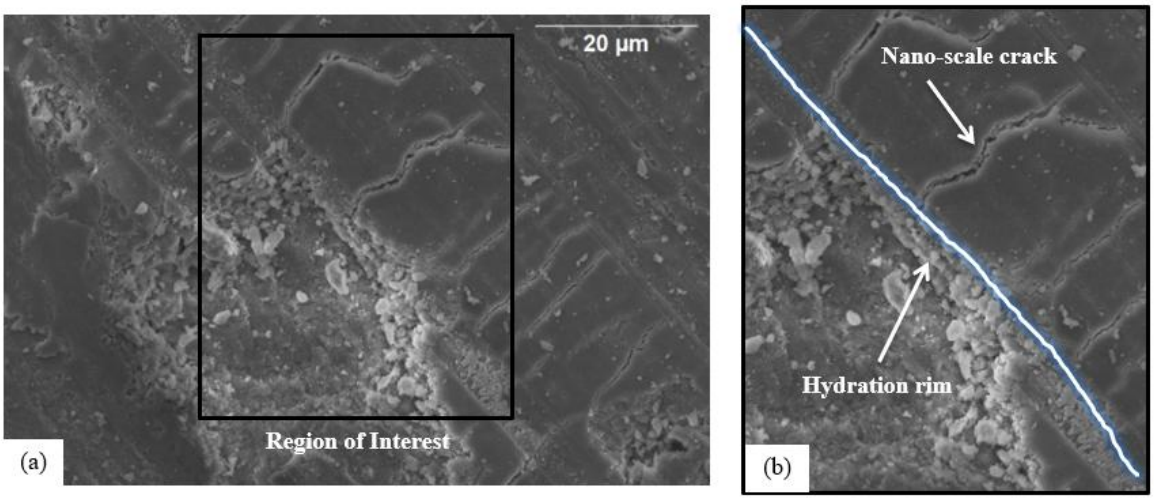

Figure 4.22. (a) Full SEM image, and (b) Zoomed region of interest showing the formation of a hydration rim around quicklime aggregates, with nano-scale cracks caused by quicklime expansion.

Seymour et al. [10] reported negligible drying shrinkage after 365 days in similar systems, suggesting that the expansive behavior of hydrated quicklime may stabilize over time; nonetheless, additional research is needed to fully characterize these thermal-chemical mechanisms and their implications for long-term performance.

4.4.4. Strength Recovery in Healed Specimens

To evaluate the mechanical recovery of self-healed specimens, compressive strength tests were performed on pre-cracked cylindrical specimens containing 2% and 4% quicklime aggregates after 180 days of exposure. The residual compressive strength values of the healed specimens are presented in Figure 4.23. Under cyclic water/air-drying conditions, microcracked specimens with crack widths ranging from 100 to 200 μm achieved compressive strength values of 6.4 MPa and 7.5 MPa for mixtures containing 2% and 4% quicklime, respectively. These values correspond to 15% and 14% strength recovery, relative to the uncracked specimens cured for 28 days. As the initial crack width increased to 200–300 μm, the strength values decreased to 5 MPa (11.8% recovery) and 6 MPa (11.3% recovery) for 2% and 4% quicklime specimens, respectively, under the same exposure conditions.

A similar trend was observed in specimens exposed to cyclic deicing salt solution/air-drying conditions. Specimens with 2% and 4% quicklime and crack widths of 100–200 μm exhibited compressive strengths of 5.3 MPa (12.4% recovery) and 6.3 MPa (11.8% recovery), respectively. For specimens with larger crack widths (200–300 μm), the compressive strength values were reduced to 4.6 MPa (10.7% recovery) and 5.3 MPa (9.86% recovery). These results indicate that the maximum recovery was achieved in the W-MICRO1-Q 2% specimens (15%), while the lowest recovery occurred in the DS-MICRO2-Q 4% specimens (9.86%). This suggests that smaller initial crack widths promote more effective healing, while exposure to cyclic deicing salt solutions hinders strength recovery. Additionally, although the 4% quicklime specimens generally exhibited higher compressive strength values after healing, their recovery percentages relative to uncracked specimens were lower than those of the 2% quicklime specimens. This can be attributed to the higher initial strength of the uncracked specimens containing 4% quicklime, which raises the baseline for recovery. Although the healed strength is greater, the relative recovery appears lower due to the larger difference from this initial strength.

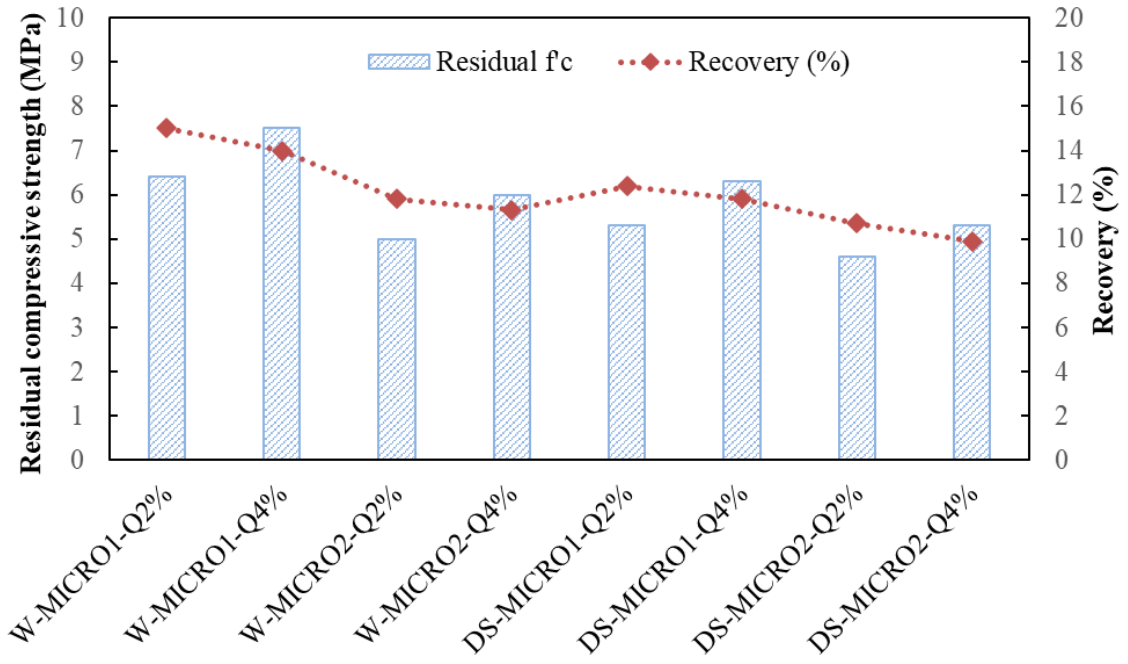

Figure 4.23. Healed compressive strength and recovery percentage of specimens with 2% and 4% quicklime after 180 days of exposure.

4.5. Study Limitations

Although this study offers valuable findings on the self-healing potential of concrete containing quicklime aggregates, it is important to recognize several limitations that may influence the interpretation and generalization of the results. Acknowledging these limitations helps guide future research and supports a more accurate understanding of the scope and applicability of the findings.

This study has several limitations that should be addressed in future research. First, it explored only two quicklime dosages (2% and 4%), leaving the optimal content for maximizing healing undetermined. The range of crack widths was also limited, focusing on two microcrack ranges (100–200 µm and 200–300 µm) and one macrocrack range (300–550 µm), without assessing larger structural cracks or complex crack patterns encountered in real structures. Additionally, specimens were subjected to controlled cyclic water/air-dry and deicing salt/air-dry exposures, which do not fully represent the fluctuating and unpredictable field conditions involving varying temperatures, moisture levels, and mechanical stresses. Mechanical performance was evaluated only through compressive strength recovery, omitting other critical indicators like tensile and flexural strength or

fracture energy. While SEM-EDS and UPV analyses provided valuable insights, a more complete microstructural characterization using techniques like X-ray diffraction (XRD) or thermogravimetric analysis (TGA) was not performed. The study also did not assess the durability of healed cracks under long-term aggressive exposure, such as extended freeze-thaw cycling or sustained chloride ingress. Finally, the potential influence of the superplasticizer used for workability improvement on the healing behavior was not isolated or independently evaluated.

CHAPTER 5 - CONCLUSIONS

This chapter summarizes the key findings of the research, highlights their practical implications for real-world applications, and offers recommendations for future studies aimed at advancing the understanding and implementation of quicklime-enhanced self-healing concrete.

5.1. Summary of Research

This study explores the self-healing capabilities of concrete incorporating quicklime (CaO) aggregates, aiming to improve the durability of concrete bridge decks that are prone to cracking from shrinkage, temperature changes, and traffic-induced stresses. Inspired by the longevity of ancient Roman concrete, three mixtures with 0%, 2%, and 4% quicklime were evaluated for their fresh properties, mechanical strength, durability, and crack-healing performance.

The addition of quicklime significantly affected fresh concrete behavior, reducing workability and setting time due to its high reactivity. While requiring superplasticizers for adjusting the workability, mixtures with quicklime showed elevated internal temperatures and accelerated setting (21 minutes for the 4% mix). In terms of mechanical performance, incorporating quicklime improved both compressive and tensile strengths: the C-Q 4% mixture achieved up to a 63% increase in 28-day compressive strength and a 54.3% increase in splitting tensile strength compared to the control. Durability performance was also enhanced in several aspects. Chloride ion penetration was reduced, with up to a 23% increase in electrical resistivity for the C-Q 2% mixture at 90 days. Abrasion resistance improved, and freeze–thaw resistance increased, with mass loss reduced from 8.8% in the control to 4% for the C-Q 4% mixture. However, drying shrinkage increased with quicklime content. At 56 days, the control mixture exhibited 0.031% shrinkage, while C-Q 2% and C-Q 4% showed 0.130% and 0.200%, respectively, approximately four to six times higher shrinkage than the control. These elevated shrinkage levels may raise concerns for restrained applications, such as bridge decks, where cracking risk must be considered in design.

Crack-healing evaluation was performed under two environmental conditions: cyclic water/air-drying and 20% deicing salt solution/air-drying for specimens with

controlled microcracks (100–250 μm, 200–350 μm) and macrocracks (300–550 μm). Healing was assessed via optical microscopy images, ultrasonic pulse velocity (UPV), water flow reduction, and SEM-EDS imaging. Results indicated that higher quicklime content led to higher healing performance up to 100% surface-crack closure in microcracks with width ranging 100–250 μm and 69% in macrocracks, along with enhanced depth-wise healing (13.8% UPV increase for W-MICRO1-Q 4%). SEM-EDS confirmed $CaCO_3$ as the main healing product in quicklime mixtures, contrasting with predominantly C-S-H in control samples.

Smaller crack widths consistently led to faster and more complete healing. Exposure of quicklime-based specimens to deicing salt cycles promoted better surface closure due to the catalytic role of NaCl in $CaCO_3$ precipitation, while internal healing was more effective under water/air-dry cycles for microcracks. After 180 days, mechanical recovery was highest in specimens with 2% quicklime and microcracks ranging 100–250 μm (15% strength regain), although absolute strength values were greater for the 4% mix.

Overall, this research demonstrates that quicklime incorporation significantly enhances the self-healing capacity, mechanical, and durability properties of concrete mixtures, offering a promising, sustainable approach for extending the service life of transportation infrastructure.

5.2. Major Findings

Based on the results obtained in this study, the following conclusions can be drawn:

- The addition of quicklime to the concrete mixtures negatively affected fresh properties by necessitating superplasticizer to restore acceptable workability, increased heat generation, and shortened the initial setting time. C-Q 0% had a 100 mm slump, while 2% and 4% mixes required superplasticizer and reached 200 mm. The exothermic reaction of quicklime with water raised temperatures from 23°C (73°F) to 33°C (91.4°F) for C-Q 2% and 46°C (114.8°F) for C-Q 4%, cutting setting times from 74 minutes to 40 and 21 minutes, respectively.
- Compressive strength increased with the addition of quicklime compared to the control mixture, showing a 63% improvement at 28 days and 59% at 90 days for the mixture with 4% quicklime. This enhancement is attributed to quicklime

forming extra C-S-H gel through reactions with silica and alumina, while its filler effect densifies the interfacial transition zone between the concrete matrix and aggregates.

- Splitting tensile strength increased with quicklime addition, rising by 35.3% and 54.3% at 28 days for 2% and 4% quicklime, respectively, and by 36.3% and 52.3% at 90 days. This improvement is attributed to the formation of additional C–S–H gel and a denser interfacial transition zone facilitated by the presence of quicklime.
- Drying shrinkage increased significantly with quicklime content. At 56 days, the C-Q 2% and C-Q 4% mixtures reached 0.130% and 0.200% shrinkage, respectively, being 3.7 times and 5.7 times greater than UDOT's allowable limit of 0.035% for bridge decks and structural concrete. This level of shrinkage presents a high risk of early-age cracking in restrained applications and would require mitigation strategies if used in practice.
- Surface electrical resistivity increased with the addition of quicklime, indicating enhanced resistance to chloride ion penetration. C-Q 2% showed the highest resistivity, with up to a 23% increase at 90 days compared to the control. This improvement is attributed to the formation of additional C–S–H gel and the pore-filling effect of quicklime, which reduce porosity and densify the microstructure.
- Abrasion resistance improved with the addition of quicklime, as shown by reduced mass loss at both 28 and 90 days. C-Q 4% specimens exhibited the lowest mass losses of 14.6% at 28 days and 12.0% at 90 days, indicating enhanced durability due to strength gain and reduced porosity over time.
- Specimens with 2% and 4% quicklime exhibited reduced mass loss after 300 freeze thaw cycles, 5.6% and 4% respectively, compared to 8.8% for the control mix. This enhanced resistance is attributed to the formation of additional C-S-H gel, which densifies the matrix and improves its ability to withstand internal pressure from freezing water.
- Increasing quicklime content significantly improves both surface-level and depth-wise healing. Specimens with 2% and 4% quicklime showed surface

crack closure improvements of up to 90–100% for microcracks (100–250 μm) and 20–69% for macrocracks, compared to corresponding 34–87% and 7–33% closure, respectively, in specimens without quicklime. The highest UPV increase (13.8%) was observed in W-MICRO1-Q 4%, while specimens without quicklime showed a maximum UPV increase of 7% (W-MICRO1-Q 0%), indicating better depth-wise healing in quicklime-containing concretes. Moreover, SEM-EDS analysis confirmed that specimens with quicklime contained more calcium carbonate ($CaCO_3$) crystals, which effectively filled cracks and enhanced healing, whereas specimens without quicklime mainly formed calcium silicate hydrate (C-S-H).

- Initial crack width plays a critical role in healing effectiveness, with smaller microcracks (100–250 μm) consistently showing higher crack closure percentages and faster healing progression than larger microcracks (200–350 μm) and macrocracks (300–550 μm). Microcracked specimens often achieved a higher level of healing, while macrocracked specimens healed more slowly and less completely, regardless of quicklime content.
- Healing performance was strongly influenced by exposure conditions. Cyclic deicing salt solution and air-drying led to up to 100% surface closure in microcracks and 69% in macrocracks, outperforming cyclic water/air-dry exposure in surface healing. However, depth-wise healing was slightly greater in microcracked specimens under cyclic water/air-dry conditions, while macrocracked specimens showed improved internal healing when exposed to deicing salt cycles. In specimens without quicklime, a 1:1 Na-to-Cl ratio confirmed the presence of pure NaCl crystals within cracks. In contrast, 2% and 4% quicklime mixtures exhibited no separate NaCl crystals, as NaCl acted as a catalyst for $CaCO_3$ formation, enhancing crack filling.
- Compressive strength tests after 180 days revealed that specimens with smaller initial crack widths (100–250 μm) exhibited greater mechanical recovery, with up to 15% strength regained in W-MICRO1-Q 2%. In contrast, wider cracks (200–350 μm) led to lower recovery rates. Specimens exposed to cyclic deicing salt solution showed reduced strength recovery compared to those under cyclic

water/air-dry conditions. While 4% quicklime mixtures achieved higher healed strength values, their recovery percentages were slightly lower than those of 2% quicklime mixtures due to higher original (uncracked) strength baselines

CHAPTER 6 - RECOMMENDATIONS AND IMPLEMENTATION

6.1. Recommendations

The quicklime-based self-healing concrete developed in this study shows promise in healing cracks in concrete. However, several practical considerations must be addressed before field implementation.

- First, the incorporation of quicklime significantly reduces workability and accelerates the setting time. In hot climates or during summer construction, this rapid setting may hinder proper placement, especially in large casting. As a result, additional labor may be required to ensure timely casting and finishing, increasing project complexity and cost. The use of superplasticizers is essential to restore workability, but they must be carefully dosed to maintain early-age reactivity.
- Second, the exothermic hydration of quicklime generates substantial heat, raising internal concrete temperatures up to a maximum of 46°C (114.8°F). This poses safety concerns for workers handling fresh concrete and necessitates the use of protective equipment and revised safety protocols. These requirements may further increase labor and equipment costs on-site.
- Third, while the majority of crack healing occurred within the first 60 days, full healing and mechanical recovery continued up to 180 days. This extended healing period may limit the material's suitability in applications requiring rapid crack closure or early-age strength regain, such as emergency repairs or high-traffic zones where early serviceability is critical.
- Fourth, quicklime incorporation led to a substantial increase in drying shrinkage, which is critical for restrained systems like bridge decks. At 56 days, the 2% and 4% mixes exceeded UDOT's allowable shrinkage limit of 0.035% by factors of 3.7 and 5.7, respectively. Such high shrinkage may lead to early-age cracking, wider crack openings, and increased moisture ingress, potentially accelerating corrosion and reducing durability in service. Without shrinkage mitigation strategies, such as internal curing, shrinkage-reducing admixtures, or fiber reinforcement, the high shrinkage response could limit field application despite the material's self-healing capability.

6.2. Implementation Plan

A future implementation plan for quicklime-based self-healing concrete should begin with laboratory optimization to determine the ideal dosage, enhance workability, and mitigate risks associated with its exothermic behavior during mixing. This should be followed by pilot-scale field trials to assess in-service performance under real environmental and loading conditions. Monitoring systems can help evaluate crack healing and durability over time. The results would inform the development of design guidelines, safety protocols, and material specifications. Broader implementation would require lifecycle cost analysis, supply chain readiness, and training for DOTs, contractors, and material producers.

REFERENCES

[1] B. Wan, C. Foley and J. Komp, "Concrete cracking in new bridge decks and overlays.," 2010.

[2] A. Elsafty and A. Abdel-Mohti, "Investigation of likelihood of cracking in reinforced concrete bridge decks.," *International Journal of Concrete Structures and Materials,* vol. 7, pp. 79-93, 2013.

[3] R. Hadidi and M. A. Saadeghvaziri, "Transverse cracking of concrete bridge decks: State-of-the-art.," *Journal of Bridge Engineering,* vol. 10, no. 5, pp. 503-510, 2005.

[4] P. D. Krauss and E. A. Rogalla, "Transverse cracking in newly constructed bridge decks (No. Project 12-37 FY'92).," 1996.

[5] M. A. Saadeghvaziri and R. Hadidi, "Transverse cracking of concrete bridge decks: Effects of design factors.," *Journal of Bridge Engineering,* vol. 10, no. 5, pp. 511-519, 2005.

[6] X. Ni, M. Leon-Miquel, Q. R. Greiner, A. Paul and Q. Jin, "Crack sealers for the preservation of concrete bridge decks: a synthesis of a national survey and literature review.," *Journal of Infrastructure Preservation and Resilience,* vol. 4, no. 1, p. 23, 2023.

[7] U. Kannan, S. A. Gafoor, S. Srivastava, M. Nithyadharan, S. S. Gupta and S. M. Maliyekkal, "A waste-derived nanocomposite sealant for repairing micro-cracks in concrete.," *Journal of Building Engineering,* vol. 48, p. 103965, 2022.

[8] A. Vanelstraete and A. Bondt, Crack prevention and use of overlay systems, CRC Press, 2004, pp. 53-67.

[9] G. Nossoni and R. S. Harichandran, "Improved repair of concrete structures using polymer concrete patch and FRP overlay.," *Journal of Materials in Civil Engineering,* vol. 22, no. 4, pp. 314-322, 2010.

[10] L. M. Seymour, J. Maragh, P. Sabatini, M. D. Tommaso, J. C. Weaver and A. Masic, "Hot mixing: Mechanistic insights into the durability of ancient Roman concrete.," *Science Advances,* vol. 9, no. 1, p. eadd1602, 2023.

[11] A. Talaiekhozani and M. Z. Abd Majid, "A review of self-healing concrete research development.," *Journal of Environmental Treatment Techniques ,* vol. 2, no. 1, pp. 1-11, 2014.

[12] V. C. Li and E.-H. Yang, "Self healing in concrete materials. In Self healing materials: an alternative approach to 20 centuries of materials science," *Dordrecht: Springer Netherlands.,* pp. 161-193, 2007.

[13] N. De Belie, E. Gruyaert, A. Al-Tabbaa, p. Antonaci, C. Baera, D. Bajare, A. Darquennes, R. Davies, L. Ferrara, T. Jefferson, C. Litina, B. Miljevic, A. Otlewska, J. Ranogajec, M. Roig-Flores, K. Paine, P. Lukowski, P. Serna, J.-M. Tulliani, S. Vucetic, J. Wang and H. M. Jonkers, " A review of self-healing concrete for damage management of structures.," *Advanced materials interfaces,* vol. 5, no. 17, p. 1800074, 2018.

[14] K.-M. Lee, H.-S. Kim, D.-K. Lee and K.-J. Shin, "Self-healing performance evaluation of concrete incorporating inorganic materials based on a water permeability test.," *Materials,* vol. 14, no. 12, p. 3202, 2021.

[15] K. V. Tittelboom, E. Gruyaert, H. Rahier and N. De Belie, "Influence of mix composition on the extent of autogenous crack healing by continued hydration or calcium carbonate formation.," *Construction and Building materials,* vol. 37, pp. 349-359, 2012.

[16] L. Ferrara, V. Krelani and M. Carsana, "A “fracture testing” based approach to assess crack healing of concrete with and without crystalline admixtures.," *Construction and Building Materials,* vol. 68, pp. 535-551, 2014.

[17] Z. Jiang, W. Li and Z. Yuan, " Influence of mineral additives and environmental conditions on the self-healing capabilities of cementitious materials," *Cement and Concrete Composites,* vol. 57, pp. 116-127, 2015.

[18] A. R. Suleiman, A. J. Nelson and M. L. Nehdi, "Visualization and quantification of crack self-healing in cement-based materials incorporating different minerals," *Cement and Concrete Composites,* vol. 103, pp. 49-58, 2019.

[19] F. Huang and S. Zhou, "A review of lightweight self-healing concrete.," *Materials,* vol. 15, no. 21, p. 7572, 2022.

[20] Y. Yang, M. D. Lepech, E.-H. Yang and V. C. Li, "Autogenous healing of engineered cementitious composites under wet–dry cycles.," *Cement and Concrete Research ,* vol. 39, no. 5, pp. 382-390, 2009.

[21] Y. Yang, E.-H. Yang and V. C. Li, " Autogenous healing of engineered cementitious composites at early age.," *Cement and concrete research,* vol. 41, no. 2, pp. 176-183, 2011.

[22] Y. Zhu, Z. Zhang, X. Chen, D. Zou, X. Guan and B. Dong, "Non-destructive methods to evaluate the self-healing behavior of engineered cementitious composites (ECC).," *Construction and Building Materials,* vol. 230, p. 116753, 2020.

[23] A. Neves, J. A. P. P. Almeida, T. Miranda, V. M. C. F. Cunha and E. Pereira, "Self-healing assessment and variability in plain and recycled tyre fiber reinforced concrete based on tensile splitting test," *Journal of Building Engineering,* vol. 84, p. 108567, 2024.

[24] T. Nishiwaki, M. Koda, M. Yamada, H. Mihashi and T. Kikuta, "Experimental study on self-healing capability of FRCC using different types of synthetic fibers," *Journal of Advanced Concrete Technology,* vol. 10, no. 6, pp. 195-206, 2012.

[25] S. R. White, N. R. Sottos, P. H. Geubelle, J. S. Moore, M. R. Kessler, S. R. Sriram, E. N. Brown and S. Viswanathan, "Autonomic healing of polymer composites," *Nature,* vol. 409, no. 6822, pp. 794-797, 2001.

[26] D. Homma, H. Mihashi and T. Nishiwaki, "Self-healing capability of fibre reinforced cementitious composites.," *Journal of advanced concrete technology,* vol. 7, no. 2, pp. 217-228, 2009.

[27] H. X. D. Lee, H. S. Wong and N. R. Buenfeld, "Self-sealing of cracks in concrete using superabsorbent polymers.," *Cement and concrete Research,* vol. 79, pp. 194-208, 2016.

[28] H. Hermawan, P. Minne, P. Serna and E. Gruyaert, "Understanding the impacts of healing agents on the properties of fresh and hardened self-healing concrete: a review.," *Processes,* vol. 9, no. 12, p. 2206, 2021.

[29] B. Hilloulin, K. V. Tittelboom, E. Gruyaert, N. Dele Belie and A. Loukili, "Design of polymeric capsules for self-healing concrete," *Cement and Concrete Composites,* vol. 55, pp. 298-307, 2015.

[30] D. Snoeck, K. V. Tittelboom, S. Steuperaert, P. Dubruel and N. De Belie, " Self-healing cementitious materials by the combination of microfibres and superabsorbent polymers.," *Journal of Intelligent Material Systems and Structures,* vol. 25, no. 1, pp. 13-24, 2014.

[31] H. M. Jonkers, "Self healing concrete: a biological approach. In Self healing materials: An alternative approach to 20 centuries of materials science," *Dordrecht: Springer Netherlands,* pp. 195-204, 2007.

[32] K. Vijay, M. Murmu and S. V. Deo, "Bacteria based self healing concrete–A review.," *Construction and building materials,* vol. 152, pp. 1008-1014, 2017.

[33] V. G. Cappellesso, T. V. Mullem, E. Gruyaert, K. V. Tittelboom and N. De Belie, "Bacteria-based self-healing concrete exposed to frost salt scaling.," *Cement and Concrete Composites,* vol. 139, p. 105016, 2023.

[34] H. M. Jonkers and E. Schlangen, "Development of a bacteria-based self healing concrete," *Tailor made concrete structures,* vol. 1, pp. 425-430, 2008.

[35] M. Sarkar, M. Maiti, M. A. Malik and S. Xu, "Evaluation of the crack-healing performance and durability of bacteria integrated alkali-activated fly ash composites," *Journal of Building Engineering ,* vol. 54, p. 104642, 2022.

[36] V. Wiktor and H. M. Jonkers, "Quantification of crack-healing in novel bacteria-based self-healing concrete.," *Cement and concrete composites,* vol. 33, no. 7, pp. 763-770, 2011.

[37] J. Y. Wang, N. De Belie and W. Verstraete, "Diatomaceous earth as a protective vehicle for bacteria applied for self-healing concrete," *Journal of industrial microbiology and biotechnology,* vol. 39, no. 4, pp. 567-577, 2012.

[38] J. Xu and W. Yao, "Multiscale mechanical quantification of self-healing concrete incorporating non-ureolytic bacteria-based healing agent," *Cement and concrete research,* vol. 64, pp. 1-10, 2014.

[39] M. Li and V. C. Li, "Cracking and healing of engineered cementitious composites under chloride environment," *ACI Materials Journal,* vol. 108, no. 3, p. 333, 2011.

[40] M. Roig-Flores, S. Moscato, P. Serna and L. Ferrara, "Self-healing capability of concrete with crystalline admixtures in different environments.," *Construction and Building Materials,* vol. 86, pp. 1-11, 2015.

[41] M. Roig-Flores, F. Pirritano and L. Ferrara, "Effect of crystalline admixtures on the self-healing capability of early-age concrete studied by means of permeability and crack closing tests.," *Construction and Building Materials,* vol. 114, pp. 447-457, 2016.

[42] K. Sisomphon, O. Copuroglu and E. A. B. Koenders, "Effect of exposure conditions on self healing behavior of strain hardening cementitious composites incorporating various cementitious materials.," *Construction and Building Materials,* vol. 42, pp. 217-224, 2013.

[43] D. Palin, V. Wiktor and H. M. Jonkers, "Autogenous healing of marine exposed concrete: Characterization and quantification through visual crack closure.," *Cement and Concrete Research,* vol. 73, pp. 17-24, 2015.

[44] M. D. Jackson, J. M. Logan, B. E. Scheetz, D. M. Deocampo, C. G. Cawood, F. Marra, M. Vitti and L. Ungaro, "Assessment of material characteristics of ancient concretes, Grande Aula, Markets of Trajan, Rome," *Journal of Archaeological Science,* vol. 36, no. 11, pp. 2481-2492, 2009.

[45] M. D. Jackson, E. N. Landis, P. F. Brune, M. Vitti, H. Chen, Q. Li, M. Kunz, H.-R. Wenk, P. J. M. Monteiro and A. R. Ingraffea, "Mechanical resilience and cementitious processes in Imperial Roman architectural mortar," *Proceedings of the National Academy of Sciences ,* vol. 111, no. 52, pp. 18484-18489, 2014.

[46] ACI Committee 224, "Control of Cracking in Concrete Structures (ACI PRC-224-01)," American Concrete Institute, Farmington Hills, MI, 2008.

[47] G. H. Koch, M. P. H. Brongers, N. G. Thompson, Y. P. Virmani and J. H. Payer, "Corrosion Cost and Preventive Strategies in the United States (No. FHWA-RD-01-156,, R315-01).," Federal Highway Administration, United States, 2002.

[48] R. Gagné and M. Argouges, "A study of the natural self-healing of mortars using air-flow measurements.," *Materials and structures,* vol. 45, pp. 1625-1638, 2012.

[49] D.-Y. Yoo, W. Shin, B. Chun and N. Banthia, "Assessment of steel fiber corrosion in self-healed ultra-high-performance fiber-reinforced concrete and its effect on tensile performance.," *Cement and Concrete Research,* vol. 133, p. 106091, 2020.

[50] ASTM International, "Standard Specification for Concrete Aggregates (ASTM C33)," American Society for Testing and Materials, West Conshohocken, PA, 2013.

[51] ASTM International, "Standard Test Method for Slump of Hydraulic-Cement Concrete (ASTM C143)," American Society for Testing and Materials., West Conshohocken, PA, 2003.

[52] ASTM International, "tandard Test Method for Time of Setting of Hydraulic Cement by Vicat Needle (ASTM C191)," American Society for Testing and Materials., West Conshohocken, PA, 2013.

[53] ASTM International, "Standard Test Method for Compressive Strength of Cylindrical Concrete Specimens (ASTM C39)," American Society for Testing and Materials., West Conshohocken, PA, 2014.

[54] ASTM International, "Standard Test Method for Splitting Tensile Strength of Cylindrical Concrete Specimens (ASTM C496)," American Society for Testing and Materials., West Conshohocken, PA, 2011.

[55] ASTM International, "Standard Test Method for Length Change of Hardened Hydraulic-Cement Mortar and Concrete (ASTM C157)," American Society for Testing and Materials., West Conshohocken, PA, 2008.

[56] AASHTO, "Standard Method of Test for Surface Resistivity Indication of Concrete's Ability to Resist Chloride Ion Penetration.," American Association of State Highway and Transportation Officials., Washington. D.C, 2015.

[57] ASTM International, "Standard Test Method for Determining Potential Resistance to Degradation of Pervious Concrete by Impact and Abrasion (ASTM C1747)," American Society for Testing and Materials., West Conshohocken, PA, 2013.

[58] ASTM International, "tandard Test Method for Resistance of Concrete to Rapid Freezing and Thawing (ASTM C666)," American Society for Testing and Materials., West Conshohocken, PA, 2008.

[59] ASTM International, "Standard Test Method for Fundamental Transverse, Longitudinal, and Torsional Resonant Frequencies of Concrete Specimens (ASTM C215)," American Society for Testing and Materials., West Conshohocken, PA, 2020.

[60] ASTM International, "Standard test method for pulse velocity through concrete (ASTM C597)," American Society for Testing and Materials, West Conshohocken, PA, 2002.

[61] ACI Committee, "Report on Pervious Concrete (ACI 522R)," American Concrete Institute , Farmington Hills, MI, 2010.

[62] N. Neithalah, M. S. Sumanasooriya and O. Deo, "Characterizing pore volume, sizes, and connectivity in pervious concretes for permeability prediction.," *Materials characterization,* vol. 61, no. 8, pp. 802-813, 2010.

[63] P. K. Acharya, S. K. Patro and N. C. Moharana, "Effect of lime on mechanical and durability properties of blended cement based concrete.," *Journal of The Institution of Engineers (India): Series A,* vol. 97, pp. 71-79, 2016.

[64] B. J. Nam, S. K. Noh, E. K. Kim, S. A. Ahn and S. Y. Kang, "Initial behavior and shrinkage properties of lime mortars for restoration of cultural heritage according to the mixing ratio," *Journal of Conservation Science,* vol. 36, no. 6, pp. 456-474, 2020.

[65] J. M. Commandré, S. Salvador and A. Nzihou, "Reactivity of laboratory and industrial limes.," *Chemical Engineering Research and Design,* vol. 85, no. 4, pp. 473-480, 2007.

[66] M. Abdul Latif, S. Naganathan, H. Abdul Razak and K. Nasharuddin Mustapha, "Performance of lime kiln dust as cementitious material.," *Procedia Engineering,* vol. 125, pp. 780-787, 2015.

[67] A. A. Adam, N. H. Amiri, I. W. Suarnita and N. Rupang, "The effect of lime addition on the setting time and strength of ambient cured fly ash based geopolymer binder.," *In MATEC web of conferences,* vol. 47, p. 01015, 2016.

[68] K. Kaewmanee, P. Krammart, T. Sumranwanich, P. Choktaweekarn and S. Tangtermsirikul, "Effect of free lime content on properties of cement–fly ash mixtures.," *Construction and Building Materials,* vol. 38, pp. 829-836, 2013.

[69] S. A. Barbhuiya, J. K. Gbagbo, M. I. Russell and P. Basheer, "Properties of fly ash concrete modified with hydrated lime and silica fume.," *Construction and Building Materials,* vol. 23, no. 10, pp. 3233-3239, 2009.

[70] M. Nazari, S. Banerji and R. J. Thomas, "Developing and Characterizing Self-Crack-Healing Roman Concrete for Bridge Decks Applications.," in *10th International Conference on CONcrete under SEvere Conditions – Environment and Loading*, Chennai, India, 2024.

[71] V. Sata, C. Jaturapitakkul and K. Kiattikomol, "Influence of pozzolan from various by-product materials on mechanical properties of high-strength concrete.," *Construction and building materials,* vol. 21, no. 7, pp. 1589-1598, 2007.

[72] J. S. Pozo-Antonio, "Evolution of mechanical properties and drying shrinkage in lime-based and lime cement-based mortars with pure limestone aggregate.," *Construction and Building Materials,* vol. 77, pp. 472-478, 2015.

[73] Y. Dong, C. Su, P. Qiao and L. Sun, "A thermal-hydraulic-mechanical coupling model for freezing process simulation of cementitious materials with entrained air voids.," *Construction and Building Materials,* vol. 243, p. 118253, 2020.

[74] K. Ebrahimi, M. J. Daiezadeh, M. Zakertabrizi, F. Zahmatkesh and A. Habibinejad Korayem, "A review of the impact of micro-and nanoparticles on freeze-thaw durability of hardened concrete: Mechanism perspective.," *Construction and Building Materials ,* vol. 186, pp. 1105-1113, 2018.

[75] Z. Zhou and P. Qiao, "Durability of ultra-high performance concrete in tension under cold weather conditions.," *Cement and Concrete Composites,* vol. 94, pp. 94-106, 2018.

[76] M. Sarkar, T. Chowdhury, B. Chattopadhyay, R. Gachhui and S. Mandal, "Autonomous bioremediation of a microbial protein (bioremediase) in Pozzolana cementitious composite.," *Journal of materials science,* vol. 49, pp. 4461-4468, 2014.

[77] J. Qiu, H. S. Tan and E.-H. Yang, "Coupled effects of crack width, slag content, and conditioning alkalinity on autogenous healing of engineered cementitious composites.," *Cement and Concrete Composites,* vol. 73, pp. 203-212, 2016.

[78] H. H. Nguyễn, J.-I. Choi, S.-E. Park, S. L. Cha, J. Huh and B. Y. Lee, "Autogenous healing of high strength engineered cementitious composites (ECC) using calcium-containing binders.," *Construction and Building Materials,* vol. 265, p. 120857, 2020.

[79] M. Rajczakowska , K. Habermehl-Cwirzen, H. Hedlund and A. Cwirzen, "The effect of exposure on the autogenous self-healing of ordinary Portland cement mortars.," *Materials,* vol. 12, no. 23, p. 3926, 2019.

[80] H. Huang, G. Ye and D. Damidot, "Characterization and quantification of self-healing behaviors of microcracks due to further hydration in cement paste.," *Cement and Concrete Research,* vol. 52, pp. 71-81, 2013.

[81] H. Huang, G. Ye and D. Damidot, "Effect of blast furnace slag on self-healing of microcracks in cementitious materials.," *Cement and concrete research,* vol. 60, pp. 68-82, 2014.

[82] Y. Takita, M. Eto, H. Sugihara and K. Nagaoka, "Promotion mechanism of co-existing NaCl in the synthesis of CaCO3.," *Materials Letters,* vol. 61, no. 14-15, pp. 3083-3085, 2007.

[83] M. Sadiuddin, A. B. M. Amrul Kaish, C.-O. Woon and S. N. Raman, "Early-age cracking in concrete: Causes, consequences, remedial measures, and recommendations.," *Applied Sciences,* vol. 8, no. 10, p. 1730, 2018.

[84] R. Morello-Frosch, M. J. Pastor, C. Porras and J. Sadd, "Environmental justice and regional inequality in southern California: implications for future research.," *Environmental health perspectives,* vol. 110, no. 2, pp. 149-154, 2002.

[85] A. Batog and . E. Stilger-Szydło, "Low-strength substrates and anthropogenic soils in transportation engineering.," *Studia Geotechnica et Mechanica,* vol. 40, no. 4, pp. 292-299, 2018.